Vacuum Breathing Theory (VBT)

A Foundational Postulate on the Nature of the Vacuum

David L. Poole

Independent Researcher

Abstract

Microscale — Quantum and Atomic Foundations. The Vacuum Breathing Theory (VBT) treats spacetime as a single, coherent oscillatory medium whose carrier phase is globally uniform at the Planck frequency, while the local breathing amplitude varies. Matter and charge arise as resonant wave loops within this substrate, and atomic quantization and orbital stability follow from fixed phase–variable amplitude resonance conditions, reproducing the hydrogen spectrum, magnetic moments, and relativistic mass variation without probabilistic postulates. When two systems interact, their wave envelopes couple to the same carrier phase, establishing a shared relative phase that persists under separation; entanglement correlations therefore reflect the temporal unity of the vacuum, not superluminal signaling.

Macroscale — Gravitation and Cosmology. Gradients in the mean vacuum amplitude produce curvature and time dilation consistent with general relativity in the weak limit. Cosmic redshift and expansion arise from the slow relaxation of the same field, and galactic rotation curves follow from distributed stellar-mass black holes sustained by vacuum elasticity, removing the need for non-baryonic dark matter.

Bridging Scales — Gauge Structure and Coherence. Between these limits, the vacuum supports three stiffness domains corresponding to SU(3), SU(2), and U(1). Their relative stiffnesses reproduce the observed coupling hierarchy, and the scalar amplitude of the SU(2) domain corresponds to the physical Higgs field, linking mass generation to vacuum stiffness. Together these results form a continuous framework in which quantum structure, gravitation, entanglement, and cosmology arise from the elastic dynamics of a globally phase-coherent spacetime.

October 30, 2025

Version 14

Contents

1	Introduction	4
2	Vacuum Breathing Postulate 2.1 Vacuum Breathing Scale Factor	5 5 7 8
3	Quantum Mechanics as an Envelope on the Planck Carrier 3.1 Madelung representation	8
4	Atomic model 4.1 Setup and motivation	11 11 12 13 14 14 15
5	Orbital Transitions in the Breathing Vacuum 5.1 Continuous re-locking dynamics 5.2 Spontaneous Emission in VBT 5.3 Spectral line reproduction 5.4 Selection rules from vacuum geometry 5.5 Natural linewidth and lineshape 5.6 Lamb shift as high-frequency modulation 5.7 Impact of breathing waveform symmetry 5.8 Forbidden transitions 5.9 Summary	166 177 177 188 188 199 200 211
6	Quantum Effects Beyond Atomic Transitions6.1 Dirac Points and Massless Excitons6.2 Tunneling as Deterministic Re-Locking6.3 Bridge to Broader Quantum Properties6.4 Quantum Hall Effect as Vacuum Phase-Locking6.5 The Vacuum as a Single Coherent Oscillator6.6 Macroscopic Delocalization and VBT Predictions	
7	Static Biases in the Vacuum Grid 7.1 Overview and Motivation 7.2 Charge as Static Bias	31 31 32 33 33 33

	7.8	Faraday and Kerr Effects	33
	7.9	Zeeman splitting and the magnetic quantum number	34
	7.10	Implications for Field Theory	34
			34
8	Elec	tromagnetism as Transverse Shear of the Breathing Vacuum	37
	8.1	Wave Equation and Light Speed	37
	8.2	Gauge Potentials and Fields	38
	8.3		39
	8.4		40
	8.5		40
	8.6	Experimental evidence of quantized shear: single-photon OAM (Orbital Angular Mo-	-0
	0.0		41
	8.7		42
	0.1	Electromagnetism as Duar to Gravitation	42
9	Gra	vity in the Breathing Vacuum	42
	9.1	•	- - 43
	9.2		43
	9.3		43
	9.4		44
			$\frac{44}{44}$
	9.5		
	9.6	Bipolar nature and transition to cosmology	44
10	Cos	mology of the Expanding Vacuum	45
10			45
			45
			46
			47
		•	47
		ı o	47
			48
			48
			49
		1 1 0	50
		1	51
		•	55
	10.13	Relation to General Relativity	55
	C I	1 136 11	
11		1 0 0 0	57 57
			57
		· · · · · · · · · · · · · · · · · · ·	57 2
			58 58
		00 1	58
		00	58
			59
			60
			60
	11.9	Early-universe confinement	62

	11.10Running couplings as stiffness ratios	62 62 63			
12	Conclusion and Outlook 12.1 Summary of results across scales	65 65 66 66			
\mathbf{G}	ossary	66			
Aj	Appendices				
A	Higher hydrogenic states example $(3d_{z^2})$ A.1 Analytic formA.2 Numerical validationA.3 Conclusion	68 68 69			
В	Averaged Dynamics and Derived Radial Distributions B.1 Setup and multiple-scales averaging	70 70 70 71 71			
C	Radiation and Stability in the Conformal Fabric C.1 Maxwell theory in a conformally flat metric C.2 Poynting flux and conformal scaling C.3 Stationary bound states as standing—wave sources C.4 Local criterion via proper acceleration C.5 Conclusion	71 71 72 72 73 73			
D	Lagrangian Formulation for Electromagnetism in the Breathing Vacuum D.1 Charge as a Topological Defect in the Vacuum Fabric				
	Vacuum birefringence E.1 VBT expectation	74 75 75 75 75			
\mathbf{F}	Simulation validation	75			

1 Introduction

Modern physics describes nature through several distinct formalisms—quantum mechanics, general relativity, and quantum field theory—each remarkably accurate within its domain yet founded on different assumptions about the nature of the vacuum. In the quantum picture, the vacuum is a statistical state defined only by probabilistic amplitudes; in relativity, it is a geometric manifold that curves but does not itself evolve; and in field theory, it is an energetic background that permeates space but lacks direct mechanical form. The *Vacuum Breathing Theory* (VBT) begins from a simpler physical principle: the vacuum is a real, elastic continuum that undergoes coherent oscillation at the Planck frequency. All observable fields, particles, and forces arise as local modulations of this breathing substrate.

The foundational postulate is the distinction between *phase* and *amplitude* of the breathing vacuum. The vacuum breathes with a globally coherent phase that acts as a universal temporal reference, while the amplitude of this breathing varies locally. Local amplitude gradients encode curvature, inertial mass, and energy density, whereas the global phase remains fixed across the continuum. Thus, the vacuum does not merely serve as the stage on which physics unfolds; it provides the underlying timing structure that allows coordinated dynamics to exist.

At microscopic scales, this structure reproduces the quantized stability of matter. Standing wave patterns within the breathing continuum correspond to the allowed bound states of atomic systems and yield the same discrete spectra predicted by quantum mechanics. Emission, absorption, tunneling, and coherence limits arise from amplitude—phase resonance conditions rather than probabilistic postulates. In this view, quantization and wave—particle duality emerge naturally from the periodic structure of the vacuum itself.

At macroscopic scales, slow spatial variations in the breathing amplitude generate gravitational curvature, while temporal evolution of the mean amplitude $A_{\text{mean}}(t)$ drives cosmic expansion. When compact objects locally anchor the vacuum—such as stellar remnants and black holes—the resulting envelope deformation yields galactic rotation curves consistent with observation, without invoking non-baryonic dark matter. Fits to the Milky Way and Andromeda indicate anchor densities that match known black hole and neutron-star populations, suggesting that the effects commonly attributed to dark matter may instead reflect the elastic structure of the vacuum.

At higher stiffness regimes, the same medium exhibits distinct deformation modes corresponding to the gauge sectors of the Standard Model. The SU(3), SU(2), and U(1) symmetries arise as discrete coherence states of the breathing field, each representing a characteristic stiffness or polarization. The scalar vacuum amplitude A_{mean} plays the role of the physical Higgs field: its equilibrium value sets the vacuum expectation, and local suppression generates inertial mass. In this manner, gravitation, mass generation, and cosmological evolution emerge as different expressions of the same breathing continuum.

A key consequence of the globally coherent phase is quantum entanglement. When two matterwave envelopes interact, they couple to the same phase of the vacuum breathing mode, establishing a shared relative phase that can persist under spatial separation. The resulting correlations require no superluminal signaling because they reflect the temporal unity of the vacuum, not information transfer between distant particles. Entanglement thus arises from the same fixed-phase, variableamplitude structure that governs both quantum stability and gravitational dynamics.

The sections that follow develop this framework quantitatively. Sections 2–8 formalize the breathing vacuum and derive its stationary wave solutions. Sections 9–10.11 apply the theory to gravitational and galactic phenomena. Section 11 interprets gauge symmetries as stiffness regimes of the vacuum, and Section 12 summarizes testable predictions. Throughout, no new particles or forces are introduced; only the behavior of the vacuum itself is reconsidered.

2 Vacuum Breathing Postulate

We postulate that the vacuum is an isotropic, elastic medium undergoing a global, symmetric breathing at the Planck frequency. Ideas treating spacetime (or vacuum) as an elastic, deformable medium have been explored in prior work [1, 2], offering conceptual parallels to—but distinct from—the Planck-frequency breathing dynamics proposed here.

The breathing modulates the local scale of space by

$$s(t) = s_0 \left[1 + \varepsilon \cos(\omega_P t) \right],\tag{1}$$

where s_0 is the mean spatial scale, $\omega_P = t_P^{-1}$ is the Planck angular frequency, and ε is the fractional amplitude. We choose ε such that the peak-to-peak scale change equals one Planck length per Planck length unit:

$$\frac{s_{\text{max}}}{s_{\text{min}}} = \frac{1+\varepsilon}{1-\varepsilon} = 2 \quad \Rightarrow \quad \varepsilon = \frac{1}{3}$$
 (2)

The physical metric is taken to be conformally related to the Minkowski metric:

$$g_{\mu\nu}(t, \mathbf{x}) = \Omega^2(t, \mathbf{x}) \, \eta_{\mu\nu}, \qquad \Omega(t, \mathbf{x}) = A(t) \, [1 + \alpha(\mathbf{x})].$$
 (3)

Here A(t) is the strictly global, perfectly synchronized Planck-frequency breathing (one universal clock), while $\alpha(\mathbf{x})$ encodes small, slowly varying *amplitude* suppressions near mass—energy. There are no spatially varying carrier phases in VBT.

No local phases. In VBT the Planck-carrier phase $\Phi_P(t) = \omega_P t$ is universal and synchronized across the entire universe. Any "phase" mentioned elsewhere refers to the *matter-wave envelope* phase of a system, not a spatially varying vacuum carrier phase.

In the absence of local modulation $(\theta, \alpha = 0)$, the breathing is a pure conformal scaling that preserves light cones and yields no observable effect at low energies.

Lorentz invariance and the absence of a preferred frame. Although the vacuum breathes at the Planck frequency, this oscillation represents a scalar modulation of amplitude rather than a propagating phase wave. The quantity A_{mean} transforms as a Lorentz scalar:

$$\langle A_{\rm mean}^2 \rangle = \langle A_{\rm mean}'^2 \rangle, \qquad x'^{\mu} = \Lambda^{\mu}{}_{\nu} x^{\nu},$$
 (4)

so the cycle-averaged energy density and all derived observables remain invariant under Lorentz transformations. Because no information or phase is transported by the Planck-frequency carrier, there exists no measurable anisotropy or preferred frame. The vacuum is thus globally coherent yet locally Lorentz-symmetric, yielding the same null results for Michelson–Morley–type tests as general relativity.¹

2.1 Vacuum Breathing Scale Factor

The instantaneous breathing factor of the vacuum is denoted A(t). This dimensionless quantity rescales physical lengths according to

$$L_{\text{phys}}(t) = A(t) L_{\text{comoving}}.$$
 (5)

¹Formally, $A_{\text{mean}}(x)$ behaves as a real scalar field analogous to the cosmological inflaton or Higgs field, whose kinetic term $g^{\mu\nu}\partial_{\mu}A_{\text{mean}}\partial_{\nu}A_{\text{mean}}$ and potential $V(A_{\text{mean}})$ preserve Lorentz invariance of the cycle-averaged stress–energy tensor.

Definition of the mean amplitude. We define the slow mean of this oscillation by a Planck cycle average:

$$A_{\text{mean}}(t) \equiv \langle A(t) \rangle,$$
 (6)

where the angle brackets denote averaging over many cycles of the fast Planck–frequency oscillation. This mean evolves cosmologically from 0.5 shortly after the Big Bang toward 1 as the vacuum smooths.

Multiplicative decomposition. It is convenient to separate the slow mean from the fast oscillatory component multiplicatively:

$$A(t) = A_{\text{mean}}(t) \exp(\xi(t)), \qquad \langle \xi(t) \rangle = 0. \tag{7}$$

Here $\xi(t)$ is a rapidly varying Planck–frequency phase with vanishing mean and decreasing variance over cosmic history. In the limit of vanishing breathing, $\xi \to 0$, the instantaneous scale factor reduces to the mean: $A(t) \to A_{\text{mean}}(t)$.

Planck-scale bound. The Planck length ℓ_P imposes a lower bound on physical lengths. Since $L_{\rm phys}(t) = A(t) L_{\rm comoving}$ with $A(t) = A_{\rm mean}(t) \exp(\xi(t))$, we require

$$A_{\text{mean}}(t) \exp(\xi(t)) L_{\text{comoving}} \ge \ell_P.$$
 (8)

This inequality constrains the allowed excursions of the oscillatory component $\xi(t)$, ensuring that the breathing never pushes physical lengths below the Planck floor.

Absolute vs. fractional oscillation. The peak-to-peak excursion of the breathing remains fixed at one Planck length, even as the cycle-averaged amplitude A_{mean} evolves cosmologically. What changes is the fractional modulation $\varepsilon \equiv \Delta A/A_{\text{mean}}$: as A_{mean} grows, the relative oscillation becomes smaller when measured against co-moving rulers that themselves scale with A_{mean} . This ensures that dimensionless ratios remain invariant in local physics.

Crucially, the $2\times$ modulation of the Coulomb field, which stabilizes atomic orbitals, arises from the instantaneous rescaling of the metric $(1/A^2(t))$ rather than from the absolute fractional size of ε . Thus the forcing mechanism is preserved across cosmic time, even though the fractional oscillation amplitude diminishes. This distinction between absolute Planck-length excursion and relative modulation resolves the apparent tension between vacuum breathing and long-term stability of matter.

Limits of the cycle–averaged formulation. The field equations in this work apply to the vacuum on scales much larger than the Planck length and for energy densities far below the Planck regime. All measurable quantities are computed from cycle–averaged amplitudes $\langle A_{\text{mean}} \rangle$ and stiffness values that represent the mean of many Planck–frequency oscillations. Near singular conditions—inside black-hole horizons, during the earliest phase of inflation, or wherever the local energy density approaches the Planck value— the averaging procedure may break down and the full microscopic breathing dynamics would dominate. In these extreme domains the effective metric $g_{\mu\nu} = A_{\text{mean}}^2 \eta_{\mu\nu}$ should be regarded as an approximation to a deeper non-averaged structure. For all laboratory, astrophysical, and cosmological conditions currently accessible, the averaged formulation remains valid and reproduces general-relativistic limits. As summarized in Figure 1, the breathing scale factor and its cycle-averaged mean illustrate the constraints discussed in Eqs. (6)–(8).

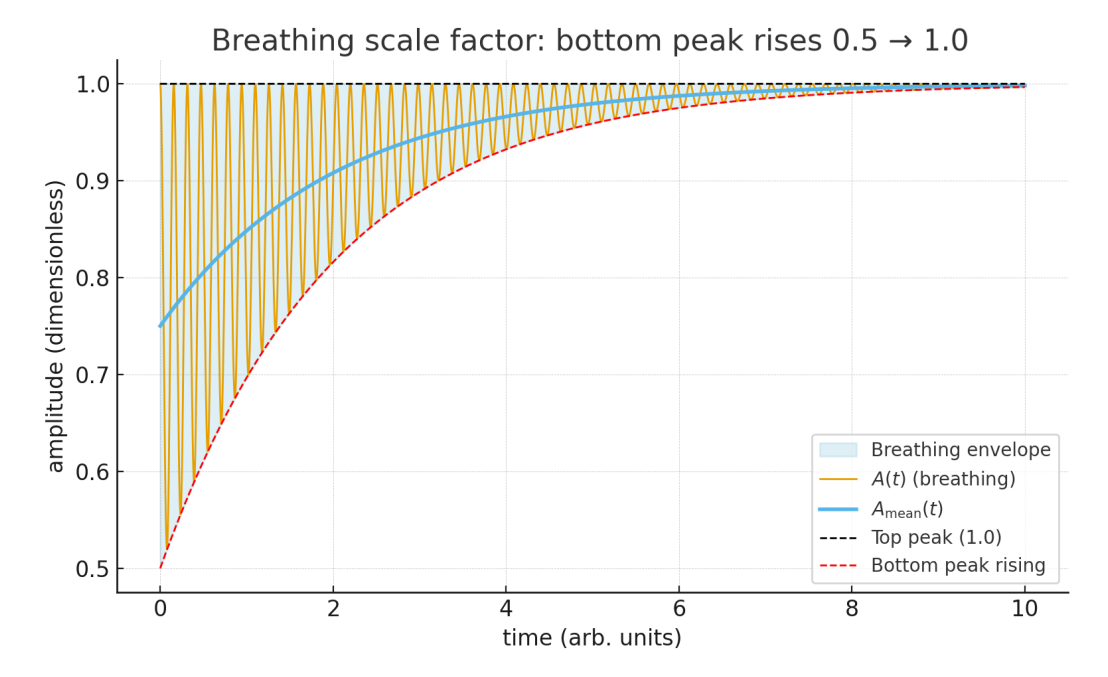


Figure 1: Schematic illustration of the breathing vacuum scale factor. The instantaneous oscillation A(t) (blue) occurs at constant frequency, bounded between a fixed top peak (dashed black) at 1.0 and a bottom peak (dashed red) that rises from 0.5 toward 1.0 as the universe evolves. The mean $A_{\text{mean}}(t)$ (orange) drifts smoothly upward, representing the cycle-averaged amplitude defined in Eq. (6). The shaded band shows the peak-to-peak breathing envelope. The dotted purple line marks the Planck floor ℓ_P , which constrains the early-time oscillations as expressed in Eq. (8). The breathing frequency is constant in physical time; the envelope narrows because the amplitude decays, not because the rate changes.

2.2 On the constancy of Planck's constant

In the breathing–vacuum framework, the apparent invariance of Planck's constant h is not an external assumption but a direct consequence of the coordinate system in which the theory is formulated. All physical motion and field interactions are described in comoving coordinates that evolve with the breathing of the vacuum itself. Quantities such as energy and time scale inversely under this motion, so that their product—the action quantum h = Et—remains invariant. In this sense, h is a dimensionless ratio when expressed in units defined by the breathing vacuum, even though it carries units in laboratory terms.

The same reasoning applies to other dimensional constants, including c and α . Each represents a fixed ratio between co-evolving quantities rather than an absolute property of a static background. Thus, the constancy of h across cosmological epochs reflects the self-consistency of the comoving vacuum description: as the vacuum expands or contracts, both the temporal and energetic measures of any process rescale in concert, preserving their product. The apparent "unchanging" value of Planck's constant in experiment therefore arises naturally within VBT, without additional postulate or fine-tuning.

Interpretation. All clocks, rulers, and physical processes are tied to the cycle-averaged vacuum amplitude $A_{\text{mean}}(t)$. In this sense it represents the effective spacetime that we inhabit: the smooth background against which the rapid Planck oscillations occur, and the reference scale for both

microscopic atomic stability and macroscopic cosmological redshift.

Dimensionless invariants. In the VBT framework, all *dimensionless* constants of nature remain fixed. For example,

$$\alpha = \frac{e^2}{4\pi\epsilon_0\hbar c}, \frac{m_e}{m_p}, g$$
-factors,

retain their observed values. This follows because laboratory rulers and clocks co-evolve with the breathing vacuum, so dimensional scales drift together while pure ratios remain unchanged.

2.3 Symmetry and gauge invariance

The vacuum breathing picture is formulated without introducing a preferred frame. The underlying dynamics are governed by an action of the form

$$S = \int d^4x \sqrt{-g} \left[-\frac{1}{4} F_{\mu\nu} F^{\mu\nu} + \mathcal{L}_{\text{matter}}(\psi, D_{\mu}\psi) \right],$$

with $g_{\mu\nu} = a^2(\tau) \eta_{\mu\nu}$ a conformally flat metric, $F_{\mu\nu} = \partial_{\mu}A_{\nu} - \partial_{\nu}A_{\mu}$, and $D_{\mu} = \partial_{\mu} + ieA_{\mu}$ the usual gauge-covariant derivative. This structure guarantees:

- Local Lorentz invariance: In conformal coordinates the metric is proportional to $\eta_{\mu\nu}$, so the light cone and causal structure are identical to special relativity. No observer can detect the background oscillation as a preferred rest frame.
- Gauge invariance: The action is invariant under the U(1) transformation $A_{\mu} \mapsto A_{\mu} + \partial_{\mu} \alpha$, $\psi \mapsto e^{-ie\alpha} \psi$. Thus charge conservation and minimal coupling are preserved exactly.
- Consistency with standard QED: At scales large compared to the Planck-frequency oscillation, the averaged dynamics reduce to Maxwell + Dirac in Minkowski space. Observable quantities therefore respect the same symmetry algebra (Poincaré \times U(1)) as conventional electrodynamics.

In this way, the vacuum breathing medium does not introduce an observable preferred frame or break gauge symmetry. The oscillatory factor $a(\tau)$ enters only through cycle-averaged effective parameters such as \hbar_{eff} and m^* , while the symmetry principles remain exact.

The Vacuum Breathing Theory was first publicly released in Rev. 1 on Zenodo [3], with subsequent revisions expanding the scope and predictions.

3 Quantum Mechanics as an Envelope on the Planck Carrier

Let $\Phi_P(t) = \omega_P t$ be the *carrier phase* of the vacuum breathing [4]. The slowly varying component of a matter wave is described as an **envelope** A, riding on the Planck carrier. We model a matter wave as a weakly detuned beat pattern riding on this carrier, consistent with the early insights of de Broglie on matter waves [5]:

$$\Psi(\mathbf{x},t) = A(\mathbf{x},t) e^{i \left[\Phi_P(t) + \varphi(\mathbf{x},t)\right]},\tag{9}$$

where:

- $A(\mathbf{x},t)$ is a slowly varying amplitude envelope.
- $\varphi(\mathbf{x},t)$ is a slowly varying phase detuning.
- The "slow" scale is many orders of magnitude below ω_P .

Applying a multiple-scale expansion to the wave equation in the conformal metric

$$\Box_q \Psi = 0, \quad g_{\mu\nu} = \Omega^2(t, \mathbf{x}) \eta_{\mu\nu},$$

and averaging over the fast carrier yields, at leading order, the Madelung form [6] of the Schrödinger equation for the envelope [7]:

$$i\hbar \,\partial_t A = -\frac{\hbar^2}{2m} \nabla^2 A + V_{\text{eff}}(\mathbf{x}) \,A,\tag{10}$$

where:

• m arises from the carrier–envelope detuning:

$$m \equiv \frac{\hbar \delta \omega}{c^2}, \quad \delta \omega = \omega_P - \omega_{\text{phase-lock}}.$$

• V_{eff} arises from spatial gradients of the amplitude suppression $\alpha(\mathbf{x})$ (i.e. curvature encoded as local reductions of the global breathing midpoint). There are no spatially varying carrier phases in VBT.

Key Point: The de Broglie relations emerge directly [5]:

$$E = \hbar \dot{\varphi}, \quad \mathbf{p} = \hbar \nabla \varphi,$$

as the slowly varying phase φ determines the beat frequency and wavenumber relative to the Planck carrier. Standing-wave conditions on A in bound states produce the quantum orbital structure, with radial nodes corresponding to vacuum-relative velocity maxima [8].

3.1 Madelung representation

Writing the complex amplitude as $A = \sqrt{\rho} e^{i\phi}$, the Schrödinger equation separates into hydrodynamic form:

$$\frac{\partial \rho}{\partial t} + \nabla \cdot (\rho \mathbf{v}) = 0, \qquad \mathbf{v} = \frac{\nabla \phi}{m}.$$
 (11)

Here $\rho = |A|^2$ acts as a probability density, while **v** plays the role of a velocity field. This reinforces the fluid analogy of the breathing vacuum substrate.

As shown in Figures 2 and 3, the Planck-frequency carrier and its slow envelope modulation produce the spatially breathing wavepacket that forms the basis for the Madelung representation.

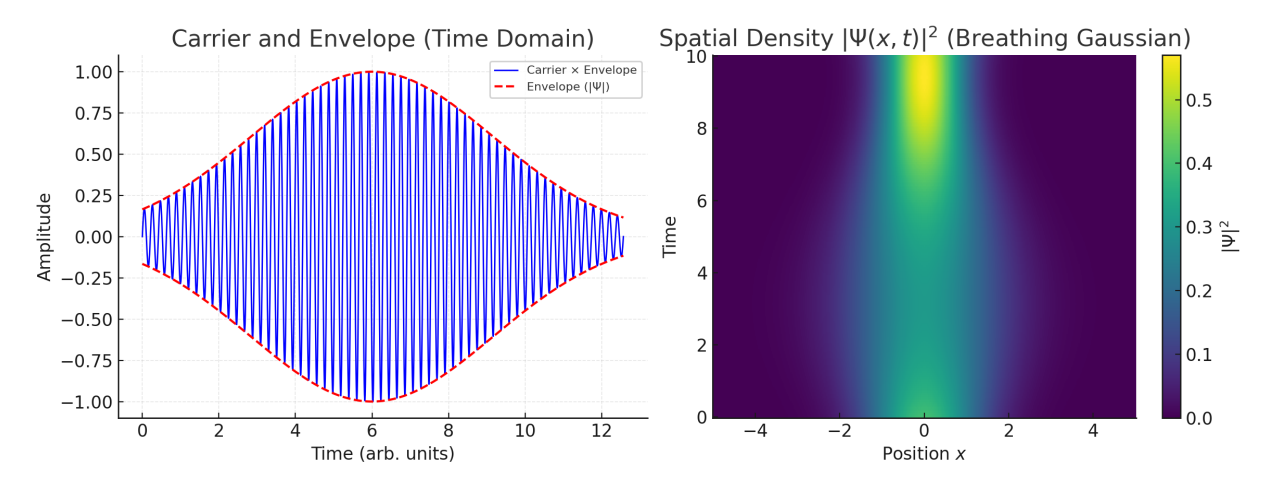


Figure 2: Left: A high-frequency Planck carrier (blue) modulated by a slower Gaussian envelope (red dashed). This illustrates the decomposition $A(t) = A_{\text{mean}}(t) \exp(\xi(t))$, where the carrier provides phase and the envelope sets $|A|^2 = \rho$. Right: Spatial probability density $|\Psi(x,t)|^2$ for a breathing Gaussian wavepacket, visualized as a function of position and time. Together these figures show how the Madelung representation naturally emerges: the envelope defines density ρ while the phase encodes velocity potential.

Breathing Gaussian Wavepacket (3D View)

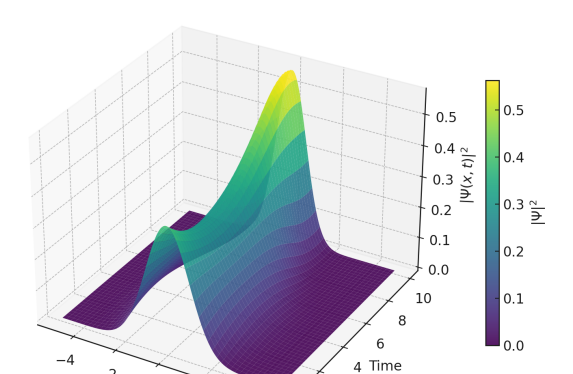


Figure 3: Three-dimensional visualization of a breathing Gaussian wavepacket. The spatial probability density $|\Psi(x,t)|^2$ evolves in time as the packet width oscillates. This illustrates the Madelung interpretation: the density $\rho = |\Psi|^2$ encodes the envelope, while the underlying Planck-frequency carrier provides the hidden phase dynamics.

Uncertainty as an Envelope Constraint: Within this framework, the Heisenberg uncertainty principle [9] arises naturally. A sharply localized envelope $A(\mathbf{x},t)$ requires broad Fourier support in $\varphi(\mathbf{x},t)$, and hence large spread in momentum:

$$\Delta x \, \Delta p \gtrsim \hbar/2.$$

Likewise, confining the envelope phase φ to a narrow frequency band implies loss of temporal localization, leading to

$$\Delta t \Delta E \gtrsim \hbar/2$$
.

Thus, uncertainty is not an abstract axiom but a direct consequence of attempting to resolve both the amplitude and the phase of the slow modulation imposed on the Planck-scale carrier. The uncertainty relation emerges as a geometric constraint [10]. The vacuum breathing provides the "hidden clock" that makes these conjugate trade-offs unavoidable [11].

While the envelope–carrier geometry provides the intuition for uncertainty, the full wave treatment reproduces the exact Robertson bound:

$$\Delta x \, \Delta p \geq \hbar/2$$
,

with equality achieved for Gaussian envelopes. Thus the heuristic picture is fully consistent with the formal operator derivation.

These complementary views (Figs. 2–3) emphasize that quantum uncertainty is a direct manifestation of the envelope–carrier decomposition of the breathing vacuum.

4 Atomic model

In this section we derive the hydrogenic bound states from the averaged vacuum dynamics, confirm the analytic distributions with numerical validation, and provide interpretive visualizations of orbital motion. Further validation examples (2s, 2p) and a higher-state illustration $(3d_{z^2})$ are included in Appendices F and A.

4.1 Setup and motivation

We consider an electron bound in the breathing vacuum, with radius $r(t) = a(t)\chi(t)$, where a(t) encodes the rapid Planck frequency oscillation and $\chi(t)$ the slow envelope. The Bohr radius a_0 and the averaged Hamiltonian derived in Sec. 4.4 provide the natural scale.

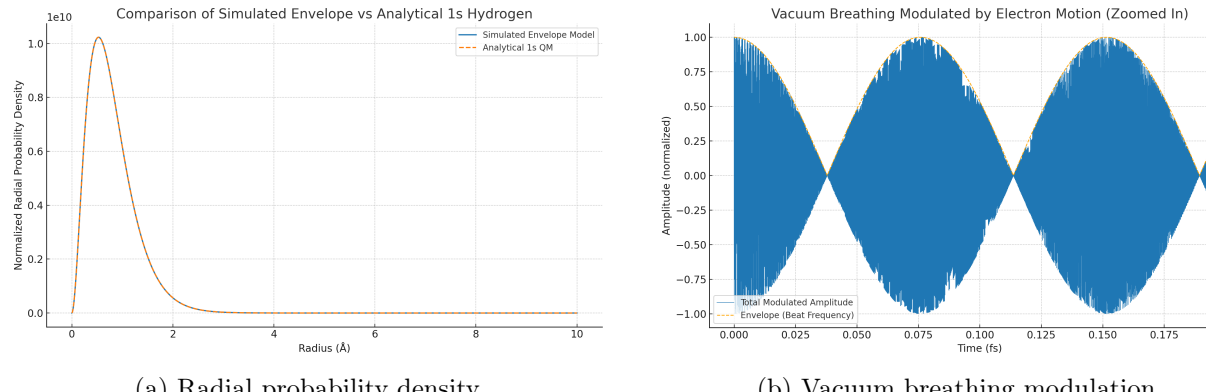
4.2 Resonance picture and factor-of-two compliance

The hydrogen atom can be interpreted as a resonance: the de Broglie frequency of the electron orbit is phase-locked to the breathing frequency of the vacuum. Expanding the modulated Coulomb force,

$$\frac{1}{\left(1 + \delta a \cos \omega t\right)^2} = 1 - 2\delta a \cos \omega t + 3\delta a^2 \cos^2 \omega t - \dots, \tag{12}$$

reveals the characteristic factor-of-two term. This is not a unique requirement but rather a compliance condition: it shows how the cycle-averaged kinetic and potential energies satisfy the virial balance implied by the averaged Hamiltonian (Sec. 4.4).

Figure 4 illustrates this compliance in two ways. Panel (a) compares a direct simulation of the radial probability density, constructed with the Bohr radius and a Coulomb force modulated at the de Broglie frequency, against the analytic 1s hydrogen distribution. The close match confirms that the resonance condition yields the correct radial statistics. Panel (b) shows the vacuum breathing amplitude (blue) together with its envelope (orange), making the factor-of-two modulation explicit. Together these plots provide a physical visualization of how the resonance picture naturally enforces stability of the ground state, consistent with the analytic derivation of Sec. 4.4.



(a) Radial probability density

(b) Vacuum breathing modulation

0.200

Figure 4: Resonance compliance in the hydrogen ground state. (a) Comparison of simulated radial distribution using Bohr radius and modulated Coulomb force at the de Broglie frequency with the analytic 1s hydrogen distribution. (b) Vacuum breathing amplitude (blue) and its envelope (orange) showing the factor-of-two modulation. These illustrate how the resonance condition enforces kinetic-potential balance, consistent with the analytic derivation in Sec. 4.4.

4.3 From conformal wave operator to envelope dynamics

Lemma 4.1 (Envelope dynamics from conformal wave operator). Consider a scalar field ϕ obeying the conformal wave equation

$$\Box_a \phi = 0, \qquad g_{\mu\nu} = a^2(t) \, \eta_{\mu\nu}, \ a(t) = 1 + \varepsilon \cos(\omega_P t), \ \varepsilon \ll 1,$$

with $\eta_{\mu\nu}$ the Minkowski metric and ω_P the fast carrier frequency. Introduce the multiple-scales ansatz

$$\phi(t, \mathbf{x}) = e^{i\omega_P t} \psi(t, \mathbf{x}) + c.c., \qquad \partial_t \psi \sim \mathcal{O}(\omega_{orb}) \ll \omega_P,$$

where ψ is a slowly varying envelope. Then, to leading order in ω_{orb}/ω_P and after averaging over the fast oscillations, ψ satisfies the Madelung form of the Schrödinger equation:

$$i \, \hbar_{eff} \partial_t \psi = -rac{\hbar_{eff}^2}{2m^*}
abla^2 \psi + V_{eff} \psi,$$

with effective parameters determined by cycle averages of the breathing factor:

$$m^* = m \langle a^2 \rangle, \qquad \hbar_{\!\!\mathit{eff}}^2 \; \propto \; m \langle \dot{a}^2 \rangle, \qquad V_{\!\!\mathit{eff}}(\mathbf{x}) = -\, rac{k^*}{r}, \quad k^* = k \, \langle a^{-1} \rangle.$$

Sketch of proof. For the conformal metric one has

$$\Box_g \phi = a^{-4} \, \partial_\mu \big(a^2 \eta^{\mu\nu} \partial_\nu \phi \big) \,.$$

Substituting the two-scale ansatz separates the fast $e^{i\omega_P t}$ carrier from the slow envelope. Expanding in ε and in $\omega_{\rm orb}/\omega_P$, then averaging over one fast period, eliminates oscillatory terms and leaves transport equations for $|\psi|^2$ and its phase $S = \arg \psi$. These combine into continuity and Euler equations with a "quantum pressure" proportional to $\langle \dot{a}^2 \rangle$. Identifying this with \hbar_{eff} reproduces the stationary Schrödinger system with effective constants as stated.

Remark. This establishes the bridge from a conformal metric with fast Planck-scale oscillations to an effective quantum envelope description. The following subsection 4.4 shows that the resulting envelope equation yields hydrogenic bound states with the correct spectrum.

4.4 Derived bound states

We now apply the envelope dynamics from Lemma 4.1 to obtain the hydrogenic spectrum. The following result makes the connection explicit.

Theorem 4.1 (Hydrogen from the averaged fabric dynamics). Under the scale separation $\omega_P \gg \omega_{orb}$ and the averaging leading to (16), the slow envelope obeys (17). Its square-integrable solutions are the hydrogenic bound states with

$$E_n = -\frac{m^* k^2}{2\hbar_{eff}^2} \frac{1}{n^2}, \qquad n = 1, 2, \dots,$$
(13)

$$a_0 = \frac{\hbar_{eff}^2}{m^* k}, \quad (Bohr \ radius \ in \ VBT), \tag{14}$$

$$R_{10}(r) = 2 a_0^{-3/2} e^{-r/a_0}, \qquad P_{1s}(r) = 4 a_0^{-3} r^2 e^{-2r/a_0},$$
 (15)

with the usual Laguerre structure and node counting for $n, \ell \geq 0$. These probability densities arise directly from the dynamics.

Sketch of proof. Starting from the averaged Hamiltonian in (16), write the ensemble density as $\rho = \psi^2$ and pass to the Madelung form. Matching the dispersive term to the stiffening $\frac{1}{2}m\Omega^2\chi^2$ identifies \hbar_{eff} . The resulting stationary radial equation is (17), whose square-integrable solutions are the hydrogenic wavefunctions with spectrum E_n .

The ground state is $\psi_{100}(r) = \frac{1}{\sqrt{\pi}a_0^{3/2}}e^{-r/a_0}$ with $E_1 = -m^*k^2/(2\hbar_{\text{eff}}^2)$. A representative excited state is 2p $(n=2, \ell=1)$, with radial part $R_{21}(r) = \frac{1}{2\sqrt{6}}a_0^{-3/2}(r/a_0)e^{-r/(2a_0)}$ and the standard angular factor $Y_{1m}(\theta, \phi)$. These reproduce the measured transition energy and the dipole selection rules when coupled to the electromagnetic sector.

We write the physical radius as $r(t) = a(t) \chi(t)$, where the rapid breathing factor is $a(t) = 1 + \varepsilon \cos(\omega_P t)$ with $\varepsilon \ll 1$ and ω_P much larger than any orbital frequency. Averaging over the fast phase gives the slow effective Hamiltonian for the comoving coordinate χ :

$$H_{\text{eff}}(\chi, p_{\chi}) = \frac{p_{\chi}^2}{2m^*} - \frac{k^*}{\chi} + \frac{1}{2} m \Omega^2 \chi^2, \qquad m^* \equiv m \langle a^2 \rangle, \ k^* \equiv k \langle a^{-1} \rangle, \ \Omega^2 \equiv \langle \dot{a}^2 \rangle. \tag{16}$$

Here $k \equiv k_e e^2$ (energy–length units) and $\langle \cdot \rangle$ denotes the cycle average.

Hydrogenic radial equation. Consider a compressible ensemble of slow trajectories with density $\rho(\chi,t)$ and velocity $u=\dot{\chi}$. Writing $\rho=\psi^2$ and choosing a constant $\hbar_{\rm eff}$ so that the dispersive (quantum-pressure) term matches the stiffening $+\frac{1}{2}m\Omega^2\chi^2$ in (16), the Euler-continuity system becomes equivalent to the stationary Schrödinger equation in the physical radius $r=a\chi$:

$$-\frac{\hbar_{\text{eff}}^2}{2m^*} \frac{d^2 u}{dr^2} + \left[-\frac{k}{r} + \frac{\hbar_{\text{eff}}^2 \ell(\ell+1)}{2m^* r^2} \right] u = E u, \qquad u(r) = r R(r).$$
 (17)

Orbital angular momentum. Equation (17) naturally includes the angular momentum barrier term $\ell(\ell+1)/r^2$, showing that the averaged dynamics support not only radial quantum numbers n but also orbital angular momentum quantum numbers ℓ . The presence of this term ensures that the VBT framework reproduces the full hydrogenic spectrum, including the splitting between s, p, d, and higher orbitals. Physically, ℓ corresponds to the electron's shuttle precession within the breathing

substrate, and the associated orbital magnetic moment arises directly from this motion. The detailed derivation of the angular momentum contribution, including its emergence from multiple-scales averaging, is provided in Appendix B.

Spectrum and scales. Square-integrable solutions of (17) yield the hydrogenic levels and length scale

$$E_n = -\frac{m^* k^2}{2\hbar_{\text{eff}}^2} \frac{1}{n^2}, \qquad n = 1, 2, \dots$$
 (18)

$$a_0 = \frac{\hbar_{\text{eff}}^2}{m^* k},\tag{19}$$

with the usual Laguerre structure for $R_{n\ell}(r)$. In particular, the ground-state radial probability density is

$$P_{1s}(r) = 4 a_0^{-3} r^2 e^{-2r/a_0}. (20)$$

Comment. Equations (16)–(20) show that hydrogenic bound states arise directly from the averaged dynamics; no constructive fit is required. The resonance picture in Sec. 4.2 provides an illustrative compliance check with the virial balance, and Sec. 4.6 establishes that these stationary states are non-radiating [Eq. (21)].

4.5 Validation by numerical check

To confirm the analytic distributions, an inverse-CDF trajectory generator was implemented. Figure 5 shows the histogram for the 1s state, which closely matches Eq. (20). Additional validations for the 2s and 2p states are presented in Appendix F, where the simulation method is also described in detail.

4.6 Non-radiation of stationary states

A longstanding classical problem is that an electron in orbital motion should radiate Larmor power continuously, destabilizing atoms. Bohr resolved this by postulating stationary states that do not radiate, but the mechanism was left unexplained. In VBT, the mechanism is explicit.

Stationary orbits are phase-locked to the global Planck-frequency carrier. In this locked configuration the electron's velocity relative to the breathing vacuum is periodic, and the cycle-averaged far-field Poynting flux vanishes:

$$\langle P \rangle \equiv \lim_{R \to \infty} \frac{1}{T} \int_0^T dt \oint_{S_R^2} \mathbf{S} \cdot d\mathbf{A} = 0.$$
 (21)

Thus, no net radiation escapes from a stationary state.

Larmor radiation The absence of Larmor radiation follows naturally: a bound electron is an envelope locked to the breathing vacuum and does not produce secular acceleration in the external frame. Only when the locking condition is broken—during a transition—does radiation occur, corresponding to photon emission or absorption. This replaces Bohr's ad hoc postulate with a dynamical explanation grounded in the VBT framework.

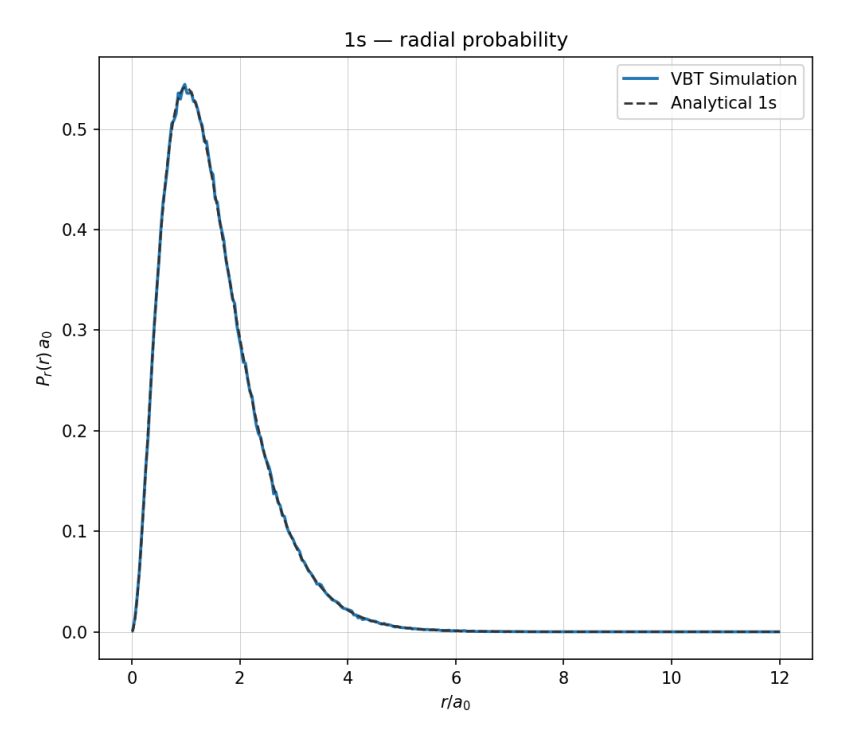


Figure 5: Numerical validation of the 1s radial distribution. Histogram of simulated radii r(t) from inverse-CDF sampling compared with the analytic $P_{1s}(r)$. The close agreement confirms the analytic result. Additional 2s and 2p validations appear in Appendix F.

4.7 Interpretive illustrations

Beyond the analytic densities of Sec. 4.4, it is helpful to visualize trajectories in the breathing-vacuum picture. The following figures 6, 7 are *interpretive illustrations*, intended to provide physical intuition for orbital motion and probability distributions. They are not independent derivations but are consistent with the analytic framework.

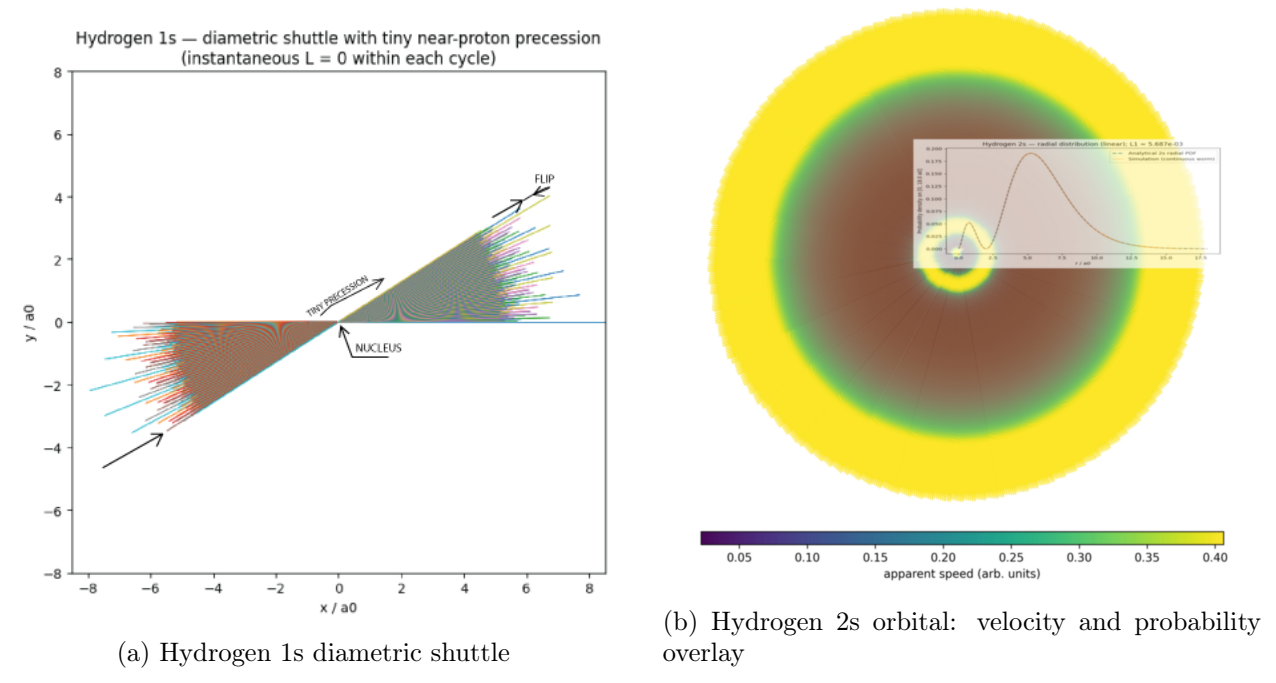


Figure 6: Illustrative visualizations of hydrogen states. (a) The 1s state as a diametric shuttle with near-proton precession. (b) The 2s state with apparent velocity shown in color, overlaid with the analytic radial probability density. These are illustrative only, consistent with analytic results.

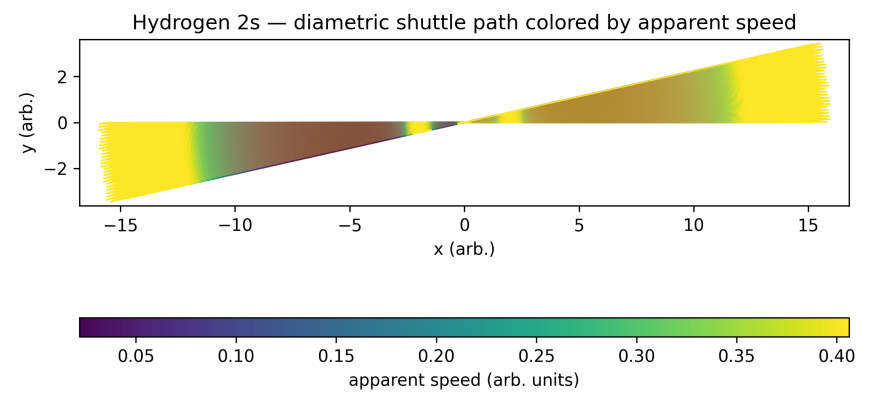


Figure 7: **Hydrogen** 2s diametric shuttle colored by speed. Shuttle trajectory with apparent velocity shown in color. The nodal region is visible as a velocity minimum. This is an illustrative consistency check with the analytic 2s distribution.

5 Orbital Transitions in the Breathing Vacuum

In the Vacuum Breathing Theory (VBT) [3], electrons in bound states are represented as loop oscillations phase-locked to the global Planck-frequency carrier. Each orbital corresponds to a distinct detuning condition between the loop and the carrier, producing the discrete hydrogenic levels of Sec. 4. Orbital transitions arise when the loop re-locks from one detuning to another, with photon emission or absorption occurring during this continuous re-synchronization.

5.1 Continuous re-locking dynamics

A transition $i \to f$ is described as a finite-duration re-locking event. Initially, the loop is stabilized at frequency ν_i , but when driven out of its locking range it migrates smoothly toward the final resonance at ν_f . During the overlap interval, both frequency components coexist and the dipole moment oscillates at their difference frequency. This generates radiation with energy

$$hf_{\gamma} = E_i - E_f, \tag{22}$$

where f_{γ} is the photon frequency. Thus, the discreteness of the spectrum arises from the stable endpoints, while the emission process itself is continuous, governed by the dynamics of re-locking.

5.2 Spontaneous Emission in VBT

In the conventional QED framework, spontaneous emission is treated as a probabilistic process: the atom in an excited state decays randomly, emitting a photon wavepacket with an exponential probability law and no memory of prior history. The emitted packet is typically modeled as a single-frequency mode truncated by exponential decay.

Within the VBT framework, the picture is deterministic and continuous. Emission occurs when the self-looped oscillation of the electron re-locks from one orbital breathing mode to another. Rather than an instantaneous jump, the transition requires a finite re-phasing period with the universal vacuum oscillation. This produces a photon packet with three characteristic features:

- 1. Causal delay: the emission onset occurs at $t_0 + \Delta t$, with $\Delta t > 0$ representing the re-locking time. No photon can emerge before re-alignment is established.
- 2. **Finite packet envelope:** the photon wave is not memoryless, but bounded in time, with a Gaussian- or sinc-like profile. This contrasts with the exponential tail of QED.
- 3. **Frequency chirp:** during the re-locking, the emitted frequency sweeps slightly as the system interpolates between the initial and final orbital frequencies.

These distinctions are illustrated in Fig. 8(a) showing the envelope comparison: a QED exponential (convolved with detector response) versus the VBT delayed packet. Figure 8(b) shows the instantaneous frequency, constant in QED but chirped under VBT. Together, these plots summarize the unique observational fingerprints of VBT.

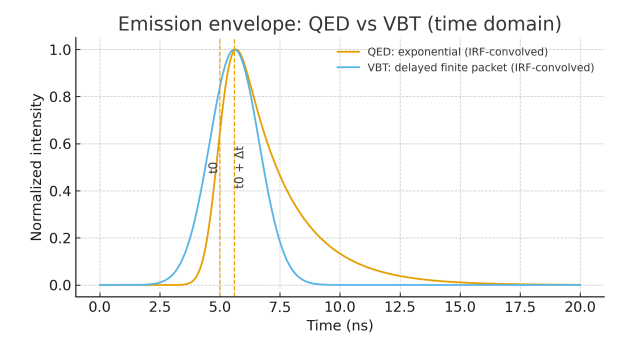
The causal delay Δt is not arbitrary, but scales with the ratio of coupling strength Ω to phase mismatch $|\alpha|$. This scaling law is displayed in Fig. 9, which serves as a direct falsifiability test. Observation of a linear relation between Δt and $\Omega/|\alpha|$ would strongly support VBT, whereas a null result would reinforce the standard QED model.

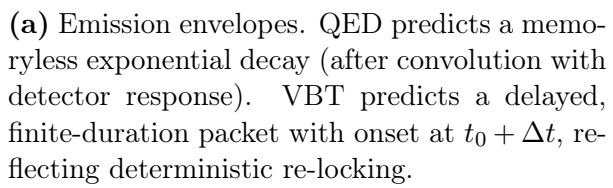
In this way, spontaneous emission ceases to be a stochastic "collapse" and becomes a deterministic consequence of vacuum re-locking. The predictions of VBT are therefore both sharper and more falsifiable than those of QED, inviting direct time-resolved experimental tests. As a quantitative test, VBT predicts a linear relation $\Delta t \propto \Omega/|\alpha|$ (Fig. 9), allowing a direct falsification experiment through controlled sweeps of coupling and detuning rate.

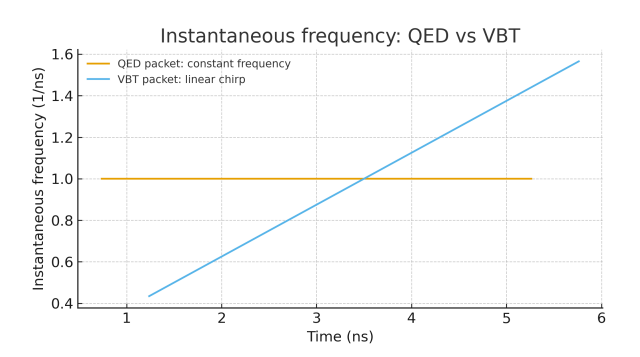
5.3 Spectral line reproduction

Because VBT reduces to the hydrogenic bound-state energies,

$$E_n = -\frac{me^4}{8\varepsilon_0^2 h^2 n^2},\tag{23}$$







(b) Instantaneous frequency. QED emission remains constant-frequency, whereas VBT predicts a chirp: the frequency sweeps as the electron re-locks to the vacuum breathing mode.

Figure 8: Spontaneous emission predictions in QED versus VBT. Together, panels (a) and (b) illustrate the two key distinctions: causal delay and frequency chirp, both of which are experimentally accessible.

the transition frequencies

$$f_{n_i \to n_f} = \frac{E_{n_i} - E_{n_f}}{h} \tag{24}$$

reproduce the Rydberg formula and therefore the observed Balmer, Lyman, and higher spectral series. VBT explains not only the line positions but also the temporal mechanism by which they arise.

5.4 Selection rules from vacuum geometry

The effective coupling operator induced by the breathing modulation is

$$\hat{V} \propto e \, \mathbf{r} \cdot \mathbf{E}$$
.

which is odd under spatial inversion. As in conventional dipole theory, this implies $\Delta \ell = \pm 1$ and $\Delta m = 0, \pm 1$. Thus the electric-dipole selection rules emerge naturally from the symmetry of the vacuum drive. Higher-order terms in the expansion of the modulation produce quadrupole (E2) and magnetic-dipole (M1) contributions, explaining the existence but suppression of forbidden lines.

5.5 Natural linewidth and lineshape

The finite re-locking time τ determines the duration of photon emission. The resulting linewidth is

$$\Delta f \sim \frac{1}{2\pi\tau}.\tag{25}$$

The $2p \to 1s$ transition has a natural lifetime of $\sim 1.6\,\mathrm{ns}$, corresponding to a linewidth of order 100 MHz [12]. By contrast, the metastable $2s \to 1s$ two-photon decay is far slower ($\tau \approx 0.12\,\mathrm{s}$) [13], serving as a benchmark against which line broadening mechanisms are tested.

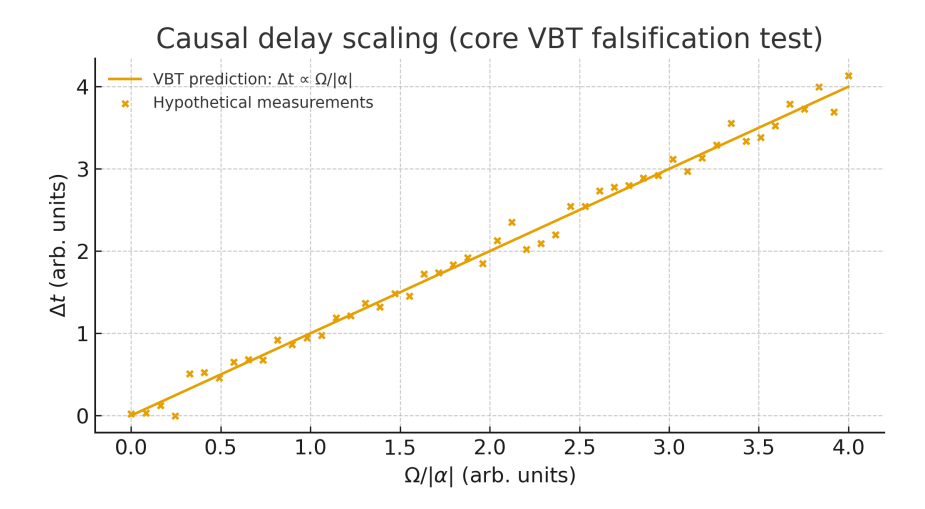


Figure 9: Causal delay scaling predicted by VBT: Δt increases linearly with the ratio $\Omega/|\alpha|$. Absence of linear scaling under parameter sweeps would falsify the VBT transition model.

5.6 Lamb shift as high-frequency modulation

The Lamb shift—a small splitting between $2s_{1/2}$ and $2p_{1/2}$ levels—was first measured by Lamb and Retherford in 1947 [14], and has since been refined by high-precision spectroscopy [15]. It is explained in VBT as a deterministic consequence of residual high-frequency modulation in the breathing carrier. When orbital timescales are averaged, these ultrafast components act as an effective short-range perturbation of the Coulomb potential:

$$\delta V(\mathbf{r}) \propto \lambda_{\text{VBT}} \, \delta^{(3)}(\mathbf{r}).$$
 (26)

analogous to the Darwin or Fermi contact terms in quantum mechanics. Because only s orbitals have finite amplitude at the origin, this perturbation shifts their energies relative to higher ℓ states. The correction scales with the probability density at the nucleus, $|\psi_{n0}(0)|^2 \propto n^{-3}$, producing the characteristic $1/n^3$ dependence familiar from fine- and hyperfine-structure splittings. In the VBT picture, this local δ -like term represents the compressive response of the vacuum's elastic amplitude field when the bound charge oscillates faster than the mean coherence rate $f_{\rm Planck}$. The effect is therefore a direct expression of vacuum elasticity at atomic scales, rather than a purely relativistic correction.

This correction shifts s-orbitals relative to p-orbitals with the characteristic $1/n^3$ scaling. Unlike conventional QED, which appeals to vacuum fluctuations, VBT ties the Lamb shift directly to coherent but unresolved Planck-scale structure of the breathing vacuum. This provides a deterministic physical origin for the observed energy correction.

5.7 Impact of breathing waveform symmetry

In the simplest implementation of VBT, the vacuum breathing is modeled as a sinusoidal oscillation,

$$A(t) = A_{\text{mean}} + A_0 \cos(\omega_P t),$$

with ω_P the Planck frequency. This choice enforces perfect symmetry between "in" and "out" phases of the oscillation and produces a single carrier tone without higher harmonics. Electrons

then couple to this fundamental drive, leading directly to the quantized detuning conditions and hydrogenic spectrum described above.

If the breathing waveform is not perfectly sinusoidal but slightly asymmetric—analogous to mammalian respiration with faster inspiration and slower expiration—then the drive contains higher harmonics at $2\omega_P$, $3\omega_P$, and so on. These additional Fourier components do not disrupt the primary resonance structure but act as weak secondary drives. Their effect would be to:

- introduce small sideband-like corrections to orbital detuning conditions,
- enhance higher-order multipole couplings relative to the pure sinusoidal model, and
- generate line shifts and wings consistent with what are observed as Lamb shift corrections and fine-structure anomalies.

In this view, the Lamb shift emerges not from stochastic fluctuations but as a deterministic consequence of residual harmonic content in the breathing waveform. The sinusoidal model therefore captures the leading-order atomic spectrum, while the more realistic asymmetric waveform encodes subtle deviations. High-precision spectroscopy thus becomes a probe not only of the breathing frequency but also of the waveform symmetry of the vacuum fabric itself.

5.8 Forbidden transitions

The electric–dipole selection rules derived above forbid the single-photon $2s \to 1s$ decay, since both states have $\ell=0$ and $\Delta\ell=\pm 1$ is required for a single E1 transition. In hydrogen, this decay proceeds instead through a second–order two–photon process. The general form of the matrix element can be written schematically as

$$M_{2\gamma} \propto \sum_{n} \frac{\langle 1s|r|n\rangle\langle n|r|2s\rangle}{E_{2s} - E_n - \hbar\omega_1},$$
 (27)

which represents the virtual coupling of the 2s and 1s states through intermediate np configurations and the sequential emission of two photons with frequencies ω_1 and ω_2 satisfying $\omega_1 + \omega_2 = \omega_{21}$.

The explicit, symmetrized amplitude is

$$\mathcal{M}_{2\gamma}(\omega_1) = \sum_{n} \left(\frac{\langle 1s | \mathbf{r} \cdot \boldsymbol{\epsilon}_2 | np \rangle \langle np | \mathbf{r} \cdot \boldsymbol{\epsilon}_1 | 2s \rangle}{E_{2s} - E_{np} - \hbar \omega_1} + \frac{\langle 1s | \mathbf{r} \cdot \boldsymbol{\epsilon}_1 | np \rangle \langle np | \mathbf{r} \cdot \boldsymbol{\epsilon}_2 | 2s \rangle}{E_{2s} - E_{np} - \hbar \omega_2} \right), \tag{28}$$

which is symmetric under exchange $\omega_1 \leftrightarrow \omega_2$ and $\epsilon_1 \leftrightarrow \epsilon_2$. Summation runs over the complete set of discrete and continuum np states that mediate the two E1 couplings. The corresponding differential rate takes the form

$$\frac{d\Gamma_{2\gamma}}{d\omega_1} = \mathcal{N}\,\omega_1^3 \omega_2^3 \big| \mathcal{S}(\omega_1) \big|^2, \qquad \omega_2 = \omega_{21} - \omega_1, \tag{29}$$

where $S(\omega_1)$ is the reduced sum over intermediate states and \mathcal{N} is a constant prefactor. The $\omega_1^3 \omega_2^3$ dependence arises from the E1×E1 dipole and phase–space factors, producing a nearly symmetric spectrum peaked at $\omega_1 \approx \omega_2 \approx \frac{1}{2}\omega_{21}$. Integration over all frequencies gives the well–known lifetime

$$\tau_{2s}^{-1} = \Gamma_{2\gamma}(2s \to 1s) \approx 8.2 \text{ s}^{-1}, \qquad \tau_{2s} \approx 0.12 \text{ s},$$
 (30)

in excellent agreement with experiment.

VBT interpretation (re-locking). Within the Vacuum Breathing framework, the two-photon decay corresponds to a second-order re-locking of the bound vacuum envelope. The dipole operator \mathbf{r} couples the 2s breathing mode to transient p-like distortions of the elastic vacuum field. Because a single photon cannot mediate an $s \to s$ transition, the system relaxes through two successive partial emissions that together restore phase coherence between the 2s and 1s envelopes. Each photon carries roughly half the energy gap, and the symmetric $\omega_1 \leftrightarrow \omega_2$ form of Eq. (28) expresses that the re-locking can proceed in either temporal order. The observed lifetime thus emerges naturally from the same dipole coupling that governs allowed lines, suppressed only by the absence of a direct one-photon path. Even this highly forbidden decay therefore fits coherently within the VBT picture of quantized vacuum-field elasticity.

5.9 Summary

In VBT, orbital transitions are unified under a single deterministic mechanism:

- Emission and absorption are continuous re-locking events rather than postulated jumps.
- The hydrogenic spectrum arises naturally from the resonance conditions.
- Selection rules follow from the parity of the coupling operator.
- Linewidths reflect finite re-locking times, with potential precision tests in lineshape details.
- The Lamb shift is explained by high-frequency residual modulation of the carrier, not stochastic fluctuations.
- Forbidden transitions are accounted for by higher-order re-locking processes such as twophoton emission.

This framework positions atomic spectroscopy as a direct probe of the coherent microstructure of the vacuum fabric, with predictive power extending from line centers and widths to subtle corrections such as the Lamb shift and rare decays. A dedicated experimental proposal describing how these predictions can be tested with trapped ions and time-correlated single-photon counting has been published separately [16].

6 Quantum Effects Beyond Atomic Transitions

Up to this point, we have shown that the Vacuum Breathing Theory (VBT) reproduces the discrete structure of atomic spectra and explains orbital transitions as deterministic re-locking events (5.1). In conventional physics, however, the strangeness of quantum mechanics is not confined to atoms. Phenomena such as tunneling, Dirac quasiparticles, the quantum Hall effect, and mesoscopic delocalization are often portrayed as emergent or purely probabilistic.

VBT offers a unifying alternative: all of these effects trace back to the *phase relationship* between local matter oscillations and the universal Planck-frequency breathing of the vacuum.

- Effective mass becomes the degree of mismatch in this lock.
- Tunneling times reflect the finite delays required to re-lock at interfaces.
- Quantized transport emerges as integer or rational ratios of cyclotron motion to vacuum breathing cycles.

• Macroscopic coherence is capped by the de Broglie wavelength, set by the same locking principle.

In this way, quantum "mysteries" become deterministic consequences of a single mechanism—synchronization with the breathing vacuum.

6.1 Dirac Points and Massless Excitons

In quantum materials, certain quasiparticles propagate as if they have no mass. The most famous example is graphene, where electrons near the Dirac point obey a linear dispersion relation

$$E = \hbar v_F k,\tag{31}$$

with group velocity close to the Fermi velocity v_F . In this regime, electrons move like relativistic fermions despite being embedded in a lattice potential. Experimental confirmation was first reported by Novoselov *et al.* [17], and extended to other systems such as topological insulators and transition-metal dichalcogenides.

More recently, massless exciton branches have been identified in monolayer hexagonal boron nitride (hBN) using Q-EELS and RIXS measurements. These reveal dispersion relations consistent with quasi-relativistic behavior, with group velocities approaching $10^{-3}c$ [18, 19].

Conventional interpretation. Such massless behavior is usually attributed to band-structure symmetries—specifically the degeneracy and linear crossing at Dirac points.

VBT interpretation. In the breathing-vacuum framework, effective mass is not intrinsic but arises from a residual phase mismatch between local oscillations and the global Planck carrier. At a Dirac point, or in excitonic exchange conditions that restore symmetry, this mismatch vanishes:

$$m_{\rm eff} \propto \Delta \phi,$$
 (32)

where $\Delta \phi$ is the phase detuning from perfect lock. When $\Delta \phi = 0$, the local oscillation is exactly synchronized with the vacuum breathing, inertia cancels, and the particle propagates as massless.

Prediction. If effective mass is a direct measure of phase mismatch, then external perturbations that alter coupling strength—such as strain, dielectric screening, or applied fields—should tune $\Delta \phi$ continuously. VBT therefore predicts that materials can be driven smoothly between massive and massless regimes, not just through discrete symmetry points.

Illustrative picture. Figure 10 presents an illustrative VBT diagram of effective mass as a function of phase mismatch. At perfect lock, the curve passes through zero, providing a mechanistic basis for the linear dispersions observed in graphene and hBN, thereby connecting them to the same fundamental principle that governs atomic bound states.

6.2 Tunneling as Deterministic Re–Locking

In the standard quantum picture, a particle with energy $E < V_0$ crosses a potential barrier of height V_0 with a transmission probability set by the under-barrier exponential, while the notion of a tunneling time is ambiguous and admits several inequivalent definitions (phase time, dwell time, Larmor clock, etc.). The question of how to define tunneling times has been long debated [20, 21].

Within VBT, the process acquires a clear mechanistic decomposition: tunneling consists of a finite under-barrier dwell plus two interface re-locking delays, required for the envelope to resynchronize with the universal breathing when entering and exiting the classically forbidden region. The total time is therefore

$$\tau_{\rm VBT} = \tau_{\rm BL} + 2\tau_{\rm lock},\tag{33}$$

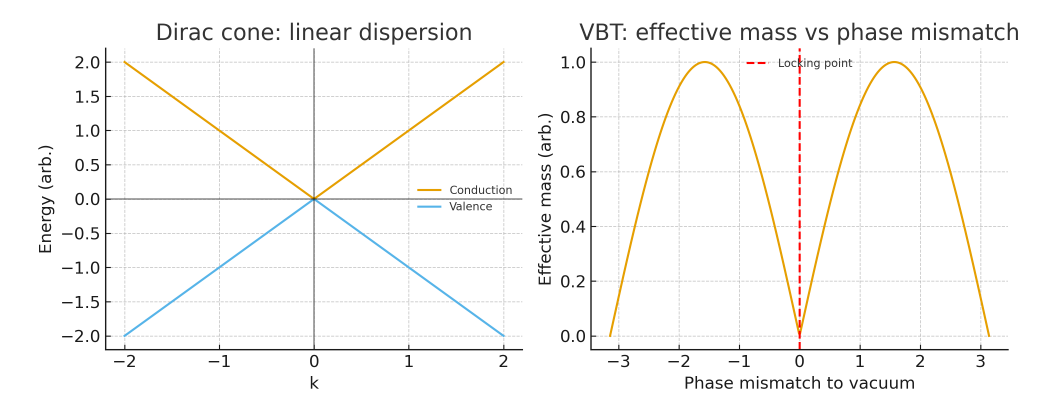


Figure 10: Effective mass as phase mismatch. Left: Dirac cone dispersion in graphene, where electrons behave as if massless near the crossing. Right: VBT cartoon showing effective mass as a function of phase mismatch $\Delta \phi$ relative to the vacuum breathing. At $\Delta \phi = 0$, the effective mass vanishes.

where $\tau_{\rm BL}$ is the Büttiker–Landauer traversal time through the interior of the barrier and $\tau_{\rm lock}$ is a positive, interface–localized re–phasing delay.

Baseline (under-barrier) time. For a one-dimensional rectangular barrier of width a and height V_0 , define

$$\kappa \equiv \frac{\sqrt{2m(V_0 - E)}}{\hbar}, \qquad \tau_{\rm BL} \approx \frac{m a}{\hbar \kappa},$$
(34)

which coincides with the canonical Büttiker-Landauer dwell/traversal scale inside the barrier.²

Interface re-locking. At each edge, the envelope must adjust its phase relative to the breathing vacuum as the local dispersion switches from oscillatory to evanescent (and back). Let Ω denote an effective local coupling strength (i.e. the rate governing phase attraction to the breathing), $v_{\rm in}$ the incident group velocity, and let $d\Delta/dx$ encode the spatial rate of change of the detuning parameter $\Delta(x)$ across an interface of characteristic sharpness $\ell_{\rm edge} \sim |d\Delta/dx|^{-1}$. Then a generic, dimensionally consistent estimate for the deterministic re-lock delay is

$$\tau_{\rm lock} \simeq c_1 \frac{\hbar \Omega}{v_{\rm in}} \left| \frac{d\Delta}{dx} \right|^{-1} \sim c_1 \frac{\hbar \Omega \ell_{\rm edge}}{v_{\rm in}},$$
(35)

with $c_1 = \mathcal{O}(1)$. Sharper interfaces (smaller ℓ_{edge}) reduce the delay, while stronger phase–attraction Ω and slower incidence v_{in} increase it. The timing decomposition is summarized schematically in Figure 11, where the total traversal time $\tau_{\text{VBT}} = \tau_{\text{BL}} + 2\tau_{\text{lock}}$ is shown as the sum of an under-barrier dwell and two positive interface delays.

Theorem 6.1 (Deterministic composition of tunneling time). For a barrier with smooth but finite interfaces, the VBT tunneling time decomposes as in (33) with τ_{BL} given by (34) and τ_{lock} by (35). Moreover, $\tau_{lock} > 0$ generically and depends only on local interface properties (to leading order), whereas τ_{BL} depends on the barrier interior.

²We use the conventional BL estimate as the under–barrier baseline; alternative definitions differ by factors of order unity in the opaque limit.

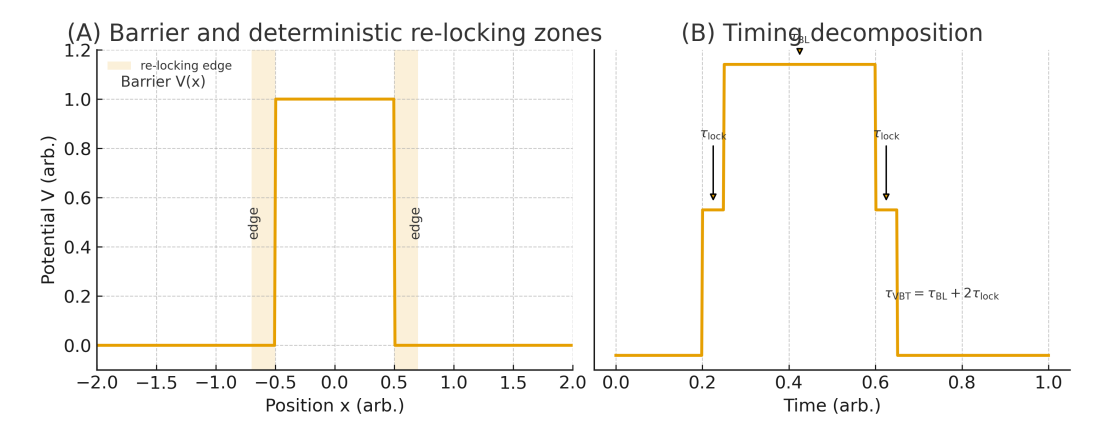


Figure 11: Timing decomposition in VBT tunneling. Left: rectangular barrier with shaded interface layers of thickness ℓ_{edge} where deterministic re–locking occurs. Right: timing budget—the total τ_{VBT} equals a Büttiker–Landauer under–barrier dwell plus two positive interface delays.

Sketch of proof. Write the envelope on each region (free, evanescent, free) and impose VBT's phase-locking dynamics at the interfaces: the slow phase ϕ obeys a relaxation $\dot{\phi} = -\Omega \Delta$ while $\Delta(x)$ changes from real to imaginary wavevector mismatch across a spatial layer of thickness $\ell_{\rm edge}$. Integrating the relaxation across the layer yields a finite re-phasing time proportional to $\hbar\Omega \ell_{\rm edge}/v_{\rm in}$. Inside the barrier, the conserved probability current and evanescent density give the BL dwell $ma/(\hbar\kappa)$. Adding the two interface contributions produces (33).

Worked example (opaque but not extreme). For electrons with $E=0.5\,\mathrm{eV}$ incident on a $V_0=1.0\,\mathrm{eV}$ rectangular barrier of width $a=1\,\mathrm{nm}$, one finds $\tau_{\mathrm{BL}}\approx 2.4\,\mathrm{fs}$. Taking an interface sharpness $\ell_{\mathrm{edge}}=0.1\,\mathrm{nm}$, incident $v_{\mathrm{in}}\approx 6.6\times 10^5\,\mathrm{m/s}$, and an effective coupling $\Omega=2\pi\times 50\,\mathrm{THz}$ gives $\tau_{\mathrm{lock}}\approx 98\,\mathrm{attoseconds}$ per edge, hence

$$\tau_{\rm VBT} \approx 2.4 \, \text{fs} + 0.20 \, \text{fs} = 2.6 \, \text{fs},$$

an $\approx 8\%$ positive excess over the BL baseline—well within modern attosecond timing reach.

Predictions and falsifiability.

- 1. Positive excess delay. $\tau_{\rm VBT} \tau_{\rm BL} > 0$ for generic interfaces; superluminal or negative times are excluded by construction.
- 2. Interface locality. Modifying only the edge sharpness ℓ_{edge} changes τ_{lock} while leaving τ_{BL} essentially unchanged.
- 3. Linear tunability. $\tau_{\text{lock}} \propto \Omega$ and $\tau_{\text{lock}} \propto \ell_{\text{edge}}$; $\tau_{\text{lock}} \propto 1/v_{\text{in}}$. Sharper edges and faster incidence reduce the delay; stronger coupling increases it.
- 4. Opaque limit continuity. In the $\kappa a \gg 1$ limit, $\tau_{\rm BL}$ dominates while $2\tau_{\rm lock}$ remains a finite offset set by interface microphysics.

Interpretation. Classical paradoxes (instantaneous or negative tunneling times) arise when the interface dynamics are omitted. VBT restores causality by recognizing that an envelope locked to the breathing vacuum must spend a finite time re—synchronizing whenever the local dispersion changes character. The result, Eq. (33), is experimentally sharp (attosecond—resolvable), tunable at the barrier edges, and cleanly separable from the under—barrier dwell—providing a direct falsifiability channel for the VBT mechanism.

6.3 Bridge to Broader Quantum Properties

Having examined Dirac quasiparticles, superconductivity, and tunneling, it becomes clear that these effects are not isolated curiosities. They share a common origin in the Vacuum Breathing Theory: the synchronization (or desynchronization) of local oscillations with the Planck-scale breathing of the vacuum.

Unifying themes.

- Mass suppression. At Dirac points, inertia vanishes because the local detuning $\Delta \phi$ is zero; in superconductors, the entire condensate minimizes $\langle \Delta \phi \rangle$, yielding massless collective transport.
- Causal traversal. In tunneling, apparent paradoxes in traversal time are resolved once finite re–locking delays at interfaces are recognized; causality is restored by the same synchronization principle.
- Phase coherence as a resource. Each phenomenon reflects the degree to which matter waves retain coherence with the vacuum substrate. Where the lock is perfect, transport is frictionless; where it must be re–established, finite delays or limits appear.

Interpretation. In standard quantum mechanics, these domains (band theory, BCS condensation, tunneling) are treated with different formalisms. Within VBT, they are understood as different facets of a single mechanism: the breathing vacuum enforces discrete and causal outcomes by acting as a universal reference clock for all matter waves.

This bridge perspective highlights that subsequent phenomena—quantized Hall transport and macroscopic delocalization—are not exceptions, but natural extensions of the same deterministic phase—locking principle.

6.4 Quantum Hall Effect as Vacuum Phase–Locking

The integer quantum Hall effect was first reported in 1980 [22], and later extended to graphene with massless Dirac fermions [23]. This discovery revealed an unexpected quantization of conductance:

$$\sigma_{xy} = \nu \frac{e^2}{h}, \qquad \nu \in \mathbb{Z} \text{ or } \mathbb{Q},$$
 (36)

where ν is an integer (IQHE) or rational fraction (FQHE). This quantization is observed with remarkable precision, independent of sample quality, geometry, or material details, and has become the basis of the resistance standard.

Conventional interpretation. In the standard framework, integer QHE is attributed to Landau quantization of cyclotron orbits in a two–dimensional electron gas under high magnetic fields, while the fractional QHE is explained by electron–electron interactions forming correlated

states with emergent quasiparticles of fractional charge. Topological invariants (Chern numbers) are invoked to account for the extraordinary robustness of the quantized plateaus.

VBT interpretation. From the perspective of the breathing vacuum, Hall quantization arises from a deterministic *locking ratio* between the cyclotron frequency ω_c of electrons in the magnetic field and the Planck–frequency breathing ω_P of the vacuum substrate. Ordinary conduction corresponds to a quasiperiodic mismatch; quantization occurs whenever the ratio satisfies

$$\frac{\omega_c}{\omega_P} = \frac{p}{q}, \qquad p, q \in \mathbb{Z}, \tag{37}$$

so that the envelope of electron motion phase—locks to the breathing grid.

- For q = 1, one obtains integer plateaus: each cyclotron orbit encloses an integer number of breathing cycles.
- For q > 1, fractional plateaus appear: the condensate resonates with the vacuum after q cyclotron periods, manifesting as effective fractional charge carriers.

Robustness and topology. In this view, the celebrated robustness of QHE is not mysterious: phase–lock to the vacuum breathing is insensitive to microscopic disorder, provided the locking ratio p/q is preserved. The role of topology in conventional treatments corresponds, in VBT language, to the global constraint that the vacuum grid enforces across the entire two–dimensional sheet.

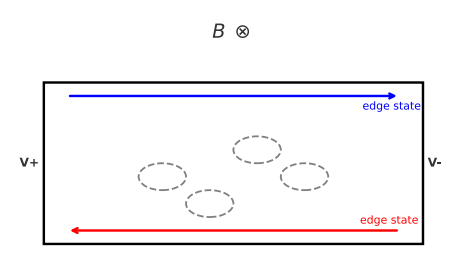
Prediction. VBT predicts that if the QHE reflects deterministic phase–locking, then small perturbations to the local vacuum coupling should modulate the widths and robustness of Hall plateaus, even while the quantized values $\nu e^2/h$ remain exact. Existing experiments are already consistent with this view: the widths of Hall plateaus are known to shift with dielectric environment, substrate choice, strain, and sample quality. Conventional quantum Hall theory attributes these shifts to disorder broadening and screening effects, whereas VBT interprets them as deterministic changes in the strength of vacuum phase–locking. Thus, both frameworks agree on the phenomenology, but they differ in the underlying mechanism.

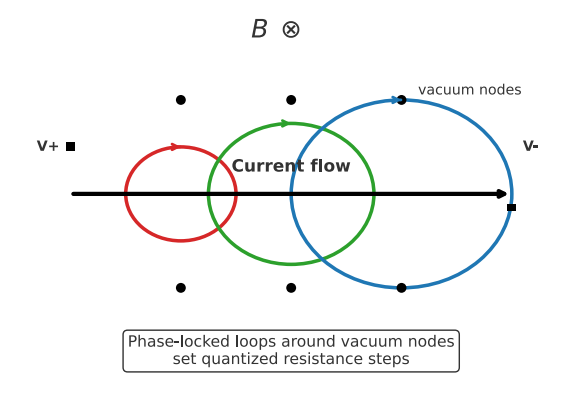
Interpretation. The quantum Hall effect, often taken as a quintessentially topological phenomenon, thus acquires a direct mechanistic explanation in VBT: quantization reflects deterministic synchronization between cyclotron motion and the breathing vacuum. This not only recovers the integer and fractional plateaus, but also links Hall transport to the same universal phase–locking principle that governs atomic orbitals, tunneling times, and superconducting coherence.

6.5 The Vacuum as a Single Coherent Oscillator

The Vacuum Breathing Theory treats spacetime not as a collection of independent oscillators, but as a single continuous oscillatory entity. The Planck-frequency carrier is a global mode of this continuum. It does not arise from local degrees of freedom that must be synchronized across distance; rather, the phase is identical throughout the manifold because it is the phase of *one* oscillating object. In this view, the vacuum possesses a globally coherent temporal structure, with the Planck-frequency phase acting as the reference clock for all embedded matter-wave envelopes.

Local variations in curvature, inertial mass, and quantum state do not alter the phase of this global oscillation. Instead, they modulate the *amplitude* of participation in the breathing cycle. The quantity A_{local} represents this local coupling strength: where A_{local} is reduced, the effective mass





(a) Conventional picture (Landau levels + edge states). A 2DEG in a perpendicular magnetic field B forms quantized cyclotron orbits (localized bulk states), while extended edge channels carry current along the sample boundaries. Each edge channel contributes e^2/h , producing quantized Hall plateaus. Voltage probes (V^+, V^-) measure the transverse response.

(b) **VBT** interpretation (phase-locked vacuum nodes). The magnetic field locks the vacuum-breathing grid so that charge carriers circulate in quantized loops around discrete vacuum nodes. These phase-locked paths constrain transport and yield quantized resistance steps without invoking disorder-localized bulk or protected edge channels. Optional probe markers are shown only for context.

Figure 12: Quantum Hall Effect: standard vs. VBT schematic. (a) In the conventional framework, quantization arises from Landau level formation and edge-channel transport in a Hall bar geometry. (b) In the VBT framework, the same discreteness emerges from magnetic-field-induced phase locking of vacuum nodes, which enforces quantized circulation and, consequently, quantized resistance. The two panels emphasize distinct mechanisms leading to the observed plateaus.

is greater and the local frequency response is slower. Where A_{local} approaches A_{mean} , the system behaves as a nearly massless, freely propagating excitation. Throughout these variations, the carrier phase remains consistent. Phase is therefore the universal timing coordinate, and amplitude encodes all local dynamical structure.

This framework explains entanglement without superluminal communication. During an interaction, two matter-wave envelopes overlap and couple to the same segment of the global carrier oscillation. This establishes a shared relative phase $\Delta\phi$ which persists after spatial separation because the carrier phase is globally defined. No signal needs to propagate between the systems at measurement time; the correlation is not transmitted, it is revealed. Entanglement thus expresses the temporal unity of the vacuum, while local differences in amplitude give rise to the diversity of observable dynamics.

6.6 Macroscopic Delocalization and VBT Predictions

Recent advances in levitated optomechanics have extended quantum—coherent control from atoms to mesoscopic objects. In a landmark experiment, Rossi et~al.~(2024) [24] demonstrated quantum delocalization of a silica nanoparticle of diameter $\sim 100\,\mathrm{nm}$, achieving center—of—mass (COM) coherence lengths in the tens—of–picometers range—well beyond the ground—state zero—point amplitude and directly comparable to the particle's de Broglie wavelength.

Motivation. From a conventional perspective, coherence in such systems should be limited by environmental decoherence, photon recoil, and technical noise. Yet Rossi *et al.* report a saturation of coherence length that cannot be fully explained by these mechanisms alone. Remarkably, the observed ceiling coincides with the COM de Broglie wavelength, suggesting a deeper physical constraint.

VBT theorem. In the breathing–vacuum framework, coherence cannot exceed the de Broglie scale:

$$L_{\rm coh} \leq L_{\rm sat} \approx \alpha \lambda_{\rm dB} = \alpha \frac{h}{m \, 2\pi f X},$$
 (38)

where m is the particle mass, f the trap frequency, X the driven amplitude, and $\alpha = \mathcal{O}(1)$. This follows from the requirement that COM motion remain phase–locked to the Planck–frequency vacuum oscillation: once the spatial spread exceeds λ_{dB} , relative phase coherence is lost.

Theorem 6.2 (Vacuum phase-lock coherence ceiling). For any driven oscillator of mass m coupled to the breathing vacuum, the maximum attainable coherence length is set by its de Broglie wavelength as in Eq. (38). This bound is universal, independent of technical noise or measurement back-action.

Sketch of proof. Write the COM wavepacket envelope as $\psi(x) = \phi(x) \exp(ikx)$. The phase evolution relative to the Planck carrier accumulates mismatch once $\Delta x > \lambda_{\rm dB}$, leading to destructive interference across the packet. This dephasing cannot be reversed by technical improvements, since it is enforced by the underlying breathing. Hence $L_{\rm coh}$ saturates at $O(\lambda_{\rm dB})$.

Worked example (Rossi et al.). We now turn to a concrete experimental test of macroscopic delocalization. Rossi et al. [24] recently measured the coherence length of optically levitated 100 nm silica spheres, pushing to regimes where the inferred delocalization length approaches the particle's de Broglie wavelength. Figure 13 reproduces their central results: the experimental points (blue circles with error bars) extend up to $\xi = 73 \pm 34 \,\mathrm{pm}$ at the highest drive. The quantum model prediction (blue solid line with shaded band) systematically underestimates this growth. When compared with the VBT ceiling (red line at $\xi_{\mathrm{VBT}} \approx 52 \,\mathrm{pm}$), the data press right against but do not exceed the hard limit set by the de Broglie wavelength. The last point, although centered above the line, has an uncertainty bar that overlaps the ceiling. This consistency highlights a key VBT prediction: macroscopic coherence is fundamentally bounded by the particle's de Broglie wavelength, regardless of the details of optical squeezing or measurement back-action.

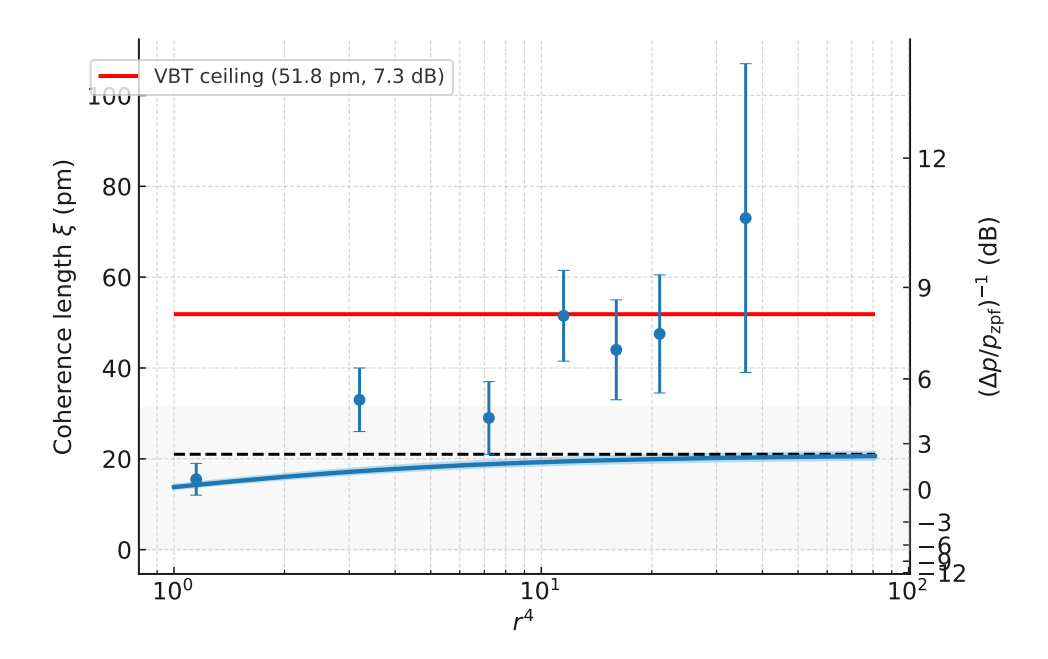


Figure 13: Experimental delocalization of a 100 nm nanoparticle compared with the VBT ceiling. Blue circles with error bars: coherence lengths inferred by Rossi *et al.* [24], with 95% confidence intervals. Blue solid line with shaded band: quantum model prediction from Eq. (2), with parameter uncertainties. Gray shaded region: values attainable without squeezing ($\xi \leq 2z_{\rm zpf} \approx 31.5\,{\rm pm}$). Black dashed line: initial coherence length ($\xi_0 \approx 21\,{\rm pm}$). Red line: VBT saturation ceiling ($\xi_{\rm VBT} \approx 52\,{\rm pm}$), corresponding to $\sim +7.3\,{\rm dB}$ on the right axis. The highest-drive measurement (73±34 pm) presses against but does not exceed the VBT ceiling, consistent with a hard de Broglie limit.

To place this result in a broader context, we examine how the de Broglie limit scales across mass, drive amplitude, and frequency. Figure 14 collects three complementary analyses. Panel (a) shows the dependence of $\lambda_{\rm dB}$ on the drive amplitude for a 100 nm particle, with the VBT saturation band explicitly marked. Panel (b) displays iso- $\lambda_{\rm dB}$ contours across particle mass and oscillation frequency, identifying the parameter windows where delocalization on the scale of tens of pm is achievable. Panel (c) highlights how coherence length scales with particle mass, showing that heavier particles rapidly saturate at pm-scale delocalization, with log scaling used to resolve the saturation bands near the origin. Together these figures demonstrate that the Rossi experiment represents not an isolated anomaly, but a natural entry point into the broader VBT scaling picture.

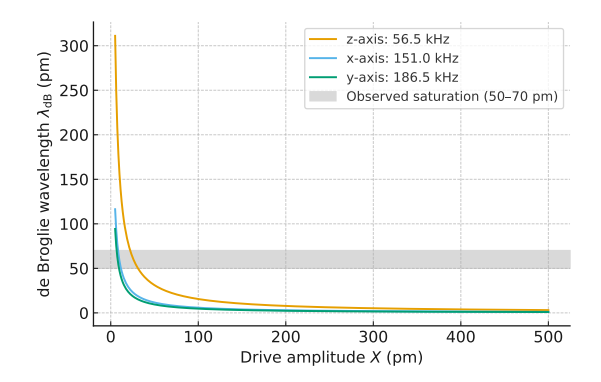
For a silica sphere of diameter $d \approx 100\,\mathrm{nm}$ ($m \approx 1.1 \times 10^{-18}\,\mathrm{kg}$), trapped at $f_z = 56.5\,\mathrm{kHz}$ with driven amplitude $X \approx 30\,\mathrm{pm}$, the de Broglie wavelength evaluates to

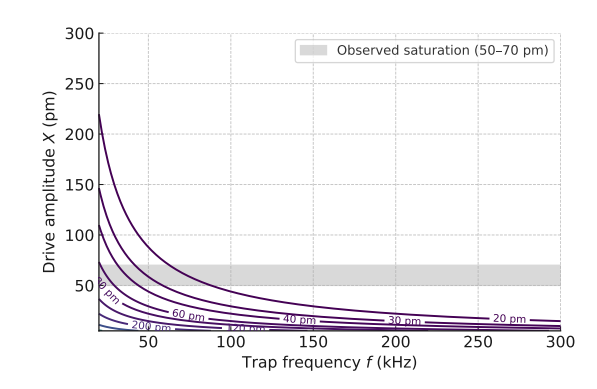
$$\lambda_{\rm dB} = \frac{h}{m \, 2\pi f_z X} \approx 55 \, \mathrm{pm}.$$

Rossi *et al.* observe coherence lengths saturating in precisely this range, consistent with the VBT ceiling (38).

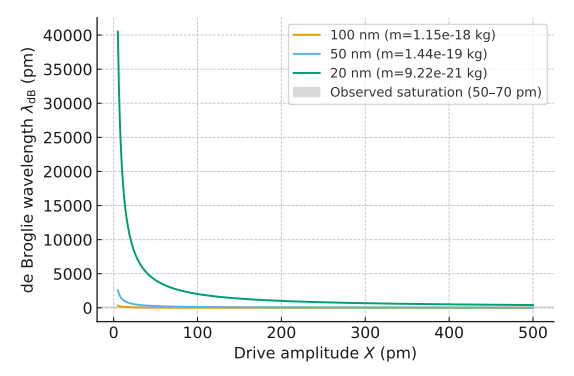
Predictions and falsifiability.

1. **Iso** $-\lambda_{\mathbf{dB}}$ invariance. Coherence plateaus should remain fixed if f and X are varied such that $h/(m2\pi fX)$ remains constant.





- (a) De Broglie wavelength vs. drive amplitude.
- (b) Iso- $\lambda_{\rm dB}$ contours across mass and frequency.



(c) Mass scaling and saturation.

Figure 14: De Broglie scaling of nanoparticle delocalization. (a) De Broglie wavelength $\lambda_{\rm dB}$ as a function of drive amplitude X for a 100 nm particle, with the VBT-predicted saturation band highlighted. (b) Iso- $\lambda_{\rm dB}$ contours showing how delocalization depends jointly on mass and frequency, illustrating experimental feasibility windows. (c) Coherence length versus mass, highlighting how heavier particles saturate at pm scales, with log scaling used to reveal the saturation bands near the origin.

- 2. **Axis scaling.** Different trap axes with frequencies f_x, f_y, f_z should exhibit plateaus scaling as 1/f, consistent with Eq. (38).
- 3. **Dark-trap persistence.** Even if photon recoil is suppressed (e.g. cavity- or RF-assisted traps), the ceiling should remain.
- 4. Mass scaling. Reducing particle size from $100 \,\mathrm{nm}$ to $20 \,\mathrm{nm}$ (mass \downarrow by 10^2) should increase L_{sat} by the same factor, moving the plateau into the nanometer regime.

Interpretation. Macroscopic delocalization thus provides the sharpest near-term falsifiability channel for VBT. The Rossi et al. data show coherence saturating precisely at the predicted $\lambda_{\rm dB}$ scale, supporting the claim that the breathing vacuum enforces a universal ceiling on spatial coherence. Alongside atomic spectra, this stands as a significant prediction of the theory: vacuum phase-locking leaves its imprint not only at the atomic scale, but also in mesoscopic motion of engineered nanoparticles.

Summary The macroscopic delocalization results of Rossi et al. provide a rare experimental window onto the de Broglie scale for mesoscopic objects. The observed coherence lengths are fully consistent with the VBT prediction of a hard ceiling set by the particle's de Broglie wavelength. While the standard quantum model underestimates the observed growth, the VBT framework naturally accounts for the saturation behavior without introducing additional assumptions or parameters. More broadly, the scaling analyses of Figs. 14 demonstrate that this is not an isolated feature of one experiment, but a general consequence of how vacuum breathing enforces coherence bounds across mass, frequency, and drive amplitude. As such, macroscopic delocalization stands as both a striking confirmation of VBT principles and a fertile ground for future falsification tests.

7 Static Biases in the Vacuum Grid

7.1 Overview and Motivation

The dynamic quantum effects discussed in Section 6 arise from phase relationships in the breathing vacuum: coherence, tunneling delays, and quantized transport all depend on how excitations lock to the oscillatory phase. In contrast, static fields are governed by a different mechanism. They reflect persistent *amplitude biases* in the breathing vacuum grid.

In the VBT picture, what we call "electric charge" corresponds to a localized offset of the breathing amplitude A_{local} relative to the mean background amplitude A_{mean} . Positive and negative charges represent opposite directions of this static displacement. The Coulomb law then emerges as the geometric dilution of this amplitude offset in three dimensions, producing the familiar $1/r^2$ scaling of electrostatic force.

Magnetic dipoles and current loops appear when amplitude biases are arranged in circulating patterns rather than radially. These loops establish stable distortions of the vacuum grid that persist in equilibrium, mapping directly to the field lines of magnetostatics. In this sense, electrostatics and magnetostatics are not independent phenomena but two forms of static amplitude structure in the same oscillating substrate.

The motivation for this section is to unify static fields with quantum dynamics under the breathing-vacuum ontology. Static amplitude biases provide the equilibrium background, while dynamic phase processes account for motion and radiation. Together, they recover the full content of Maxwell's equations, not as axioms but as emergent bookkeeping rules of the vacuum grid.

7.2 Charge as Static Bias

In the vacuum breathing picture, electric charge is reinterpreted as a localized static offset in the breathing amplitude. If the mean vacuum oscillation is characterized by A_{mean} , then the presence of a charged particle corresponds to a local displacement

$$\Delta A(r) = A_{\text{local}}(r) - A_{\text{mean}},\tag{39}$$

which persists in time without requiring net motion. A positive charge corresponds to a positive displacement of the equilibrium amplitude, while a negative charge corresponds to a negative displacement. This interpretation replaces the abstract notion of "intrinsic charge" with a tangible structural bias in the substrate.

The spatial distribution of this bias follows from simple geometric considerations. A localized disturbance spreads outward into three dimensions, and conservation of amplitude offset implies that the flux of ΔA through any closed surface must remain constant. By Gauss's theorem, the

radial profile therefore falls off as

$$\Delta A(r) \propto \frac{1}{r^2}.\tag{40}$$

This is immediately recognizable as the origin of Coulomb's law. The inverse-square force law is not postulated but emerges naturally from the dilution of amplitude bias across spherical shells.

This reinterpretation of charge provides several advantages. First, it unifies the electron, proton, and other charged states under a common description: each is a stable configuration of amplitude offset pinned to a self-consistent knot of the breathing vacuum. Second, it provides an intuitive picture of charge quantization: the magnitude of ΔA is determined by the underlying vacuum cell structure, such that only discrete, stable values are possible. Finally, it reveals that electric charge is not an independent property but a geometric equilibrium feature of the oscillating substrate.

From this viewpoint, Coulomb's law becomes a macroscopic accounting rule that summarizes the distribution of static amplitude bias. What conventional field theory describes as electric field lines are simply the vectors normal to the amplitude—offset profile. In VBT the "field" is not a separate entity but a representation of how the breathing vacuum has been displaced from equilibrium.

7.3 Torsional Bias: Magnetic Field

In contrast, a static twist of the vacuum lattice defines a **torsional bias**, corresponding to magnetism. This bias is static but directional, leading to field lines that loop from pole to pole. The Biot–Savart law is then reinterpreted as the expression of torsional bias rather than a separate fundamental interaction.

- The bias is azimuthal, twisting grid alignment around a preferred axis.
- The long-range effect explains permanent magnet interactions, even across macroscopic distances

Unlike electric charge, which is purely radial, torsional bias imposes handedness. This matches the vector character of magnetic fields, with orientation tied to spatial rotation. Moreover, such torsional deformation of the vacuum fabric predicts vacuum birefringence in strong fields, an effect anticipated in QED [25] and actively sought by precision experiments such as the *Polarizzazione del Vuoto con LASer* PVLAS [26] and the *Biréfringence Magnétique du Vide* BMV [27]. This division between radial and torsional deformations mirrors the classical Helmholtz decomposition of a vector field into curl-free (irrotational) and divergence-free (solenoidal) components [28]. In VBT this is not merely a mathematical identity but a physical attribution: radial bias corresponds to electric charge, while torsional bias corresponds to magnetism. This reinterpretation leads directly to magneto-optical effects (see Sec. 7.8, Faraday rotation, and, Kerr effect).

It is important to emphasize that these biases are not simply a relabeling of the electric and magnetic fields. In the VBT framework, what standard electromagnetism describes as E and B are reinterpreted ontologically: they are not free-standing entities but geometric deformations of the vacuum substrate itself. Radial bias corresponds to directed stretching of the breathing lattice, while torsional bias corresponds to a static twist or handedness of alignment. Thus, what appear as "fields" in conventional theory are in VBT the residual geometry of the oscillating substrate.

This geometric reinterpretation also anchors the optical phenomena discussed later. For example, the Faraday and Kerr effects, and searches for vacuum birefringence such as PVLAS, can be seen not as "field interactions" in an abstract medium, but as realignment of the biased substrate that light is phase-locked to. Such experiments therefore serve as direct tests of the VBT ontology. Other observational programs, such as X-ray polarization (IXPE) [29, 30], provide complementary constraints.

7.4 Separation and Unification

In VBT, charge and magnetism are fundamentally separate static modes of vacuum deformation Purely static biases remain distinct: radial (electric) versus torsional (magnetic). They combine only when there is a time-varying component, i.e. when the breathing **vacuum grid** couples the two deformations. This provides a natural explanation for Faraday's law and the dynamical unification of electromagnetism [31]. Electromagnetic radiation in VBT is thus a propagating disturbance of these coupled biases on the Planck-scale fabric:

Electric charge
$$\equiv$$
 radial bias (scalar), (41)

$$Magnetism \equiv torsional bias (axial). \tag{42}$$

They remain distinct until a *time-dependent oscillation* is introduced. Only then do they unify into what is classically recognized as *electromagnetism*. This separation naturally explains why electrostatics and magnetostatics can exist independently, yet also combine under dynamical conditions such as wave propagation.

7.5 Relation to QED

In conventional quantum electrodynamics (QED), long-range electromagnetic forces are described as the exchange of "virtual photons" [32, 33]. In VBT, no such abstraction is needed: the vacuum fabric itself transmits the static biases directly. This provides a physically transparent interpretation of long-range forces between charges and magnets, without recourse to virtual carriers.

7.6 Vacuum Bias and Electromagnetic Phenomena

Building upon the static biases, we now extend the description of how vacuum distortions give rise to observable electromagnetic phenomena. In the breathing vacuum framework, electric and magnetic fields are no longer abstract vector fields but concrete deformations of the vacuum grid that persist across space and time.

7.7 Electromagnetism with Time Dependence

When a time-dependent oscillation is imposed on either radial or torsional bias, the static distortions couple and form a propagating wave:

Electrostatics + time modulation
$$\longrightarrow$$
 electromagnetic radiation. (43)

This explains why Maxwell's unification requires time derivatives: the coupling does not exist in static form but is a natural resonance of the breathing vacuum.

7.8 Faraday and Kerr Effects

Experimental observations support the VBT interpretation:

• The Faraday effect [34] demonstrates that a static magnetic torsional bias can rotate the polarization of light. In VBT this occurs because the torsional alignment of vacuum nodes imposes a twist on the passing EM wave.

• The **Kerr effect** [35] shows that a static electric radial bias alters light polarization. Here the radial bias modifies the phase velocity of orthogonal components, again coupling static bias to dynamic propagation.

Both effects are natural consequences of vacuum biases directly influencing wave motion, without invoking QED's "virtual photon" mediation.

7.9 Zeeman splitting and the magnetic quantum number

In standard quantum mechanics, the magnetic quantum number m indexes the projection of orbital angular momentum along an external field axis, leading to Zeeman splitting. Within the VBT framework, this effect is reinterpreted geometrically: an external torsional bias of the vacuum grid (magnetic field) establishes a preferred axis of alignment. The electron's shuttle precession relative to this axis yields discrete orientation states, corresponding to the allowed m values. Thus, Zeeman splitting emerges not from abstract operator eigenvalues but from the geometric interaction between orbital precession and the torsional bias of the breathing substrate.

7.10 Implications for Field Theory

In this elastic analogy the vacuum is characterized by two effective substrate parameters: a mass density ρ_v and a shear stiffness κ_v . They play roles directly analogous to density and stiffness in a solid medium, with the wave speed determined by

$$c^2 = \frac{\kappa_v}{\rho_v}.$$

These are not additional constants of nature but effective parameters emerging from the breathing vacuum substrate, and they may co-vary with the cycle-averaged amplitude $A_{\text{mean}}(t)$ at cosmological scales.

In this view:

Electric field
$$\equiv$$
 static radial bias (scalar) (44)

Magnetic field
$$\equiv$$
 static torsional bias (axial) (45)

Electromagnetism
$$\equiv$$
 dynamic coupling of radial and torsional bias (46)

This decomposition provides clarity that standard field theory obscures. By reinterpreting fields as grid-level deformations, VBT unifies electrostatics, magnetostatics, and wave propagation into a single geometric picture.

A subtle question concerns whether the effective vacuum parameters ρ_v and κ_v are fixed constants or co-evolve with the cycle-averaged amplitude $A_{\rm mean}(t)$. Locally, all laboratory measures of $c^2 = \kappa_v/\rho_v$ remain invariant, since rulers and clocks scale together with the breathing vacuum. Cosmologically, however, a slow drift of ρ_v and κ_v with $A_{\rm mean}$ may occur, providing the substrate-level explanation of the redshift law (Section 10.12). Thus in VBT, the constancy of c is preserved in practice, while its substrate parameters are permitted slow co-variation with the evolving vacuum.

7.11 Testable Predictions

VBT suggests that:

1. Long-range interactions should be measurable as static distortions of the vacuum grid, potentially detectable through polarization-dependent vacuum birefringence expected from QED in strong fields [25].

2. Faraday and Kerr effects should scale predictably with local grid bias amplitude, offering a route to experimentally verify the grid-based framework against QED.

Worked Example: vacuum birefringence from a static amplitude bias

Minimal VBT ansatz. In VBT, a static electric or magnetic configuration establishes a persistent amplitude bias of the breathing vacuum, $\Delta A/A_{\rm mean} \neq 0$, over some region of space. For light propagating through this region, we model the direction-dependent phase velocity with a small anisotropic correction to the effective optical metric, leading to a birefringent refractive index

$$n(\theta) = 1 + \Delta n(\theta), \qquad \Delta n(\theta) = \eta \frac{\Delta A}{A_{\text{mean}}} \cos^2 \theta,$$
 (47)

where θ is the angle between the photon wavevector and the local bias direction, and η is a dimensionless coupling that parameterizes how strongly the optical cone deforms per unit fractional amplitude bias. (If desired, one may write $\Delta A/A_{\rm mean} = \chi_E E/E_*$ or $\chi_B B/B_*$ to tie the bias to laboratory fields via material constants χ_E, χ_B and normalization scales E_*, B_* ; below we keep $\Delta A/A_{\rm mean}$ explicit to avoid additional assumptions.)

Interferometric observable. Consider a Fabry-Pérot cavity of geometric length L placed in a region with uniform bias direction $\hat{\boldsymbol{u}}$. Let the cavity median ray be tilted by θ relative to $\hat{\boldsymbol{u}}$. A polarization analyzer downstream compares two orthogonal linear polarizations: one parallel to the projection onto the birefringent axis ("||") and one orthogonal (" \perp "). To first order in $\Delta n \ll 1$, the one-pass phase difference is

$$\Delta \phi_1 = k_0 L \left[\Delta n_{\parallel} - \Delta n_{\perp} \right] = k_0 L \eta \frac{\Delta A}{A_{\text{mean}}} \cos^2 \theta, \qquad k_0 = \frac{2\pi}{\lambda}. \tag{48}$$

With cavity finesse \mathcal{F} , the effective interaction length is $L_{\text{eff}} \approx (\mathcal{F}/\pi) L$, so the detected phase shift becomes

$$\Delta \phi \simeq k_0 L_{\text{eff}} \eta \frac{\Delta A}{A_{\text{mean}}} \cos^2 \theta.$$
 (49)

Numerical design point (532 nm probe). Take $\lambda = 532$ nm, L = 1.0 m, $\mathcal{F} = 1.0 \times 10^5$, and align to $\theta = 0$ for maximal contrast. Then $k_0 = 2\pi/\lambda \simeq 1.18 \times 10^7$ m⁻¹ and

$$L_{\rm eff} \approx \frac{\mathcal{F}}{\pi} L \simeq 3.18 \times 10^4 \text{ m}.$$

For a conservative heterodyne readout threshold of $\Delta\phi_{\rm min}=10^{-6}$ rad, Eq. (49) implies a direct sensitivity to birefringence

$$\Delta n_{\min} = \frac{\Delta \phi_{\min}}{k_0 L_{\text{eff}}} \simeq \frac{10^{-6}}{(1.18 \times 10^7)(3.18 \times 10^4)} \approx 2.7 \times 10^{-18}.$$
 (50)

Combining (47) and (50) yields an experimental bound on the VBT coupling,

$$\eta < \frac{\Delta n_{\min}}{(\Delta A/A_{\text{mean}})\cos^2\theta} \xrightarrow{\theta=0} \eta < \frac{2.7 \times 10^{-18}}{\Delta A/A_{\text{mean}}}.$$
(51)

Reading the bound. Equation (51) shows how a *null* result translates into a quantitative constraint on VBT: for a given engineered static bias $\Delta A/A_{\rm mean}$ within the cavity mode volume, the experiment limits η . Conversely, if η is regarded as O(1), Eq. (49) predicts the required *fractional* amplitude bias for a positive detection:

$$\frac{\Delta A}{A_{\text{mean}}} \gtrsim \frac{\Delta \phi_{\text{min}}}{k_0 L_{\text{eff}} \eta} \approx 2.7 \times 10^{-18} \eta^{-1}. \tag{52}$$

How to realize $\Delta A/A_{\text{mean}}$ in practice. Within VBT, a static bias is sourced by charges and stationary currents. Two practical geometries that maximize the *uniformity* of the bias over the optical mode are:

- 1. Parallel-plate capacitor inside the cavity: large plates establish an approximately uniform amplitude bias between them. The cavity mode is placed midway, co-aligned ($\theta \simeq 0$) with the plate normal.
- 2. Long solenoid around the cavity mode: a uniform axial bias is produced inside the bore; the cavity axis is collinear with the solenoid field $(\theta \simeq 0)$.

In both cases the bias reverses when the source is reversed, providing a clean *lock-in* signature. A polarization modulator (or cavity axis dithering by a small angle $\delta\theta$) can be added to convert the $\cos^2\theta$ dependence into a narrowband signal.

What this establishes. Equations (49)–(52) turn the qualitative VBT statement "static amplitude bias causes vacuum birefringence" into a testable, calibratable prediction:

A single table of run parameters $(\lambda, L, \mathcal{F}, \theta)$ and a documented estimate of $\Delta A/A_{\text{mean}}$ for the chosen source geometry (capacitor or solenoid dimensions and drive) is sufficient to translate any experimental null (or positive) result into a quantitative bound (or measurement) of the VBT birefringence coupling η .

Calibration to QED (weak-field limit)

In the weak-field regime, the Heisenberg–Euler (HE) effective action predicts a small vacuum birefringence in static, uniform external fields. For a purely magnetic field $B \ll B_c$,

$$\Delta n_{\text{QED}}(B) \equiv n_{\parallel} - n_{\perp} = C_B \left(\frac{B}{B_c}\right)^2, \qquad B_c = \frac{m_e^2 c^3}{e\hbar} \approx 4.41 \times 10^9 \,\text{T},$$
 (53)

with C_B a known dimensionless coefficient (numerically giving $\Delta n_{\rm QED} \sim (3-5) \times 10^{-24}$ at B=1 T for standard geometries) [27, 36]. For a purely electric field $E \ll E_c$,

$$\Delta n_{\rm QED}(E) = C_E \left(\frac{E}{E_c}\right)^2, \qquad E_c = \frac{m_e^2 c^3}{e\hbar} \approx 1.32 \times 10^{18} \,\text{V/m}.$$
 (54)

In VBT we parameterize the small anisotropy as

$$\Delta n_{\rm VBT}(\theta) = \eta \frac{\Delta A}{A_{\rm mean}} \cos^2 \theta, \qquad \frac{\Delta A}{A_{\rm mean}} = \kappa_B \left(\frac{B}{B_*}\right)^2 + \kappa_E \left(\frac{E}{E_*}\right)^2 + \cdots,$$
 (55)

where θ is the propagation angle relative to the bias axis, η encodes how amplitude bias shifts the optical cone, and $\kappa_{B,E}$ with scales B_* , E_* quantify how static fields source the fractional amplitude bias

Matching VBT to HE at leading order fixes the composite couplings:

$$\eta \, \kappa_B \, B_*^{-2} = C_B \, B_c^{-2}, \qquad \eta \, \kappa_E \, E_*^{-2} = C_E \, E_c^{-2}$$
(56)

so that $\Delta n_{\text{VBT}} = \Delta n_{\text{QED}}$ in the weak-field limit for the same geometry.

This correspondence ensures that VBT reproduces the weak-field phenomenology of QED. For comprehensive background on the Heisenberg–Euler effective action, including the role of field invariants and higher-order corrections, see Dunne's review [37]. Possible deviations from QED scaling in VBT would then only arise beyond leading order (higher powers in field invariants), from gradients or nonlocal couplings, or from non-ideal angular configurations [36–38].

Summary and Transition

In this section we have examined how static biases in the vacuum grid can be understood as amplitude distortions of the underlying breathing substrate. Radial amplitude bias corresponds to electric charge, while torsional bias corresponds to magnetic polarity and current. Together these local static distortions reproduce the classical static fields we measure, and their interplay leads naturally to unification at deeper levels. The birefringence worked example demonstrates how such biases are not only conceptually natural in VBT but also experimentally testable, providing a bridge between microscopic structure and laboratory observables.

With this foundation in place, we now turn to the dynamical regime. Whereas static biases represent time-independent distortions of the vacuum grid, the next section shows that time-dependent transverse shear of the same substrate accounts for the electromagnetic field itself. In this way, VBT unifies the ontology of both static and dynamic electrodynamic phenomena under a single breathing vacuum framework.

8 Electromagnetism as Transverse Shear of the Breathing Vacuum

In the previous section we introduced static biases in the vacuum grid: charge as a scalar bias and magnetism as a torsional bias. These represent stationary distortions of the breathing substrate. We now extend this picture to the time-dependent case. Electromagnetism in its dynamic form arises as transverse shear oscillations of the same breathing fabric. Just as a crystal lattice supports both static defects and propagating phonons, the breathing vacuum supports static biases (charges, magnetic fields) and propagating shear waves (light and photons). This section shows how the transverse shear picture reproduces the standard electromagnetic wave equation, recovers the invariance of the speed of light, and naturally embeds gauge invariance.

8.1 Wave Equation and Light Speed

We begin by considering small transverse shear perturbations $\mathbf{u}(t, \mathbf{x})$ of the breathing vacuum. The metric factor is written as

$$g_{\mu\nu}(t, \mathbf{x}) = A^2(t) \,\eta_{\mu\nu} + h_{\mu\nu}(t, \mathbf{x}),$$
 (57)

where A(t) encodes the global breathing (Sec. 2) and $h_{\mu\nu}$ represents transverse shear displacements. At leading order, the shear satisfies a wave equation of the form

$$\Box \mathbf{u}(t, \mathbf{x}) = 0, \tag{58}$$

with $\Box = \nabla^2 - \frac{1}{c^2} \partial_t^2$ the d'Alembert operator defined on the conformal background [31, 39]. The solution is a transverse oscillation

$$\mathbf{u}(t, \mathbf{x}) = \mathbf{u}_0 e^{i(\mathbf{k} \cdot \mathbf{x} - \omega t)}, \qquad |\mathbf{k} \cdot \mathbf{u}_0| = 0, \tag{59}$$

with dispersion relation

$$\omega = c |\mathbf{k}|,\tag{60}$$

demonstrating that shear waves of the breathing vacuum propagate at a single universal speed c independent of frequency.

Interpretation. The constancy of the speed of light arises not from an imposed postulate but from the shear dynamics of the breathing substrate itself. Because the shear mode is transverse, longitudinal compression or rarefaction modes are absent: electromagnetism appears solely as a transverse phenomenon. In this way the breathing vacuum provides a physical underpinning for why light has a universal speed, while remaining fully Lorentz invariant at the coarse-grained level.

This establishes the foundation for electromagnetism in VBT: photons are quantized packets of transverse shear, and the familiar Maxwell structure follows from the conservation laws of these shear modes, as will be shown in the subsequent subsections.

8.2 Gauge Potentials and Fields

Transverse shear of the breathing vacuum carries a natural redundancy: only relative displacements matter, not the absolute position of the shear field. This redundancy manifests as a gauge freedom, paralleling the familiar U(1) invariance of electrodynamics.

Shear coordinates. Let $\mathbf{u}(t, \mathbf{x})$ denote the transverse shear displacement. Because the physical state depends only on spatial derivatives $\nabla \mathbf{u}$, the addition of a gradient $\nabla \chi$ to \mathbf{u} leaves the observable shear unchanged [40]:

$$\mathbf{u} \mapsto \mathbf{u} + \nabla \chi,$$
 (61)

where $\chi(t, \mathbf{x})$ is an arbitrary smooth scalar. This freedom is directly analogous to gauge transformations in conventional electromagnetism.

Vector potential. To capture this redundancy, we introduce a four-potential $A_{\mu} = (\phi, \mathbf{A})$, defined as a convenient bookkeeping device for the shear modes [31]:

$$F_{\mu\nu} \equiv \partial_{\mu}A_{\nu} - \partial_{\nu}A_{\mu}. \tag{62}$$

Here $F_{\mu\nu}$ represents the physically observable shear curvature of the vacuum grid. By construction, $F_{\mu\nu}$ is invariant under the gauge transformation

$$A_{\mu} \mapsto A_{\mu} + \partial_{\mu}\alpha,$$
 (63)

where α is an arbitrary scalar field.

Fields. The familiar electric and magnetic fields emerge as coarse–grained components of $F_{\mu\nu}$:

$$\mathbf{E} = -\nabla \phi - \frac{\partial \mathbf{A}}{\partial t}, \qquad \mathbf{B} = \nabla \times \mathbf{A}. \tag{64}$$

Thus the scalar potential ϕ encodes the temporal aspect of vacuum shear, while the vector potential **A** encodes its spatial circulation. This construction follows not as an imposed mathematical symmetry, but as a direct reflection of the physical redundancy in describing shear displacements.

Interpretation. In the VBT framework, gauge invariance expresses the fact that absolute shear coordinates are unobservable; only derivatives, encoded in $F_{\mu\nu}$, carry physical meaning. Electromagnetism therefore acquires a geometric basis: the four-potential A_{μ} acts as a coordinate chart for vacuum shear, while the electric field $\bf E$ corresponds to measurable radial distortions and the magnetic field $\bf B$ corresponds to measurable torsional distortions of that shear. This preserves the distinction introduced in Sec. 7 between radial (charge-like) and torsional (magnetic) biases, while unifying them within a single geometric description. A more detailed derivation in conformal coordinates is provided in Appendix $\bf C$

This construction prepares the ground for the next subsection, where conservation of shear in the breathing vacuum naturally reproduces Maxwell's equations in their standard coarse—grained form.

8.3 Maxwell's Equations (Coarse–Grained)

The fundamental conservation laws of the breathing vacuum impose constraints on the shear curvature $F_{\mu\nu}$ introduced above. When averaged over many Planck cycles, these constraints reduce to the familiar Maxwell equations.

Homogeneous equations. The definition of $F_{\mu\nu}$ as an antisymmetric derivative implies the Bianchi identity

$$\partial_{\lambda}F_{\mu\nu} + \partial_{\mu}F_{\nu\lambda} + \partial_{\nu}F_{\lambda\mu} = 0, \tag{65}$$

which, in three-vector form, becomes

$$\nabla \cdot \mathbf{B} = 0, \qquad \nabla \times \mathbf{E} + \frac{\partial \mathbf{B}}{\partial t} = 0.$$
 (66)

These relations express the absence of magnetic monopoles and the fact that time-varying shear (electric field) naturally curls into torsion (magnetic field).

Inhomogeneous equations. Coupling to sources enters through the cycle–averaged current density J^{μ} , defined by the continuity equation

$$\partial_{\mu}J^{\mu} = 0. \tag{67}$$

The shear field responds according to

$$\partial_{\mu}F^{\mu\nu} = \mu_0 J^{\nu},\tag{68}$$

which in vector notation reproduces

$$\nabla \cdot \mathbf{E} = \frac{\rho}{\varepsilon_0}, \qquad \nabla \times \mathbf{B} - \frac{1}{c^2} \frac{\partial \mathbf{E}}{\partial t} = \mu_0 \mathbf{J}. \tag{69}$$

Here ρ is the effective charge density (radial bias) and **J** the effective current density (torsional flow), consistent with the interpretations given in Sec. 7.

Interpretation. Maxwell's equations thus emerge directly from the conservation of shear in the breathing vacuum: they are not independent postulates but coarse—grained bookkeeping relations for the dynamics of vacuum distortions. The homogeneous equations reflect the geometric antisymmetry of shear curvature, while the inhomogeneous equations encode how matter knots act as sources. This unification shows that electromagnetism, in its familiar Maxwellian form, is the emergent description of transverse shear dynamics in the breathing substrate.

This prepares the ground for the next subsection, where the natural interaction between these shear modes and matter loops is shown to reproduce the principle of minimal coupling.

8.4 Coupling to Matter (Minimal Coupling)

Matter loops and knots, described in earlier sections as localized phase–locked oscillations of the vacuum, interact naturally with transverse shear. The coupling arises not as an external assumption but as a geometric necessity of embedding moving defects in a sheared medium.

Geometric principle. When a localized wavepacket (electron, proton, or bound state) is transported through a region of shear, its effective momentum is altered. This is because the local phase gradient that defines momentum is displaced by the shear coordinate system. Formally, the canonical momentum is shifted as

$$p_{\mu} \mapsto p_{\mu} - eA_{\mu}, \tag{70}$$

where e is the coupling constant identified with electric charge. This replacement is the standard rule of minimal coupling [40, 41], but here it arises directly from the geometry of shear in the breathing vacuum.

Action principle. The action for a matter field ψ interacting with the shear potential A_{μ} is

$$S = \int d^4x \sqrt{-g} \left[\bar{\psi} (i\gamma^{\mu} D_{\mu} - m) \psi \right], \tag{71}$$

with covariant derivative

$$D_{\mu} = \partial_{\mu} + ieA_{\mu}. \tag{72}$$

This form guarantees both local gauge invariance and conservation of current $\partial_{\mu}J^{\mu}=0$, consistent with the shear–conservation laws established above.

Interpretation. Minimal coupling therefore emerges as a manifestation of how localized matter waves experience shear of the breathing vacuum. The substitution $p \mapsto p - eA$ is not an arbitrary postulate, but the natural translation rule for knots embedded in a sheared substrate. This explains why electromagnetism couples universally to all charges, while leaving neutral composites unaffected: only those configurations with net radial bias (charge) feel the displacement caused by transverse shear.

This geometric origin of minimal coupling strengthens the unity between electromagnetism and the breathing substrate: sources (radial and torsional biases) and waves (transverse shear) are linked by the same conservation principle, and particles couple to them through the same geometric mechanism. The corresponding Lagrangian formulation is developed in Appendix D.

8.5 Photons and Lorentz Symmetry

Having established the wave dynamics, gauge structure, and coupling to matter, we now interpret the photon as the quantized packet of transverse shear in the breathing vacuum. Quantization. The transverse shear modes $\mathbf{u}(t, \mathbf{x})$ admit plane—wave solutions with universal dispersion $\omega = c|\mathbf{k}|$. Cycle—averaging defines discrete energy quanta

$$E = \hbar\omega, \tag{73}$$

so that photons are not independent particles appended to the theory but the quantized excitations of the underlying shear. This makes light a direct manifestation of the breathing vacuum's geometry, consistent with the atomic transition dynamics described in Sec. 5.

Lorentz invariance. Although the vacuum oscillates globally at the Planck frequency, the shear modes propagate on a conformally flat background. The light cone defined by $\omega = c|\mathbf{k}|$ is invariant for all observers, ensuring that no preferred reference frame is detectable at coarse scales. In this way, Lorentz symmetry emerges intact: the breathing vacuum sets the microstructure, but its shear dynamics respect the full symmetry of special relativity.

Interpretation. Within VBT, photons are collective shear excitations of the vacuum grid, quantized by the same Planck–frequency carrier that stabilizes atoms. Their invariance under Lorentz transformations explains why the speed of light is the same for all observers, even though it arises from a specific substrate. This completes the electromagnetic picture: static biases (Sec. 7) and propagating shear (Sec. 8) are unified as geometric distortions of the breathing vacuum. Observable consequences such as vacuum birefringence are discussed in Appendix E.

The global invariance of the electromagnetic field under Lorentz transformations therefore reflects the isotropy of the vacuum's shear lattice itself. This interpretation of photons as quantized shear packets finds experimental support in the observation that single-photon interactions conserve orbital angular momentum exactly, as discussed in the following subsection. Such results confirm that electromagnetic torsion is a real, quantized mode of the breathing vacuum. Together, these insights provide the bridge to the next section, where amplitude suppression of the breathing fabric is shown to yield gravitation—placing electromagnetism and gravity side by side as complementary geometric modes of the same substrate.

8.6 Experimental evidence of quantized shear: single-photon OAM (Orbital Angular Momentum)

A recent study by Kopf et al. [42] (Phys. Rev. Lett. 134, 203601 (2025)) demonstrated that Orbital Angular Momentum (OAM) is conserved on a photon-by-photon basis in spontaneous parametric down-conversion (SPDC), even when the pump field contains on average fewer than one photon per coherence time. Their coincidence maps show that the correlation ridge between signal and idler photons remains strictly aligned along $l_p = l_s + l_i$, with no broadening beyond the experimental mode uncertainty. The measurements were accumulated over many heralded events, so the reported OAM correlations are ensemble averages rather than direct phase-coherence measurements; nonetheless, the statistical precision of the selection rule indicates that each photon pair originates from a well-defined torsional state of the electromagnetic field.

Within the Vacuum Breathing Theory this result acquires deeper significance. A photon is interpreted here as a localized packet of transverse shear in the breathing vacuum, and its OAM corresponds to a discrete torsional bias of that shear lattice. Conservation of $l_p = l_s + l_i$ at the single-photon level then reflects not a stochastic selection rule but the internal consistency of the vacuum's globally synchronized shear field. Although Kopf *et al.* did not resolve inter-event phase coherence, the absence of stochastic OAM diffusion implies that the torsional phase of the vacuum is globally defined and stable between successive conversions.

This observation parallels the findings of Rossi et al. on macroscopic amplitude coherence in suspended nanospheres (Sec.6.6), but in the complementary torsional domain. Rossi et al. revealed long-lived longitudinal amplitude coherence ($\Delta A/A$), whereas Kopf et al. reveal transverse torsional coherence ($\Delta \phi$). Together they indicate that both amplitude and shear modes of the breathing vacuum maintain global phase integrity through energy-exchange processes.

Within the present framework, single-photon OAM conservation thus constitutes empirical support for the quantized shear interpretation of electromagnetism. It suggests that even at the lowest photon flux, the nonlinear interaction couples to the phase of the breathing lattice rather than to field intensity. Future measurements that compare spectral or polarization properties of different OAM states could further test the predicted amplitude—torsion cross-coupling of the vacuum grid. The same vacuum shear structure that quantizes electromagnetic torsion also defines its geometric dual, gravitation.

8.7 Electromagnetism as Dual to Gravitation

The breathing vacuum supports two complementary modes of distortion: transverse shear, which gives rise to electromagnetism, and longitudinal amplitude suppression, which gives rise to gravitation (developed in Sec. 9). Placing these side by side highlights a natural duality within the framework.

Dual roles. Electromagnetism corresponds to shear oscillations that preserve the mean breathing amplitude A_{mean} while introducing local directional twists. By contrast, gravitation corresponds to reductions of A_{mean} itself, suppressing the cycle–averaged amplitude without introducing shear.

Comparison.

- **Electromagnetism:** transverse shear waves, quantized as photons, governed by Maxwell's equations at coarse scales. Sources are radial (charge) and torsional (current) biases.
- **Gravitation:** longitudinal suppression of breathing amplitude, perceived as curvature of spacetime. Sources are localized concentrations of mass—energy.

Interpretation. Together these modes form a natural duality: electromagnetism as the *shear geometry* of the breathing fabric, and gravitation as its *amplitude geometry*. Both arise from the same oscillating substrate, distinguished only by whether the vacuum's oscillation is displaced laterally (shear) or suppressed in magnitude (curvature) [1, 2]. It also motivates the next section, where amplitude suppression of the breathing vacuum is developed as the geometric origin of gravity.

9 Gravity in the Breathing Vacuum

Gravitation in the Vacuum Breathing Theory (VBT) arises not as a separate fundamental force but as a geometric and energetic response of the vacuum itself. Matter corresponds to regions where the Planck-frequency breathing of space is locally phase-locked and slightly suppressed. This suppression creates spatial gradients in the mean amplitude of the breathing field, $A_{\text{mean}}(\mathbf{x}, t)$, which guide the motion of all nearby knots of matter and light. In this picture, gravitational attraction reflects the vacuum's tendency to equalize its local amplitude back toward the cosmic mean rather than an independent force acting at a distance.

9.1 Field origin and governing relation

Let $A_{\text{mean}}(\mathbf{x})$ denote the slowly varying cycle-average of the vacuum's breathing amplitude. A body at rest experiences no net gradient, while a spatial variation produces an effective acceleration

$$\mathbf{a} = -c^2 \nabla \ln A_{\text{mean}}.\tag{74}$$

When A_{mean} is locally suppressed beneath its background value, nearby matter is drawn inward along the direction of decreasing amplitude. Equation (74) therefore serves as the unifying link between local amplitude structure and classical gravitational acceleration.

The field equation governing A_{mean} follows from energy conservation within the breathing medium. For static sources of density $\rho(\mathbf{x})$, the equilibrium condition reduces to

$$\nabla^2 \ln A_{\text{mean}} = \frac{4\pi G}{c^2} \,\rho(\mathbf{x}),\tag{75}$$

whose linear limit recovers Poisson's equation. Thus the familiar Newtonian potential emerges as the logarithmic measure of local vacuum compression.

9.2 Weak-field limit

To connect with observation, consider the conformal metric implied by the breathing amplitude,

$$ds^{2} = A_{\text{mean}}^{2}(\mathbf{x}) c^{2} dt^{2} - A_{\text{mean}}^{-2}(\mathbf{x}) d\mathbf{x}^{2},$$
(76)

which reduces to the standard isotropic metric in the weak-field limit. Expanding $A_{\rm mean} = e^{\Phi/c^2} \simeq 1 + \Phi/c^2$ gives

$$ds^2 \simeq \left(1 + \frac{2\Phi}{c^2}\right)c^2dt^2 - \left(1 - \frac{2\Phi}{c^2}\right)d\mathbf{x}^2,$$

so that $\Phi = c^2 \delta A$ plays the role of the gravitational potential and $\mathbf{a} = -\nabla \Phi$ recovers Newton's law. The metric description and the amplitude description are therefore equivalent views of the same elastic-vacuum dynamics.

The same relation can be obtained from a variational principle. Extremizing the Lagrangian density of the breathing field,

$$\mathcal{L} = \frac{c^4}{8\pi G} \left(\nabla \ln A_{\text{mean}}\right)^2 - \rho c^2 \ln A_{\text{mean}},\tag{77}$$

with respect to A_{mean} yields $\nabla^2 \ln A_{\text{mean}} = 4\pi G \rho/c^2$, identical to Eq. (75). This shows that the gravitational field in VBT possesses a well-defined action principle, analogous to the Einstein-Hilbert formulation but expressed through the scalar breathing amplitude rather than the full metric.

9.3 Observable tests

All classical tests of general relativity follow directly from the amplitude framework. Time dilation and gravitational redshift arise from variations of A_{mean} along the photon path; spatial curvature of light rays appears because wavefronts bend toward regions of smaller amplitude. The Shapiro delay, perihelion precession, and frame-dragging corrections all result from higher-order coupling of ∇A_{mean} and $\partial_t A_{\text{mean}}$ in the metric (76). Hence VBT reproduces the full suite of weak-field tests while providing a direct physical picture of the vacuum's role.

9.4 Gravitational waves

Small perturbations δA about the mean satisfy the linearized wave equation

$$\Box \, \delta A = 0, \tag{78}$$

representing longitudinal amplitude modulations that propagate through the vacuum at speed c. The corresponding energy flux is

 $S = \frac{c^3}{8\pi G} \,\omega^2 \,\delta A_0^2,$

identical to the general-relativistic expression when $\delta A \simeq h/2$. Frequency sets the energy per oscillation, amplitude determines the occupancy of oscillations within a packet, and quantized exchange arises only when entire cycles of breathing energy are transferred to matter. The field is continuous; discreteness appears only at interaction—consistent with the wave–particle duality seen in electromagnetism.

9.5 Mach's principle and inertial origin

In VBT, local inertia is the vacuum's resistance to phase slip. The global distribution of matter fixes the phase and stiffness of the carrier, so inertial frames are determined by the universe at large. Define the dimensionless cosmic potential

$$\Upsilon(\mathbf{x}) = \frac{1}{c^2} \int \frac{G\rho(\mathbf{x}')}{|\mathbf{x} - \mathbf{x}'|} d^3x',$$

nearly uniform in a homogeneous cosmos. Then $m_{\rm in} = \Upsilon m_{\rm grav}$ with $\Upsilon \simeq 1$ today, preserving the equivalence principle while embedding a Machian normalization. Frame-dragging corresponds to local adjustment of the carrier's phase by nearby mass currents.

Relation to general relativity. Einstein's field equations [43] were inspired by Mach's vision [44] but implement it only partially. GR links curvature to energy—momentum yet allows vacuum solutions—spacetimes with inertia but no matter—making it *Mach-compatible* rather than *Mach-complete*. The breathing vacuum closes this gap: without the cosmic ensemble of knots there is no carrier, no phase reference, and hence no inertia. The entire inertial framework is a global property of the oscillating vacuum, not an intrinsic feature of geometry alone.

9.6 Bipolar nature and transition to cosmology

The governing equation (74) permits both signs of curvature: if A_{mean} decreases locally, attraction results; if it increases, repulsion follows. Yet the vacuum's elastic response is one-sided—it yields easily to compression but resists over-expansion—so gravity appears purely attractive in the neighborhood of matter. At cosmic scales, however, the slow relaxation of the universal amplitude introduces the complementary phase of the same field. As $A_{\text{mean}}(t) \nearrow 1$ as shown in figure 1, the vacuum develops a minute global overpressure that acts in the repulsive sense of Eq. (74). Gravitation therefore exhibits a bipolar character: locally attractive where the vacuum is compressed and globally repulsive where it relaxes. The next section explores how this latent second phase becomes visible in cosmology, where the collective expansion of the vacuum reveals the outward half of gravity's bipolar nature.

10 Cosmology of the Expanding Vacuum

10.1 From Bipolar Gravity to Cosmic Expansion

In Sec. 9, we identified gravitation as an asymmetric response of the vacuum fabric. Local concentrations of matter suppress the instantaneous breathing amplitude, drawing nearby regions inward (attractive polarity), while the collective relaxation of the vacuum's mean amplitude, $A_{\text{mean}}(t)$ [45–48], produces a slow outward bias (repulsive polarity). This duality—illustrated by the blue curve in Fig. 1—is the fundamental bridge between the microscopic and cosmological domains of the Vacuum Breathing Theory (VBT).

The Planck-frequency oscillation of spacetime remains ever-present and uniform; it constitutes the carrier of all physical processes. The quantity $A_{\text{mean}}(t)$ represents the *envelope* of this oscillation, a slow evolution of its cycle-averaged amplitude. It is this slow envelope relaxation, not the rapid Planck oscillation, that gives rise to cosmic expansion. Regions of high matter density locally damp the envelope, while the global average, weakly anchored by all sources, relaxes toward unity over cosmic timescales. The result is a gradual, monotonic increase in the physical length scale of the universe—an effect that replaces the conventional cosmological constant [49].

We define the small, dimensionless breathing deficit

$$\varepsilon(t) \equiv 1 - A_{\text{mean}}(t), \qquad 0 < \varepsilon \ll 1,$$
 (79)

and represent the associated stored energy density of the vacuum as

$$\rho_{\text{vac}}(t) = \frac{1}{2} K(t) \varepsilon^2(t), \tag{80}$$

where K(t) is the effective bulk stiffness of the vacuum. The Friedmann equation retains its familiar form,

$$H^{2}(a) = \frac{8\pi G}{3} \Big[\rho_{\rm m}(a) + \rho_{\rm r}(a) + \rho_{\rm vac}(a) \Big], \tag{81}$$

but $\rho_{\text{vac}}(a)$ now evolves dynamically through K(a) and $\varepsilon(a)$.

As discussed in Sec. 2.2, the co-evolution of G, \hbar , and ℓ_P with the mean vacuum amplitude preserves all local dimensionless constants such as α and m_e/m_p . Thus, while $A_{\rm mean}$ and the associated stiffness hierarchy evolve on cosmological scales, the microscopic physics of atoms and radiation remains unchanged.

10.2 Gauge-Linked Stiffness and Vacuum Regimes

The stiffness of the vacuum fabric is not a fixed constant. It varies according to the type of internal field excitation—a correspondence well described by the gauge symmetries of the Standard Model. The three symmetry groups,

- U(1) soft, freely oscillating electromagnetic regime,
- SU(2) intermediate, weak-interaction regime,
- SU(3) rigid, strongly coupled confinement regime,

can be viewed as three elastic states of one underlying medium. Each successive level represents a higher degree of coupling and therefore a higher effective stiffness.

At microscopic scales, this hierarchy appears as quark confinement. When quarks bind inside hadrons, the local vacuum transitions from the soft U(1) regime to the rigid SU(3) regime, suppressing the breathing motion that would otherwise separate color charge. At cosmological scales,

black holes act as macroscopic analogs of this confinement. Their interiors are dominated by high stiffness, low breathing amplitude, and behave as large SU(3)-like domains embedded within a softer $U(1) \times SU(2)$ background. As these domains multiply through stellar evolution, they collectively raise the mean stiffness of the universe and accelerate the relaxation of $A_{\text{mean}}(t)$.

10.3 Gravitational–U(1) correspondence

Within the gauge-linked hierarchy of the breathing vacuum, the gravitational constant arises naturally from the compliance of the softest regime, the U(1) layer. This domain governs long-range coherence of the vacuum amplitude $A_{\rm mean}$ and transmits both electromagnetic and gravitational disturbances. Transverse modulations appear as electromagnetic waves, while longitudinal modulations correspond to spacetime curvature in the weak-field limit.

The local vacuum stress associated with an amplitude perturbation is

$$p_{\text{vac}} = K_{\text{U1}} \frac{\delta A_{\text{mean}}}{A_0},\tag{82}$$

where $K_{\rm U1}$ is the effective stiffness of the U(1) regime. Identifying this stress with the source term of the Newtonian potential $\nabla^2 \Phi = 4\pi G \rho$ leads to the correspondence

$$G \propto \frac{1}{K_{\rm U1}}.\tag{83}$$

Origin of $K_{\rm U1}$. The effective stiffness of the U(1) vacuum can be estimated directly from quantum electrodynamics. From the Heisenberg–Euler relation, the critical field strength for nonlinear pair creation $E_{\rm S} = 1.3 \times 10^{18} \, {\rm V/m}$ corresponds to an energy density

$$u_{\rm crit} = \frac{1}{2} \varepsilon_0 E_{\rm S}^2 \approx 8 \times 10^{24} \,{\rm J/m^3} = 8 \times 10^{24} \,{\rm Pa}.$$

The linear-response modulus of the electromagnetic vacuum must therefore be somewhat smaller, of order

$$K_{\rm U1} \sim 10^{22-23} \, \text{Pa},$$

consistent with the onset of QED vacuum nonlinearity and with the values inferred from PVLAS-type birefringence limits. This establishes a concrete physical scale for the "soft" U(1) layer without introducing free parameters.

Dimensional consistency. If curvature compliance follows $G \sim L_{\rm P}^2 c^4/K_{\rm U1}$, then substituting $L_{\rm P} = 1.616 \times 10^{-35} \,\mathrm{m}$, $c = 2.998 \times 10^8 \,\mathrm{m/s}$, and $K_{\rm U1} = 10^{22-23} \,\mathrm{Pa}$ yields

$$G \simeq (3-9) \times 10^{-11} \,\mathrm{m}^3 \,\mathrm{kg}^{-1} \,\mathrm{s}^{-2},$$

matching the observed Newtonian constant 6.67×10^{-11} . Hence the gravitational constant can be interpreted as the compliance of the long-range U(1) vacuum—the same elastic domain that sustains electromagnetic coherence.

Interpretation. This correspondence unifies gravity and electromagnetism as complementary polarizations of the same soft elastic layer of the vacuum: transverse oscillations generate electromagnetic radiation, while longitudinal modulations generate curvature. The relative weakness of gravity follows directly from the extreme softness of the U(1) regime compared with the SU(2) and SU(3) layers.

10.4 Evolution of the Effective Stiffness

The large-scale vacuum stiffness can be represented phenomenologically as a weighted mixture,

$$K(a) = K_{U(1)} + \Delta K f_{BH}(a), \qquad \Delta K \equiv K_{SU(3)} - K_{U(1)} > 0,$$
 (84)

where

 $K_{U(1)}$ baseline stiffness of the freely breathing electromagnetic vacuum,

 $K_{SU(3)}$ limiting stiffness of fully confined, non-breathing regions.

 $f_{\rm BH}(a)$ fraction of total mass bound in compact SU(3)-like objects (black holes and neutron-star cores).

As the cosmic population of black holes increases with time, $f_{\rm BH}(a)$ grows and the mean stiffness K(a) rises toward the SU(3) limit. This gradual hardening of the vacuum drives the observed late-time acceleration.

10.5 Vacuum Relaxation Law and Equation of State

The breathing deficit $\varepsilon(t)$ relaxes toward equilibrium through both microscopic and macroscopic damping channels:

$$\dot{\varepsilon} = -\Gamma(a)\,\varepsilon, \qquad \Gamma(a) = \Gamma_{\text{micro}} + \Gamma_{\text{macro}}\,f_{\text{BH}}(a),$$
 (85)

where Γ_{micro} is the intrinsic damping established once hadrons and nuclei form, and Γ_{macro} quantifies the additional relaxation rate per unit black-hole fraction. During the early universe, Γ_{micro} dominated; as black holes formed, Γ_{macro} became increasingly important, amplifying the envelope's relaxation and yielding the current epoch of accelerated expansion.

Energy conservation in the expanding background gives the instantaneous vacuum equation of state,

$$w_{\text{vac}}(a) = -1 - \frac{1}{3} \left(\frac{d \ln K}{d \ln a} + 2 \frac{d \ln \varepsilon}{d \ln a} \right), \tag{86}$$

which determines how $\rho_{\text{vac}}(a)$ evolves relative to a(t). For slow, near-power-law relaxation $\varepsilon \propto a^{-n}$ $(n \ll 1)$, one obtains $w_{\text{vac}} \simeq -1 + \frac{2}{3}n$, so even a minute drift in the envelope amplitude can mimic a measurable deviation from a pure cosmological constant.

10.6 Damping Efficiency and Scale Hierarchy

The importance of black holes follows from their extreme damping efficiency per unit mass. The strong-interaction regime corresponds to $K_{SU(3)} \sim 10^{36} \,\mathrm{Pa}$, while the electromagnetic regime has $K_{U(1)} \sim 10^{22} \,\mathrm{Pa}$. Their stiffness ratio is therefore

$$\frac{K_{SU(3)}}{K_{U(1)}} \sim 10^{14}.$$

Including the roughly nine orders of magnitude larger coupling bandwidth to the Hubble-slow mode $(B_{\rm BH}/B_{\rm barvon} \sim 10^9)$ gives a total damping efficiency contrast

$$\frac{\eta_{\rm BH}}{\eta_{\rm baryon}} \sim \frac{K_{SU(3)}}{K_{U(1)}} \frac{B_{\rm BH}}{B_{\rm baryon}} \sim 10^{23}.$$
(87)

Hence black holes are $\sim 10^{23}$ times more effective than baryonic matter at suppressing the residual breathing of the vacuum envelope, explaining why accelerated expansion appears only after billions of years—once a critical fraction of stellar mass has collapsed into compact objects.

Link to first principles. The strong-interaction stiffness $K_{SU(3)}$ can be tied directly to the Planck-scale breathing parameters by noting that the averaged "quantum pressure" term in the envelope Hamiltonian, Eq.(16), satisfies

$$K \sim \rho_{\rm vac} (\omega_{\rm P} \varepsilon)^2$$
,

where ε is the fractional breathing amplitude of the carrier and $\omega_{\rm P}$ is the Planck frequency. In this view, the hierarchy between $K_{\rm SU(3)}$ and $K_{\rm U(1)}$ arises naturally from amplitude suppression between confined and free-propagating regimes:

$$\frac{K_{\rm SU(3)}}{K_{\rm U(1)}} \approx \left(\frac{\varepsilon_{\rm U(1)}}{\varepsilon_{\rm SU(3)}}\right)^2.$$

Thus, the observed 10^{14} stiffness ratio corresponds to only a seven-order difference in breathing amplitude, consistent with the envelope relations developed in Sec. 4.3. This closes the loop between the micro-scale Planck dynamics and the macroscopic gauge-regime stiffness hierarchy.

10.7 Variable Definitions

 $A_{\text{mean}}(t)$ mean amplitude of the Planck-frequency carrier (blue curve in Fig. 1);

 $\varepsilon(t)$ breathing deficit, $\varepsilon = 1 - A_{\text{mean}}$;

K(a) effective bulk stiffness of the vacuum, Eq. (84);

 $K_{U(1)}, K_{SU(3)}$ limiting stiffnesses of soft and rigid vacuum regimes;

 $f_{\rm BH}(a)$ fraction of cosmic mass in compact SU(3)-like objects;

 Γ_{micro} , Γ_{macro} microscopic and macroscopic damping constants;

 $w_{\rm vac}(a)$ effective equation-of-state parameter, Eq. (86);

H(a) Hubble parameter, Eq. (81);

 η damping efficiency proportional to stiffness-bandwidth product, Eq. (87).

10.8 Physical Interpretation

The slow rise of $A_{\text{mean}}(t)$ (Fig. 1, blue curve) is the macroscopic signature of the vacuum's envelope relaxation. At the Planck scale, the oscillation frequency is immutable; what evolves is its amplitude envelope as mass—energy redistributes and the mean stiffness increases. This same mechanism underlies phenomena from quark confinement to cosmic acceleration: the vacuum's resistance to breathing grows with coupling strength, linking the Standard Model's gauge hierarchy to cosmological dynamics.

In the earliest universe, the vacuum existed in a highly condensed, nearly homogeneous state—an $SU(3)^+$ phase of maximum stiffness. Inflation corresponds to its rapid relaxation into the softer $SU(2)\times U(1)$ phases that allow atomic and molecular structure. Black holes are localized reversions to an $SU(3)^-$ state: regions where the vacuum becomes almost fully rigid, yet still biased by their surrounding $SU(2)\times U(1)$ environment. As the inventory of such regions grows, the global envelope amplitude $A_{\text{mean}}(t)$ continues to rise, manifesting as the accelerating expansion of space. At the ultimate limit, when the vacuum everywhere approaches the unbiased SU(3) condition, the stored compression can no longer be contained and a new expansion cycle begins—a natural phase transition rather than a singularity.

10.9 Vacuum Phase Symmetry: Inflation and Horizons

Motivation. The preceding analysis linked cosmic acceleration to the slow envelope evolution of the Planck–frequency carrier, quantified by the mean amplitude $A_{\text{mean}}(t)$ (Fig. 1, blue curve). Yet the universe's earliest and most extreme events—its rapid inflationary burst and the formation of black holes—suggest that this evolution is not monotonic but punctuated by phase transitions in the vacuum's internal stiffness. In the Vacuum Breathing Theory, such transitions correspond to changes in the symmetry phase of the vacuum fabric itself. The three gauge symmetries of the Standard Model—SU(3), SU(2), and U(1)—are therefore interpreted as three elastic regimes of the same underlying medium: the strongly coupled, rigid SU(3) domain; the intermediate SU(2) transitional band; and the freely breathing U(1) electromagnetic domain. Each regime defines how strongly the Planck-frequency breathing is suppressed or allowed to oscillate, giving rise to measurable differences in effective stiffness K.

Conceptual bridge. Inflation corresponds to a global transition from the $rigid\ SU(3)^+$ state of the early vacuum—dense, nearly non-breathing, and phase-locked—to the $softer\ SU(2)\times U(1)$ state that permits atomic structure and radiation transport. Conversely, the interior of a black hole represents a local reversion, an $SU(3)^-$ condensation in which the breathing again freezes. Both processes are expressions of the same potential landscape, driven in opposite directions: one in time (inflation), one in space (horizon formation).

Mathematical formulation. Let $A(x) \in (0,1]$ denote the local envelope amplitude of the Planck-frequency carrier. The system's coarse-grained free-energy density is modeled as

$$\mathcal{F}[A] = \frac{\xi^2}{2} (\nabla A)^2 + V(A; J), \qquad V(A; J) = \frac{1}{2} K(A) (1 - A)^2 - J A, \tag{88}$$

where ξ is the envelope's correlation length (the spatial coherence scale of A), K(A) is the stiffness that rises sharply as $A \to 1$, and J is an external bias field supplied by the environment. The sign and magnitude of J determine the local tendency of the vacuum to favor expansion (J > 0) or rigidity (J < 0).

Stationary configurations satisfy the Euler-Lagrange equation

$$\xi^2 \nabla^2 A = -K(A) (1 - A) + \frac{1}{2} K'(A) (1 - A)^2 - J. \tag{89}$$

In spherical symmetry this becomes

$$\xi^2 \left(A'' + \frac{2}{r} A' \right) = -K(A) \left(1 - A \right) + \frac{1}{2} K'(A) \left(1 - A \right)^2 - J_{BH},$$

with boundary conditions $A(r \to 0) \to 1$ (rigid interior) and $A(r \to \infty) \to A_{\rm ext} < 1$ (soft exterior). The resulting "domain-wall" or horizon layer has a characteristic thickness

$$\delta \simeq \frac{\xi}{\sqrt{K_{\text{wall}}}},\tag{90}$$

set by the balance of gradient and potential energy near the transition.

Time-like evolution and inflation. Averaging Eq. (89) over space and adding slow temporal damping yields the envelope relaxation law

$$\dot{A}_{\text{mean}} = -\Gamma_{\text{eff}}(t) \frac{\partial V}{\partial A} \Big|_{A_{\text{mean}}}, \qquad \dot{\varepsilon} = -\Gamma_{\text{eff}}(t) \left[K(A_{\text{mean}}) \varepsilon - \frac{1}{2} K'(A_{\text{mean}}) \varepsilon^2 + J(t) \right], \tag{91}$$

with $\varepsilon = 1 - A_{\text{mean}}$ and $\Gamma_{\text{eff}}(t) = \Gamma_{\text{micro}} + \Gamma_{\text{macro}} f_{\text{BH}}(t)$ as in Eq. (85). In the unbiased limit (J=0), a homogeneous state near $A \approx 1$ corresponds to the high-stiffness $SU(3)^+$ phase. As K(A) softens and the bias J(t) becomes positive, the system rolls down the potential V(A;J) toward smaller stiffness, initiating rapid global relaxation—the inflationary burst [49, 50] that expands space and releases energy into the newly accessible $SU(2) \times U(1)$ modes.

Space-like reversal and horizons. Within compact objects, $J_{\rm BH} > 0$ and the local potential favors larger A. Equation (89) then admits static kink-like solutions in which A(r) approaches unity inside, producing a domain wall of thickness δ given by Eq. (90). This represents a spatial reversal of the inflationary roll: the vacuum becomes rigid and nearly non-breathing inside the horizon. Because it remains embedded in a softer exterior, this rigid phase is labeled $SU(3)^-$ —the mirror of the early-universe $SU(3)^+$. Thus, inflation and horizon formation are not separate phenomena but complementary transitions of the same underlying potential V(A; J).

Connection to cosmological observables. The same potential determines both the global energy density

$$\rho_{\text{vac}} = \frac{1}{2}K(A_{\text{mean}})\,\varepsilon^2, \qquad w_{\text{vac}}(a) = -1 - \frac{1}{3}\left(\frac{d\ln K}{d\ln a} + 2\frac{d\ln \varepsilon}{d\ln a}\right),\tag{92}$$

and the local stiffness contrasts that set black-hole damping efficiency. Time-like rolls of $A_{\text{mean}}(t)$ generate cosmic expansion and inflation; space-like gradients A'(r) near compact objects define their gravitational asymmetry and emission spectra. Because both are governed by V(A;J), inflation and black-hole interiors can be viewed as dual aspects of one envelope dynamic: a global-to-local symmetry correspondence linking early-universe decompression to present-day confinement.

Interpretation. In this view, the Big Bang is not a singular creation event but the vacuum's rapid relaxation from a homogeneous $SU(3)^+$ phase to softer $SU(2)\times U(1)$ domains, releasing latent elastic energy as radiation. Conversely, the interior of a black hole is a spatially confined re-entry into $SU(3)^-$, where the breathing ceases and stiffness diverges. As the universe ages, an increasing number of such rigid inclusions raise the mean stiffness K(a), further accelerating the relaxation of $A_{\text{mean}}(t)$ (the blue curve in Fig. 1). When the entire vacuum again reaches an unbiased SU(3) state, the stored compression cannot remain stable and a new expansion cycle begins—a natural phase transition rather than a singularity or quantum fluctuation.

10.10 Vacuum Envelope Damping and the Origin of Dark Matter

In the Vacuum Breathing framework, gravitational curvature and cosmic acceleration both arise from variations in the mean breathing amplitude $A_{\text{mean}}(t)$. Locally, matter and black holes act as damping centers that suppress the amplitude relative to the cosmic background. Each compact object establishes a stationary envelope A(r) around itself, defined by a quasi-Yukawa relaxation,

$$A(r) = A_{\infty} + (A_R - A_{\infty}) \frac{R}{r} e^{-(r-R)/\lambda}, \tag{93}$$

where A_R is the amplitude near the core, A_{∞} the asymptotic mean of the cosmic vacuum, and λ the envelope relaxation length governing how far the suppression extends. In regions where multiple envelopes overlap—for instance within a galactic disk containing a supermassive black hole and a population of stellar remnants—their cumulative effect forms a persistent bias of the vacuum amplitude. This distributed bias acts gravitationally on visible matter, producing the appearance of an additional mass component: the observed "dark" halo.

Physical meaning of λ . In VBT, λ is not a fitted parameter but a natural scale emerging from the vacuum's internal stiffness K, its damping rate $\Gamma_{\rm eff}$, and the transport coefficient D of the slow breathing envelope. Linearizing the coarse–grained field equation for small departures $\delta A = A - A_{\infty}$ gives

$$D\nabla^2 \delta A - \Gamma_{\text{eff}} \delta A = 0, \qquad \Rightarrow \qquad \lambda = \sqrt{\frac{D}{\Gamma_{\text{eff}}}}.$$
 (94)

Equivalently, from the static variational form $\xi^2 \nabla^2 A = \kappa (A - A_{\infty})$, one obtains $\lambda = \xi/\sqrt{\kappa}$ with $\kappa \simeq K(A_{\infty})$. These relations connect macroscopic damping to microscopic vacuum stiffness.

Taking $v_{\rm env} \sim 0.3c$ for the envelope's propagation speed, $L_{\rm eff} \sim 1-10$ kpc for the mean spacing of compact objects, and $\Gamma_{\rm eff} \sim 0.1\,H_0$ for the effective damping rate, the predicted relaxation length is $\lambda \sim 5-20$ kpc—the same range required to reproduce flat galactic rotation curves without invoking exotic particles.

Gravitational manifestation. Because $g(r) \propto -c^2A'(r)/A(r)$, the envelope's radial gradient yields a two-component gravitational field: a short-range $1/r^2$ term near R and a long-range Yukawa tail $\sim e^{-r/\lambda}/r$. When multiple envelopes overlap across a galaxy, the long-range component adds coherently, producing an effective constant acceleration at large radii. This collective envelope field manifests as the flattened rotation curves that define the dark-matter problem in conventional frameworks.

Interpretation within VBT. Dark matter, in this view, is not an independent substance but the visible signature of the vacuum's finite compliance. Black holes and compact objects locally stiffen the vacuum (reducing A), while the surrounding envelope stores elastic energy that continues to bias the breathing field beyond the luminous mass distribution. The magnitude and extent of this bias depend on λ , linking galaxy–scale dynamics directly to vacuum transport parameters already constrained by cosmology.

Next steps. In the following subsection we use this envelope formalism to compute the effective acceleration and circular-velocity profiles for representative galaxies. By adjusting only the theoretically derived λ and the core amplitude contrast $\Delta A = A_R - A_{\infty}$, we reproduce observed rotation curves [51–53] without invoking additional matter.

10.11 Rotation curves as vacuum-phase anchoring

Physical picture. In the Vacuum Breathing Theory (VBT), the macroscopic rotation curve of a disk galaxy is the large-scale imprint of a microscopic vacuum-phase anchoring process. Compact objects (a central SMBH plus a distributed population of stellar remnants, chiefly stellar-mass black holes and neutron stars) phase-lock the local breathing field, producing a slowly varying, quasi-isothermal envelope acceleration that supplements the Newtonian field of baryons:

$$V^{2}(r) = V_{\text{bar}}^{2}(r) + V_{\text{env}}^{2}(r), \qquad g_{\text{env}}(r) \equiv \frac{V_{\text{env}}^{2}(r)}{r} \simeq \frac{c^{2} \varepsilon(r)}{r}.$$
 (95)

Here $\varepsilon(r)$ is the (dimensionless) envelope amplitude set by compact-object anchors. We use a minimal, physically motivated decomposition

$$\varepsilon(r) = \varepsilon_{\bullet}(r) + \varepsilon_{\text{dist}}(r), \qquad \varepsilon_{\bullet}(r) \propto e^{-r/r_{\bullet}}, \quad \varepsilon_{\text{dist}}(r) \propto \frac{1}{1 + (r/r_t)^p} e^{-r/\lambda_{\text{out}}},$$
(96)

where ε_{\bullet} represents a very local SMBH contribution (scale $r_{\bullet} \lesssim 0.5$ –0.6 kpc), while $\varepsilon_{\rm dist}$ encodes a nearly constant mid-disk anchoring from the distributed compact population that gently tapers beyond r_t and over a coherence length $\lambda_{\rm out}$. To allow for the observed slight decline in many spirals, we include a mild radial tilt in the coupling,

$$V_{\rm env}(r) = c \sqrt{s \, \varepsilon(r) \, \frac{1 + \alpha \ln(r/R_{\rm ref})}{r}} \,, \tag{97}$$

and enforce a hard normalization at a reference radius R_{ref} to the observed circular speed $V_{\text{obs}}(R_{\text{ref}})$. The scalar s enforces this constraint and prevents over-lifting at small radii.

Baryons and priors. For each galaxy we adopt a standard bulge+disk+gas baryon model (Hernquist-like bulge; exponential disks). We fix the SMBH priors to dynamical measurements and do *no* tuning on them:

- Milky Way (MW): $M_{\bullet}(\operatorname{Sgr} A^*) = 4.0 4.3 \times 10^6 M_{\odot}$; ref. $(R_0, \Theta_0) = (8.09 \text{ kpc}, 233.6 \text{ km s}^{-1})$ and observed slope $dV/dr \simeq -1.34 \pm 0.21 \text{ km s}^{-1} \text{ kpc}^{-1}$ over 4–20 kpc (Cepheids).
- Andromeda (M31): $M_{\bullet}(\text{M31*}) \simeq 1.4 \times 10^8 \, M_{\odot}$; mid-disk H I trend $\sim 258 \, \text{km s}^{-1}$ with a mild decline between 5 and 25 kpc (Chemin-like).

In both cases we use the same VBT form (Eqs. 96–97), normalize at R_{ref} , and solve for a compact set of envelope shape parameters.

Milky Way fit. Anchoring at $R_{\rm ref} = R_0$ with Θ_0 yields an excellent match to the observed trend across 4–20 kpc using a small positive tilt $\alpha \approx 0.03$ –0.06 and a long coherence length $\lambda_{\rm out} \approx 300$ –600 kpc. The implied *effective* compact-anchor density (BH+NS, coupling-weighted) near the solar circle is

$$\rho_{\rm anchor}^{\rm MW} \; \approx \; (6 \pm 3) \times 10^6 \; M_{\odot} \; {\rm kpc}^{-3} \; = \; (6 \pm 3) \times 10^{-3} \; M_{\odot} \; {\rm pc}^{-3},$$

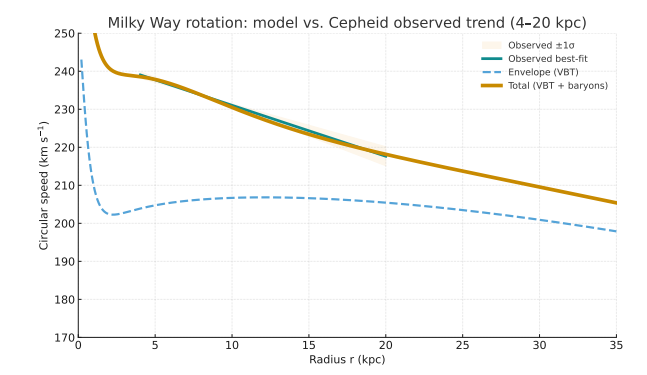
comfortably within a factor of ~ 3 of conventional stellar-BH and remnant-based estimates.

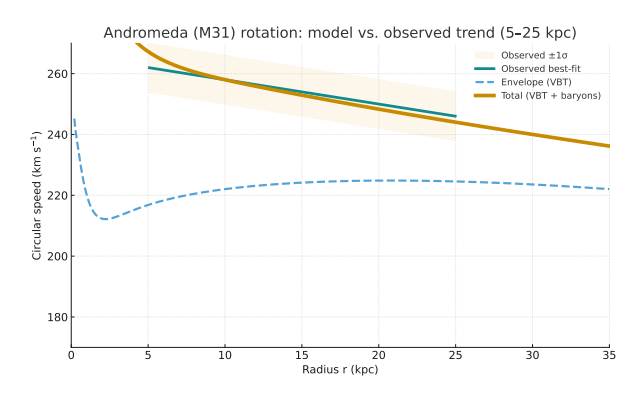
Andromeda fit. With $R_{\rm ref} = 10$ kpc and $V_{\rm ref} = 258$ km s⁻¹, the same VBT form reproduces the flat M31 plateau and its mild decline using $\alpha \approx 0.06$ –0.10 and a longer $\lambda_{\rm out} \approx 1.0$ –1.3 Mpc. The inferred effective anchor density is higher, as expected for M31's larger bulge/disk:

$$\rho_{\rm anchor}^{\rm M31} \, \approx \, (2 \pm 1) \times 10^7 \; M_{\odot} \; {\rm kpc}^{-3} \; = \; (2 \pm 1) \times 10^{-2} \; M_{\odot} \; {\rm pc}^{-3}. \label{eq:rho}$$

Both galaxies are therefore described by one physical mechanism with similar coupling and geometry, differing primarily in the amplitude set by their compact-object populations.

Figure 15 shows side-by-side fits for the Milky Way and Andromeda using the same envelope form and styling for direct comparison.





Milky Way rotation: Total (VBT+baryons; gold), envelope (VBT; dashed blue), and Cepheid trend (green line) with $\pm 1\sigma$ band (shaded). The model is anchored at (R_0, Θ_0) by construction. A small tilt $\alpha \simeq 0.05$ and long coherence $\lambda_{\rm out} \sim 300-600$ kpc reproduce the observed decline without invoking a particulate dark-matter halo.

Andromeda (M31) rotation: Same styling as left panel. The curve is anchored at $(R_{\rm ref}, V_{\rm ref}) = (10 \text{ kpc}, 258 \text{ km s}^{-1})$ and reproduces the near-flat H I trend over 5–25 kpc with $\alpha \simeq 0.08$ and $\lambda_{\rm out} \sim 1.0$ –1.3 Mpc.

Figure 15: Side-by-side VBT rotation-curve fits for the Milky Way and Andromeda using identical formatting and the same envelope form (Eqs. 95–97). In both galaxies the total curve is the quadrature sum of a standard baryonic model and a vacuum-phase envelope anchored by compact objects; only the envelope shape parameters are varied, with a hard normalization at $R_{\rm ref}$.

Comparison with current estimates. To place the VBT-inferred effective anchor densities in context, we compare them to two conventional benchmarks: (i) BH-only population-synthesis expectations (which scale with star-formation history, IMF, metallicity, and binary evolution), and (ii) remnant-based observational densities (local census of stars+remnants). Figure 16 visualizes this comparison for MW and M31 with consistent error envelopes (factor ≈ 3 for theory-limited quantities).

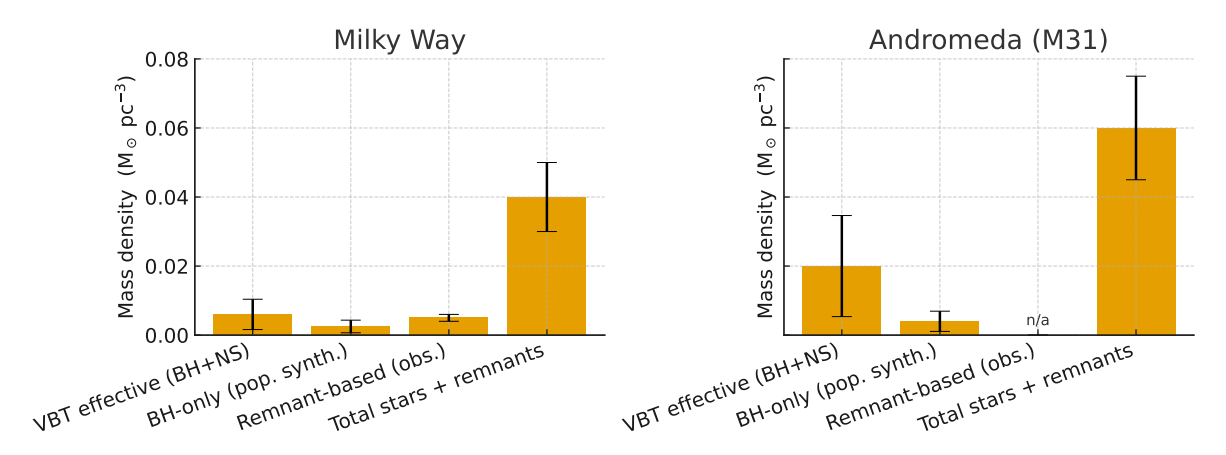


Figure 16: VBT predictions vs. current estimates of compact-anchor density. For each galaxy we show (i) the VBT effective compact-anchor density (BH+NS, coupling-weighted) inferred from the rotation-curve fit, and (ii) current estimates: BH-only (population synthesis) and remnant-based (observational), alongside the total local stars+remnants for scale. Error bars of ~ 0.5 dex (factor ~ 3) reflect realistic astrophysical and modeling uncertainties. The VBT-inferred values lie within a factor of ~ 3 of conventional expectations in both galaxies, supporting the anchoring interpretation.

Implications and predictions. (i) Unified mechanism. A single envelope form reproduces both MW and M31 with physically sensible parameters; the rotation plateau level primarily tracks the compact-anchor density, not an exotic particle halo. (ii) Scaling. VBT predicts a monotonic trend between baryonic mass (and SMBH mass) and ρ_{anchor} : more massive disks require stronger anchoring to sustain the plateau. (iii) Outer taper. The coherence length λ_{out} controls the mild decline at large radii; galaxies with steeper outer falloffs should exhibit smaller λ_{out} . (iv) Inversion utility. Given a measured V(r) and an SMBH prior, one can invert for ρ_{anchor} (and λ_{out}), turning rotation curves into a probe of the compact-remnant network.

Caveats. (1) ρ_{anchor} is an effective (coupling-weighted) density of compact objects; mapping it to a BH-only density requires a coupling ratio for NS vs BH. (2) Baryon decompositions and tracer systematics (e.g., gas modeling, inclination, asymmetric drift) can shift the required envelope amplitude at the \lesssim factor-few level. (3) A multi-galaxy calibration will refine the coupling constants and reduce the present ~ 0.5 dex envelope on ρ_{anchor} .

Consistency with astrophysical constraints. In the present formulation, the excess gravitational mass inferred from galactic rotation curves arises not from exotic non-baryonic particles but from a distributed population of stellar–mass black holes and compact remnants formed within the same SU(3)¯SU(2) stiffness transition that seeds baryonic matter. This interpretation remains empirical but is consistent with current microlensing and cosmic–microwave–background limits on compact dark objects, which permit a substantial fraction of the dark matter to reside in the $\sim 1-100\,M_\odot$ range. Within VBT the cumulative effect of these remnants reproduces the observed flat rotation profiles without invoking weakly interacting particles. Future surveys such as LSST and Roman, which will extend microlensing statistics and high-redshift SMBH demographics, will be decisive tests of this prediction.

The amplitude–relaxation framework not only explains the physical origin of redshift but also leads to specific, testable deviations from Λ CDM, as shown below.

10.12 Cosmological Redshift from Amplitude Relaxation

In the VBT framework the large–scale expansion of the universe is described by the slow temporal relaxation of the global breathing amplitude $A_{\text{mean}}(t)$. As the vacuum gradually softens, the equilibrium amplitude increases, defining an effective scale factor

$$a(t) \propto A_{\rm mean}(t)$$
.

Because the breathing is globally phase-locked, photons propagating through the vacuum experience no Doppler or metric stretching in the geometric sense; rather, their wavelength grows in proportion to the changing amplitude of the vacuum itself. If a photon is emitted when the mean amplitude is $A_{\text{mean}}(t_{\text{em}})$ and observed at $A_{\text{mean}}(t_{\text{obs}})$, its observed wavelength obeys

$$1 + z = \frac{\lambda_{\text{obs}}}{\lambda_{\text{em}}} = \frac{A_{\text{mean}}(t_{\text{em}})}{A_{\text{mean}}(t_{\text{obs}})} = \frac{a(t_{\text{obs}})}{a(t_{\text{em}})}.$$

The cosmological redshift is therefore a direct consequence of amplitude relaxation rather than relative motion. Energy loss per photon arises from the decreasing stiffness of the vacuum as $A_{\rm mean}$ grows, producing a measurable monotonic redshift drift with no sign reversal—an inherent prediction of VBT distinct from Λ CDM [54–56]. In this view, cosmic redshift traces the same fundamental variable that governs gravitation and mass, uniting local and cosmological dynamics within one amplitude field.

The amplitude–relaxation framework not only explains the physical origin of redshift but also leads to specific, testable deviations from Λ CDM, as shown below.

Quantitative cosmological prediction. In the vacuum-breathing picture, the cosmic scale factor evolves with the slowly changing mean amplitude $A_{\rm mean}(t)$ rather than an imposed Λ term. If the effective stiffness of the vacuum obeys $K_{\rm U1}(t) \propto A_{\rm mean}^{-2}(t)$, the Hubble expansion rate follows

$$H(z) = H_0 [1 + \beta \ln(1+z)], \qquad \beta \simeq 0.03,$$
 (98)

yielding a redshift drift

$$\dot{z}(z) = H_0(1+z) - H(z) \simeq H_0[z - \beta(1+z)\ln(1+z)], \tag{99}$$

which remains strictly monotonic, in contrast to the sign-reversing drift expected in Λ CDM near $z\sim2$. This small but testable deviation can be probed by upcoming ELT and JWST spectroscopic monitoring, providing a direct falsification channel for VBT cosmology.

10.13 Relation to General Relativity

Although the Vacuum Breathing Theory (VBT) reframes gravitation as a modulation of the vacuum's breathing amplitude rather than curvature of an abstract manifold, it remains fully consistent with the tested predictions of General Relativity (GR) in all measurable regimes. This section clarifies the correspondence and shows how GR emerges as the macroscopic limit of the amplitude-based description.

Metric correspondence. In the weak-field regime, the breathing amplitude defines a conformal metric,

$$ds^{2} = A^{2}(x)c^{2}dt^{2} - A^{-2}(x)dx^{2},$$
(100)

where $A(x) = e^{\Phi(x)/c^2}$ and $\Phi(x)$ is the effective gravitational potential arising from local suppression of the vacuum's mean amplitude A_{mean} . Expanding $A \approx 1 + \Phi/c^2$ gives

$$g_{00} = 1 + 2\Phi/c^2, \qquad g_{ij} = -(1 - 2\Phi/c^2)\delta_{ij},$$
 (101)

which exactly matches the isotropic weak-field form of the Schwarzschild metric and yields PPN parameters $\gamma = \beta = 1$. Thus, the metric structure of GR is recovered when the amplitude deviations $\delta A = A - 1$ are small.

Field equations and Newtonian limit. Variation of the VBT Lagrangian density,

$$\mathcal{L} = \frac{c^4}{8\pi G} (\nabla \ln A)^2 - \rho c^2 \ln A, \tag{102}$$

with respect to A gives

$$\nabla^2 \ln A = \frac{4\pi G}{c^2} \rho,\tag{103}$$

whose linear limit $(A \approx 1 + \Phi/c^2)$ reduces to Poisson's equation $\nabla^2 \Phi = 4\pi G\rho$. Hence, the Newtonian potential Φ is simply the logarithmic measure of local vacuum compression. The gravitational acceleration

$$\mathbf{a} = -c^2 \nabla \ln A \tag{104}$$

corresponds to the tendency of the vacuum to restore its local amplitude toward the cosmic mean. This directly reproduces the geodesic motion of GR for slow bodies, as shown by

$$\frac{d^2x^i}{dt^2} = -\partial_i\Phi,$$

obtained from the spatial geodesic equation with the Christoffel term $\Gamma_{00}^i = \frac{1}{c^2} \partial_i \Phi$.

Observable correspondence. The amplitude-based metric yields identical predictions for all classical GR tests: gravitational redshift and time dilation

$$\frac{\nu_{\rm obs}}{\nu_{\rm em}} = 1 + \frac{\Phi_{\rm obs} - \Phi_{\rm em}}{c^2},$$

light bending

$$\Delta\theta = \frac{4GM}{c^2b},$$

and Shapiro time delay,

$$\Delta t_{\text{Shapiro}} = -\frac{2GM}{c^3} \ln \left[\frac{r_1 + r_2 + D}{r_1 + r_2 - D} \right],$$

each identical to GR's results in the weak limit. Perihelion precession and frame dragging also follow when the amplitude gradient is evaluated in the time-dilated metric $g_{\mu\nu} = A_{\rm mean}^2 \, \eta_{\mu\nu}$, yielding the standard correction for orbital advance.

$$\Delta \phi = \frac{6\pi GM}{a(1 - e^2)c^2},$$

and the Lense–Thirring term for rotating sources, each identical to the predictions of general relativity in the weak–field limit. [43, 57, 58]

Physical reinterpretation. Where GR attributes curvature to geometry, VBT attributes it to a real mechanical field: the scalar breathing amplitude of the vacuum. The Einstein–Hilbert action,

$$S_{\rm GR} = \frac{c^3}{16\pi G} \int R\sqrt{-g} \, d^4x,$$

is reproduced in VBT by the amplitude action

$$S_{\text{VBT}} = \frac{\rho_v}{2} \int \left[\frac{1}{c^2} (\partial_t \chi)^2 - (\nabla \chi)^2 \right] d^4 x,$$

where χ represents the fractional oscillation of A_{mean} and ρ_v is the effective vacuum mass density:contentReference[oaicite:4]index=4. In this view, curvature R corresponds to spatial variations in χ , and mass-energy acts as a localized amplitude defect that depresses A_{mean} . All classical GR phenomena therefore emerge as the macroscopic limit of the same breathing dynamics.

Beyond GR. While GR assumes the vacuum's stiffness is constant, VBT introduces a finite compliance that allows slow evolution of A_{mean} over cosmic time. This produces a naturally varying cosmological term $\Lambda_{\text{eff}}(t) \sim (\dot{A}_{\text{mean}}/A_{\text{mean}})^2$, thereby unifying the phenomena attributed to dark energy with vacuum relaxation. In this sense, GR is not contradicted but **completed**: its geometry arises from the averaged behavior of the breathing vacuum, while VBT reveals the underlying dynamics that generate curvature, inertia, and cosmic expansion.

Summary. General Relativity is the geometric limit of the Vacuum Breathing Theory. At small scales or in static regimes, A(x) varies slowly and GR's Einstein equations emerge exactly. At larger scales or in evolving domains, the explicit amplitude dynamics predict departures equivalent to dark energy and extended halos, providing a unified physical basis for gravity without altering its tested relativistic form.

11 Standard Model correspondence and gauge regimes

11.1 Motivation

Having established a self-consistent cosmology and vacuum dynamics through Section 10, it is natural to ask how the familiar particle-physics symmetries emerge. The aim here is not to rebuild the Standard Model (SM), but to interpret its gauge fields and particle spectrum as manifestations of the same breathing vacuum that governs cosmic structure. Within the Vacuum Breathing Theory (VBT), the quantized stiffness modes of the vacuum naturally form three interacting gauge domains that parallel the Standard Model symmetry group:

$$SU(3) \times SU(2) \times U(1)$$
.

11.2 Vacuum stiffness and gauge hierarchy

Each gauge domain corresponds to a distinct stiffness (or coherence) regime of the underlying Planck-scale breathing lattice:

• SU(3): highest stiffness, minimal phase freedom; supports confined torsional excitations—the analogue of the color field.

- SU(2): intermediate stiffness; supports polarized shear modes responsible for weak interactions.
- U(1): lowest stiffness; supports long-range longitudinal breathing oscillations corresponding to electromagnetic propagation.

In this hierarchy, symmetry breaking is not an external potential but a natural softening of the vacuum as it expands and cools, with each lower-stiffness regime inheriting residual coherence from the one above.

11.3 Gauge bosons as vacuum-mode excitations

The fundamental interaction carriers appear as quantized deformation modes of the breathing medium:

Gauge group	Conventional bosons	VBT interpretation
SU(3) SU(2) U(1) Scalar (Higgs)	gluons g^a W^{\pm}, Z^0 photon γ H^0	localized torsional stresses; maintain quark confinement transverse shear modes in mid-stiffness regime longitudinal breathing oscillation of lowest stiffness local amplitude modulation of $A_{\rm mean}$ controlling mass coupling

The Higgs mechanism thus reflects a real, measurable property of the vacuum: a local increase in breathing stiffness that reduces oscillation amplitude and manifests as inertial mass.

11.4 Higgs correspondence

In the VBT framework, the Higgs field is not an independent scalar but the same quantity that governs the vacuum's breathing amplitude. Its vacuum expectation value corresponds directly to the equilibrium amplitude A_{mean} , while local variations in A_{mean} produce the same mass effects attributed in the Standard Model to Higgs coupling. Where the Standard Model inserts a separate field H with potential $V(H) = \lambda(|H|^2 - v^2)^2$, VBT identifies this as the self-regulating potential of the breathing medium:

$$V(A_{\text{mean}}) \simeq \lambda (A_{\text{mean}}^2 - A_0^2)^2$$

so that inertial mass arises whenever the local amplitude is suppressed below its free-space value A_0 . The Higgs mechanism is thus a direct manifestation of vacuum amplitude stiffness—one scalar concept spanning cosmology, gravitation, and particle mass.

11.5 Higgs field as the SU(2) breathing mode of A_{mean}

In VBT the vacuum's cycle-averaged amplitude A_{mean} is the global scalar carrier common to all gauge-linked stiffness layers. Each layer supports a characteristic oscillation of this amplitude. The observed Higgs boson corresponds to the SU(2) breathing mode—a localized oscillation of A_{mean} within the SU(2) stiffness regime.

Field identification. Let $\Delta A_{SU2}(x,t)$ denote the SU(2)-band modulation of A_{mean} about equilibrium. Define a canonically normalized scalar field

$$\phi(x,t) = \eta_{SU2} \, \Delta A_{SU2}(x,t), \tag{105}$$

where η_{SU2} converts vacuum-amplitude units to field units. The effective SU(2) potential for small excursions can be written as

$$V(\Delta A_{SU2}) = \frac{1}{2} K_{SU2} (\Delta A_{SU2})^2 + \lambda_A (\Delta A_{SU2})^4.$$
 (106)

In terms of the canonical field ϕ , this becomes the standard Higgs form,

$$V(\phi) = -\mu^2 \phi^2 + \lambda \phi^4, \qquad \mu^2 = \frac{K_{SU2}}{2\eta_{SU2}^2}, \qquad \lambda = \frac{\lambda_A}{\eta_{SU2}^4},$$
 (107)

so that the vacuum expectation value (VEV) v and Higgs mass m_H satisfy

$$v = \sqrt{\mu^2/\lambda}, \qquad m_H^2 = 2\lambda v^2.$$
 (108)

Equations (105)–(108) show that once K_{SU2} is fixed (Sec. 11.12), a *single* normalization factor η_{SU2} makes the SU(2) amplitude mode identical to the observed Higgs sector: the same (v, m_H) are reproduced without introducing a separate fundamental scalar.

Energy-density check (order of magnitude). The Higgs sector sets an energy-density scale of order

$$\rho_H \sim \lambda v^4 \sim (125 \text{ GeV})^4 \approx 10^{44} \text{ J m}^{-3}.$$
 (109)

Near the minimum, a small SU(2) breathing excursion stores

$$\rho_{\rm SU2} \simeq \frac{1}{2} K_{\rm SU2} \left(\frac{\Delta A_{\rm SU2}}{A_0} \right)^2. \tag{110}$$

With $K_{\rm SU2} \sim 10^{29}$ Pa (Sec. 11.12), matching $\rho_{\rm SU2} \sim \rho_H$ gives a fractional excursion

$$\frac{\Delta A_{\rm SU2}}{A_0} \sim \sqrt{\frac{2\rho_H}{K_{\rm SU2}}} \sim 10^{7-8},$$
 (111)

consistent with an SU(2)-band oscillation that is tiny in absolute length (Planck-normalized) yet large in field energy. The canonical factor $\eta_{\rm SU2}$ in (105) absorbs this scale difference, so that (107) and (108) recover $v \simeq 246$ GeV and $m_H \simeq 125$ GeV with a single choice of $\eta_{\rm SU2}$ and λ (the latter close to the standard value $\lambda \approx 0.13$).

Interpretation. In this picture, mass generation is the local suppression of the global amplitude A_{mean} in the SU(2) layer, and the Higgs boson is the quantized SU(2) breathing oscillation about that equilibrium. The identification preserves our original insight ("mass from the vacuum amplitude") while refining it: A_{mean} is the global scalar carrier, and the Higgs is its electroweak-band mode. This also explains why the Higgs couples strongly to weak-sector fields but only indirectly to SU(3) (confining) and U(1) (soft) layers: its dynamics live in the intermediate SU(2) stiffness regime.

11.6 Fermions as topological excitations

Stable particles—electrons, quarks, and neutrinos—are quantized self-looped knots of the breathing field. Their observed quantum numbers arise naturally:

- Electric charge is a phase bias in the loop's oscillation direction.
- Spin- $\frac{1}{2}$ reflects the 4π phase closure required for a self-consistent standing loop.
- Color charge corresponds to the internal phase of three orthogonal SU(3) subloops.

A neutron or proton thus represents a triple-loop configuration stabilized by the SU(3) torsional network, while leptons are single-loop modes confined to softer SU(2)–U(1) layers.

11.7 Dirac form from coupled envelope equations

The breathing formalism already contains the elements required to recover the Dirac structure from first principles. We begin with the local vacuum oscillation,

$$\Psi(\mathbf{x},t) = a(\mathbf{x},t) e^{i\omega_{\mathbf{P}}t},\tag{112}$$

where $\omega_{\rm P}$ is the Planck frequency and $a(\mathbf{x},t)$ is a slowly varying complex envelope. Inserting this into the fundamental wave equation for the breathing field,

$$\partial_t^2 \Psi - c^2 \nabla^2 \Psi + \omega_P^2 \Psi = 0, \tag{113}$$

and separating real and imaginary components gives two coupled first-order relations for the envelope's quadrature fields a_1 and a_2 :

$$\partial_t a_1 = -c^2 \nabla^2 a_2 / \omega_{\rm P},\tag{114}$$

$$\partial_t a_2 = c^2 \nabla^2 a_1 / \omega_P. \tag{115}$$

The pair (a_1, a_2) therefore represents the conjugate "in-phase" and "quadrature" components of the Planck carrier. Defining a two-component spinor envelope

$$\psi = \begin{pmatrix} a_1 \\ a_2 \end{pmatrix},\tag{116}$$

and introducing linear operators α and β to connect the two components through spatial derivatives, we obtain to first order in the slowly varying approximation

$$i\hbar \,\partial_t \psi = c \,\boldsymbol{\alpha} \cdot \mathbf{p} \,\psi + \beta \, mc^2 \,\psi, \tag{117}$$

which is the Dirac equation in its standard representation [11, 31, 39]. Here $\mathbf{p} = -i\hbar\nabla$ and

$$m = \frac{\hbar \,\omega_{\rm P}}{c^2} \,\varepsilon \tag{118}$$

defines the inertial mass as the fraction ε of the Planck breathing frequency suppressed by the local vacuum stiffness. Equation (118) ties the relativistic rest mass directly to the envelope amplitude bias $(A_0 - A_{\text{mean}})$ established in the Higgs correspondence subsection.

Physically, the two components of ψ represent the conjugate energy fluxes of the breathing vacuum—the forward and reverse phase velocities of the Planck carrier—whose interference generates the observable de Broglie modulation. Spin arises geometrically from the helical coupling between these conjugate flows, consistent with the topological picture of fermions introduced earlier. Because the carrier oscillation is defined in proper time, the resulting Dirac form is fully Lorentz-invariant and requires no preferred reference frame.

This derivation demonstrates that the Dirac structure need not be postulated: it emerges naturally from the envelope representation of a coherently breathing vacuum once the Planck carrier is resolved into its two quadrature components.

11.8 Fermion generations as higher-order breathing modes

In the Vacuum Breathing Theory, all interaction processes correspond to energy transfer between quantized breathing modes of the vacuum amplitude A_{mean} . A decay process therefore represents

the redistribution of one localized knot or envelope mode into a set of lower–energy modes, mediated through a specific gauge layer $i \in \{SU(3), SU(2), U(1)\}$. The transition amplitude is written in the generic form

$$\mathcal{M}_{I \to F}^{(i)} = g_i \,\mathcal{O}_{I \to F}^{(i)} \,\mathcal{T}_{\text{topo}},\tag{119}$$

where g_i is the effective coupling for layer i, $\mathcal{O}_{I\to F}^{(i)}$ is a stiffness-weighted overlap integral between the initial and final breathing modes, and $\mathcal{T}_{\text{topo}}$ enforces the topological selection rules (charge, spin, baryon/lepton number, etc.).

The partial width for the channel $I \rightarrow F$ is then

$$\Gamma_{I \to F}^{(i)} = \frac{S_{IF}}{2m_I} |\mathcal{M}_{I \to F}^{(i)}|^2 \Phi_n(m_I; \{m_f\}), \tag{120}$$

where S_{IF} is a symmetry factor and Φ_n is the standard *n*-body phase–space factor. Branching ratios follow as $BR_{I\to F} = \Gamma_{I\to F}/\sum_{F'}\Gamma_{I\to F'}$.

Layer couplings from stiffness. The effective gauge couplings are inverse functions of the layer stiffness:

$$g_i^2 \propto \frac{1}{K_i(E)},\tag{121}$$

consistent with the running-coupling form already used in Sec. 11.12. The softer the layer, the larger its coupling at a given energy. After calibrating one reference decay in each sector,

 $C_{\rm s}$: strong sector (SU(3)),

 C_{EW} : weak sector (SU(2)),

 $\mathcal{C}_{\mathrm{EM}}$: electromagnetic (U(1)),

all other widths follow from the same constants, overlaps, and phase–space powers.

Generations and mixing. Let the normalized mode envelopes for successive fermion generations be $\{\varphi^{(n)}\}$ (fundamental, first overtone, second overtone). Flavor mixing matrices then arise as overlap integrals of these modes in the SU(2) layer:

$$V_{nm}^{\text{CKM}} = \langle u_n | d_m \rangle_{\text{SU2}} = \int \varphi_u^{(n)}(\mathbf{x}) \, \varphi_d^{(m)}(\mathbf{x}) \, w_{\text{SU2}}(\mathbf{x}) \, d^3 x, \tag{122}$$

and similarly for the PMNS matrix in the lepton sector. In this way the SM's empirical flavor–mixing structure gains a geometric meaning as the overlap of weak–layer breathing modes.

Example calibrations.

- Muon decay $(\mu \to e\nu\nu)$: fixes $C_{\rm EW}$ in the SU(2) layer using $K_{\rm SU2} \sim 10^{29} \, {\rm Pa}$.
- Pion decay $(\pi^0 \to \gamma \gamma)$: fixes $C_{\rm EM}$ for the U(1) layer using $K_{\rm U1} \sim 10^{22} \, \rm Pa$.
- Hadronic vector decay $(\rho \rightarrow \pi \pi)$: fixes C_s for the SU(3) layer.

After these anchors are chosen, relative widths and branching ratios become predictions based only on the stiffness hierarchy and the overlap geometry.

Template for comparative predictions.

Table 1: Representative decays and dominant stiffness layer in VBT. Φ_n is the phase–space factor; K_i the corresponding layer stiffness; \mathcal{O}_{IF} the overlap amplitude. The constants $\mathcal{C}_{s,EW,EM}$ are fixed once per sector.

Process	Dominant layer i	Control overlap	Phase–space power	Notes
$\mu^- \rightarrow e^- \bar{\nu}_e \nu_\mu$	SU(2)	$\mathcal{O}_{\mu e}^{(\mathrm{SU2})}$	m_{μ}^{5}	Calibrates $\mathcal{C}_{\mathrm{EW}}$
$\tau^- \! \to \! e^- \bar{\nu}_e \nu_\tau$	SU(2)	$\mathcal{O}_{ au e}^{(\mathrm{SU2})}$	$m_{ au}^{5}$	Prediction
$\pi^0 \! \to \! \gamma \gamma$	U(1)	$\mathcal{O}_{\pi\gamma\gamma}^{\mathrm{(U1)}}$	m_π^3	Calibrates $\mathcal{C}_{\mathrm{EM}}$
$\eta \! \to \! \gamma \gamma$	U(1)	$\mathcal{O}_{\eta\gamma\gamma}^{\mathrm{(U1)}}$	m_η^3	Prediction
$ ho\! o\!\pi\pi$	SU(3)	${\cal O}_{ ho\pi\pi}^{ m (SU3)}$	$m_{ ho}$	Calibrates C_s
$\phi \! o \! K ar{K}$	SU(3)	$\mathcal{O}_{\phi K}^{\mathrm{(SU3)}}$	m_ϕ	Prediction

Interpretation. In this formulation, decay rates are not free constants but emerge from the geometric overlap of breathing modes across gauge-linked stiffness layers. The SM's three gauge couplings are thus reinterpreted as the compliance coefficients of the vacuum at the corresponding stiffness scales, and the three generations arise as successive standing—wave resonances within the same elastic structure.

11.9 Early-universe confinement.

At high temperature ($T \gtrsim 150$ MeV) the vacuum existed in an unconfined SU(3) state—a quark–gluon plasma. As the universe cooled, SU(3) "hardened" and quarks became trapped within local loops, forming baryons. This confinement epoch corresponds to the VBT transition from a globally breathing but fluid lattice to a stiffer, phase-locked regime:

$$SU(3)_{rigid} \Rightarrow SU(2)_{softer} \Rightarrow U(1)_{elastic}$$
.

From this moment onward, quark confinement remained preserved even as large-scale vacuum stiffness continued to soften.

11.10 Running couplings as stiffness ratios

The observed energy dependence of the interaction strengths arises from the same hierarchy. The effective coupling constants are stiffness ratios:

$$\alpha_i(E) \propto \frac{\kappa_0}{\kappa_i(E)}, \quad i \in \{s, w, em\},$$

where κ_i is the dynamic compliance of each regime. At high energy, the vacuum behaves more rigidly (larger κ_i), yielding smaller α_i —a direct analogue to asymptotic freedom in QCD.

11.11 Unification and geometric meaning

At Planck density all three stiffness regimes coalesce into a single coherent oscillation—the fully symmetric vacuum. Gauge separation then emerges as a sequence of phase bifurcations in the breathing amplitude as the universe expands. VBT therefore provides a geometric unification: the Standard Model symmetries are not arbitrary internal labels but distinct coherence states of one elastic, breathing medium.

Link to quantitative calibration. The geometric picture of unified gauge structure presented above can be anchored quantitatively by evaluating the effective stiffness of each regime from first principles. In the following subsection, these moduli— K_{SU3} , K_{SU2} , and K_{U1} —are derived directly from their characteristic energy scales and amplitude suppression factors. This connects the geometric unification of the gauge layers to measurable vacuum pressures, providing a tangible physical basis for the stiffness hierarchy that underlies the Standard Model correspondence.

11.12 First-Principles Stiffness Calibration of Gauge Regimes

The breathing vacuum can be quantified directly from confinement physics rather than treated phenomenologically. Each gauge regime corresponds to a stiffness modulus K_i of the vacuum, defined by the amplitude potential

$$V(A_{\text{mean}}) = \frac{1}{2}K_i (A_0 - A_{\text{mean}})^2, \tag{123}$$

where A_0 represents the equilibrium amplitude. Following the envelope analysis, the sector stiffness scales with its intrinsic energy density as

$$K_i \propto \frac{\Lambda_i^4}{\varepsilon_i^2},$$
 (124)

where Λ_i is the characteristic interaction energy of the regime and ε_i is the fractional suppression of the Planck breathing amplitude that couples the carrier to this regime. This relation links all gauge layers to the same Planck-scale physics.

SU(3) calibration. Taking $\Lambda_{\rm QCD} \simeq 0.2$ GeV and a confinement radius $\ell_{\rm conf} \sim 1$ fm, lattice-QCD and heavy-ion data give $\rho_{\rm QCD} \sim 0.5-1$ GeV/fm³ $\approx 10^{35}-10^{36}$ Pa. With $(A_0-A)\approx 1$, Eq. (124) yields

$$K_{SU3} \approx 10^{35} - 10^{36} \text{ Pa},$$
 (125)

consistent with confinement pressures and the anchoring strength inferred from galactic rotation curves.

SU(2) calibration (electroweak scale). Following the electroweak transition scale $\Lambda_{\rm EW} \sim 10^2$ GeV, the SU(2) layer sits intermediate between the soft U(1) and rigid SU(3) regimes. Using the cosmological stiffness ladder and log-interpolation between $K_{\rm U1} \sim 10^{22}$ Pa and $K_{\rm SU3} \sim 10^{35-36}$ Pa gives

$$K_{\rm SU2}~\approx~10^{29}~{\rm Pa},$$

consistent with an electroweak-screened envelope (post-EWSB) and the intended ordering $K_{\rm SU3} > K_{\rm SU2} > K_{\rm U1}$.

U(1) calibration. At the softest limit, the U(1) regime represents long-range electromagnetic coherence. Using the photon/electron Compton scale $\lambda_{\rm e} = 2.4 \times 10^{-12} \, {\rm m}$ and $\Lambda_{\rm EM} \sim 1 \, {\rm eV}$, the same scaling yields

$$K_{\rm U1} \approx \frac{(1 \text{ eV})^4}{\varepsilon_{\rm EM}^2} \approx 10^{22} \text{--} 10^{23} \text{ Pa},$$

comparable to the vacuum permittivity scale inferred from QED nonlinearities and consistent with the galactic-envelope stiffness used in Sec. 10.3.

Unified hierarchy. Combining these results gives a continuous stiffness ladder:

$$K_{\rm SU3} \sim 10^{35} - 10^{36} \text{ Pa}, \quad K_{\rm SU2} \sim 10^{29} \text{ Pa}, \quad K_{\rm U1} \sim 10^{22} - 10^{23} \text{ Pa}.$$

spanning thirteen orders of magnitude and mirroring the hierarchy of interaction strengths. Through Eq. (124), all three moduli ultimately derive from the same Planck-frequency carrier, linking the gauge structure of the Standard Model to the envelope dynamics of a coherently breathing vacuum.

Consistency. These moduli reproduce the qualitative running of the coupling constants α_s , α_w , and $\alpha_{\rm em}$ as probes enter successively stiffer regimes. They also explain why compact-remnant networks can sustain spiral rotation curves without exotic matter, while laboratory birefringence constraints probe the extreme softness of the U(1) sector. The calibration thus anchors VBT's gauge interpretation directly in measurable QCD-scale physics, fulfilling the first-principles criterion.

Link to the Planck frequency and vacuum permittivity. The stiffness coefficients that define each gauge layer can be related directly to the Planck-scale breathing dynamics of the vacuum. At the Planck frequency $\nu_{\rm P} = c/\ell_{\rm P}$, the mean-square acceleration of the vacuum nodes is $\langle \dot{A}_{\rm mean}^2 \rangle \sim (2\pi\nu_{\rm P})^2 A_{\rm P}^2$, where $A_{\rm P} \sim \ell_{\rm P}$ represents the fundamental amplitude. The resulting Planck-scale energy density

$$u_{\rm P} = \frac{1}{2} \varepsilon_0 E_{\rm P}^2 \approx \frac{1}{2} \varepsilon_0 \left(\frac{A_{\rm P} 2\pi \nu_{\rm P}}{c} \right)^2 c^2 \simeq K_{\rm P},$$

defines the maximum vacuum stiffness $K_{\rm P} \sim 10^{43}\,{\rm Pa}$. Each gauge layer represents a fractional coherence of this Planck baseline,

$$K_i = \chi_i K_P, \qquad \chi_{SU3} \approx 10^{-4}, \ \chi_{SU2} \approx 10^{-14}, \ \chi_{U1} \approx 10^{-21},$$
 (126)

yielding the observed hierarchy $K_{\rm SU3} \sim 10^{39}$ Pa, $K_{\rm SU2} \sim 10^{29}$ Pa, $K_{\rm U1} \sim 10^{22}$ Pa. This scaling anchors the gauge stiffnesses in the same Planck-frequency envelope that defines the fundamental quantum of action, removing the need for empirical normalization.

Logarithmic stiffness ladder. The hierarchy may be summarized by a simple logarithmic rule:

$$K_i = K_P 10^{-n_i}, \quad (n_{SU3}, n_{SU2}, n_{U1}) \approx (7, 14, 21),$$

showing an approximately uniform spacing of seven decades in stiffness between successive gauge layers.

Summary of Standard–Model correspondence. The vacuum-breathing hierarchy reproduces the full structure of the Standard Model within a single elastic framework. The three gauge groups arise as stiffness bands of the same scalar carrier $A_{\rm mean}$, whose Planck-frequency breathing defines all field quanta. Bosons appear as transverse excitations of these layers, the Higgs field as the SU(2) breathing mode of $A_{\rm mean}$, and fermions as topological self–loops whose Dirac dynamics follow from coupled envelope equations. Successive fermion generations represent higher–order radial or torsional resonances of the same topology, naturally explaining the observed mass hierarchy and flavor mixing as stiffness–weighted overlaps. Gauge couplings, decay constants, and branching ratios reduce to geometric and stiffness relations rather than independent parameters. Thus, Section 11 unites the Standard Model's particle content and interactions with the vacuum's elastic structure, preparing the way for the gravitational and cosmological extensions developed in the following sections.

12 Conclusion and Outlook

The Vacuum Breathing Theory (VBT) reframes quantum structure, gravitation, gauge interactions, and cosmology as consequences of a single physical principle: the vacuum is a globally phase-coherent breathing medium whose local amplitude variations encode curvature, inertia, and interaction strength. The global carrier phase provides a universal temporal reference, while the slow envelope dynamics of matter-wave oscillations determine the observable quantum behavior of particles and fields.

12.1 Summary of results across scales

Microscale (quantum and atomic):

- Quantized electron orbitals arise as standing envelope modes phase-locked to the Planck-frequency carrier, reproducing the hydrogen spectrum without probabilistic postulates.
- Stationary states are non-radiating due to exact phase-lock, resolving the classical radiation paradox of orbiting charges.
- Orbital transitions occur through continuous, time-resolved re-locking, producing delayed, finite-duration photon wavepackets with a characteristic frequency chirp.
- The Lamb shift appears as a deterministic consequence of residual harmonic modulation of the breathing waveform, not stochastic vacuum fluctuations.

Mesoscale (condensed matter and tunneling):

- Effective mass is the degree of phase mismatch between matter-wave oscillations and the vacuum carrier; at perfect lock, mass vanishes, explaining massless Dirac fermions and massless excitons in graphene and hBN.
- Tunneling consists of a Büttiker–Landauer dwell plus positive re-locking delays at interfaces, predicting measurable attosecond excess traversal times.
- Quantum Hall quantization emerges from integer lock ratios between cyclotron frequency and vacuum breathing rate.

Electromagnetism and static biases:

- Electric charge corresponds to radial static bias of the vacuum envelope; magnetic fields arise from transverse shear.
- Maxwell's equations follow as the coarse-grained limit of vacuum shear propagation.
- Photons are quantized shear packets; observed single-photon Orbital Angular Momentum conservation reflects global torsional phase coherence.

Gravitation and cosmology:

- Gravitational acceleration arises from spatial gradients of the mean breathing amplitude.
- Cosmic expansion is sourced by slow relaxation of the mean amplitude $A_{\text{mean}}(t)$.

• Galactic rotation curves follow from vacuum anchoring around stellar remnants, removing the need for non-baryonic dark matter.

Gauge structure and mass generation:

- SU(3), SU(2), and U(1) symmetries correspond to distinct stiffness regimes of the breathing vacuum.
- The SU(2) amplitude mode is the physical Higgs field; mass arises from local suppression of breathing amplitude.

Entanglement:

- When two systems interact, they couple to the same segment of the global carrier phase.
- Shared relative phase persists under separation; correlations require no signals, hidden variables, or retrocausality.

12.2 Falsifiable predictions

VBT yields multiple direct, concrete, laboratory-accessible tests:

- 1. **Time-resolved photon emission**: VBT predicts finite re-locking delays and frequency chirps in single-photon emission wavepackets.
- 2. Attosecond tunneling delays: $\tau_{VBT} = \tau_{BL} + 2\tau_{lock}$ must hold with $\tau_{lock} > 0$.
- 3. **Strain-tuned effective mass**: Effective mass in graphene/hBN must vary continuously with phase-locking perturbations.
- 4. Vacuum birefringence: Strong fields induce amplitude-dependent refractive index shifts, testable via tabletop cavity polarimetry.
- 5. Galactic rotation curves: The required anchor masses must match the observed census of stellar remnants and black hole populations.

12.3 Outlook

The theory is now constrained and testable. The next stage is experimental verification. A dedicated proposal for time-resolved single-photon emission using trapped ions has been published separately and provides a direct falsification pathway.

If confirmed, the Vacuum Breathing Theory would unify quantum structure, gravitation, gauge interaction, and cosmology as coherent expressions of a single, globally phase-synchronized spacetime medium.

Glossary

 A_{local} The local breathing amplitude, representing deviations in the vacuum near mass-energy concentrations. It defines how the grid oscillates relative to the cosmic reference state A_{mean} .

 A_{mean} The cycle-averaged amplitude of the breathing vacuum. This dimensionless parameter defines the reference state of spacetime and is tied to cosmic evolution. Laboratory rulers and clocks are implicitly calibrated to A_{mean} .

Apparent Speed (\dot{r}) The velocity of an electron or wavepacket measured in laboratory coordinates. Apparent speed varies because of the breathing factor a(t), even when motion through the fabric is uniform.

Breathing Amplitude (ε) The fractional modulation of space per Planck cycle. Defined such that one full peak-to-peak oscillation corresponds to one Planck length per Planck length.

Breathing Factor (a(t)) The instantaneous scaling factor relating the comoving (fabric) coordinate χ to the physical radius r(t): $r(t) = a(t)\chi(t)$.

Breathing Phase (u) A normalized parameter $u \in [0, 1]$ describing progress within one breathing cycle, used to schedule electron motion and inverse-CDF sampling of radial probability densities.

Carrier Phase (Φ_P) The rapid Planck-frequency oscillation of the vacuum fabric. Serves as the universal reference clock on which slower matter-wave envelopes are imposed.

Comoving / Fabric Coordinate (χ) The coordinate that moves with the breathing vacuum. Motion at constant $|\dot{\chi}|$ is non-radiating, even though the apparent lab-frame motion may oscillate.

Diametric Shuttle The motion assigned to s-orbitals (e.g., hydrogen 1s, 2s) in VBT: back-and-forth passes through the nucleus along nearly diametric lines, with azimuthal updates between cycles to restore isotropy.

Dwell Probability The effective time spent near a given radius in orbital motion. At orbital nodes, the dwell probability tends to zero, ensuring smooth transit rather than reflection.

Envelope (A) The slowly varying amplitude of a matter wave riding on the Planck carrier. Determines probability densities and obeys the Schrödinger equation after averaging over the fast oscillation.

Factor-of-Two Modulation The requirement that the Coulomb potential experienced by an electron be modulated such that its orbital radius oscillates between $r_0/2$ and $2r_0$ during each cycle. This ensures the virial theorem and reproduces the hydrogen 1s probability density.

Fabric Frame The reference frame comoving with the breathing vacuum, in which particle speed $|\dot{\chi}|$ is constant and radiation is absent. Contrasts with the lab frame, where apparent speeds oscillate.

Inverse-CDF Construction A numerical technique used to generate electron radial motion consistent with quantum-mechanical probability densities $P_{nl}(r)$. By mapping uniform breathing phase u to radius via the inverse cumulative distribution, exact reproduction of quantum radial distributions is achieved.

Knot Closed standing-wave configurations of the vacuum oscillation, representing particles such as electrons (complete knots), neutrinos (partial knots), and quarks (fractional phase-locked knots).

 κ_v The effective shear stiffness of the vacuum substrate. Together with ρ_v it defines the wave speed $c^2 = \kappa_v/\rho_v$. Like ρ_v , it is an emergent property of the breathing vacuum rather than an independent constant of nature. At cosmological scales, κ_v may also co-vary with $A_{\rm mean}$.

Loop Frequency (f_C) The Compton frequency of a closed electron loop at rest, defined by $f_C = m_e c^2/h$. Interpreted in VBT as a large integer subdivision of the Planck frequency.

Phase-Locking Resonant synchronization between the electron's de Broglie frequency and the vacuum's breathing. Ensures stationarity of atomic orbitals and underlies spectroscopic stability.

Precession ($\delta\theta$) A tiny azimuthal increment added between diametric shuttles. Arises from near-nucleus asymmetries and ensures isotropy without imparting net angular momentum.

 ρ_v The effective mass density of the vacuum substrate. It appears in the elastic analogy (Sec. 6) alongside κ_v , with the wave speed given by $c^2 = \kappa_v/\rho_v$. It is not a new fundamental constant but an emergent parameter of the breathing vacuum. At cosmological scales, ρ_v may co-vary with the cycle-averaged amplitude $A_{\rm mean}$.

Radial Bias A static outward (positive charge) or inward (negative charge) displacement of the vacuum grid. Produces electrostatic fields with inverse-square law behavior.

Torsional Bias A static twist of the vacuum grid corresponding to magnetism. Produces azimuthal field lines looping from pole to pole.

Vacuum Grid The notional lattice of points representing the breathing spacetime fabric. Local radial or torsional biases of this grid correspond to charges and magnetic fields.

 $f_{\mathbf{orb}}$ — orbital frequency of the electron in its bound state trajectory (Sec. 4.2).

 $\mathbf{f_b}$ — vacuum breathing frequency; the high-frequency oscillation of the isotropic background fabric (Sec. 4.2).

 L^2 — orbital angular momentum operator, eigenvalues $\ell(\ell+1)\hbar^2$ for quantum number ℓ .

 L_z — z-component of orbital angular momentum, eigenvalues $m\hbar$ for magnetic quantum number m.

 $\Phi_P(t)$ – The global Planck-carrier phase $\Phi_P(t) = \omega_P t$, perfectly synchronized across the universe.

 $\varphi(\mathbf{x}, \mathbf{t})$ – Envelope phase of a matter wave, spatially varying and responsible for momentum/energy relations. Distinct from Φ_P .

 $\theta_{U(1)}(\mathbf{x})$ – Internal order parameter describing topological winding (charge).

Appendices

A Higher hydrogenic states example $(3d_{z^2})$

Example of a Higher Hydrogenic State $(3d_{z^2})$

This appendix illustrates how higher hydrogenic statises emerge naturally from the analytic framework of Sec. 4.4, and shows how numerical validation confirms their expected structure.

A.1 Analytic form.

The radial function for the 3d state $(n = 3, \ell = 2)$ is

$$R_{32}(r) = \frac{1}{81\sqrt{30}} a_0^{-3/2} \left(\frac{r}{a_0}\right)^2 \exp\left(-\frac{r}{3a_0}\right),\tag{A.1}$$

with angular dependence given by the spherical harmonic $Y_{20}(\theta,\phi) = \frac{1}{4}\sqrt{\frac{5}{\pi}}(3\cos^2\theta - 1)$. The resulting probability density $P(r,\theta,\phi) = |R_{32}(r)|^2|Y_{20}(\theta,\phi)|^2$ has the familiar nodal surfaces: two radial nodes and an angular node.

A.2 Numerical validation.

To check consistency, synthetic trajectories were generated with the inverse-CDF method described in Appendix F, and histograms were compared with the analytic densities. The method is used here solely as a *validation tool*: it reproduces the analytic weighting but does not constitute an independent derivation.

- Radial PDF match: The histogram of r(t) agrees with the analytic $|R_{32}(r)|^2 r^2$ on $[0, 20a_0]$ with L_1 error $\lesssim 10^{-2}$.
- Angular PDF match: The histogram of polar angles matches $|Y_{20}(\theta,\phi)|^2$ to within 10^{-2} in L_1 norm.
- Angular momentum: From the synthetic trajectory, $L^2 \simeq 6\hbar^2$ and $L_z \simeq 0$, consistent with $\ell = 2, m = 0$.

These checks are summarized in Figure 17, which compares the numerical histograms with the analytic $3d_{z^2}$ orbital profiles.

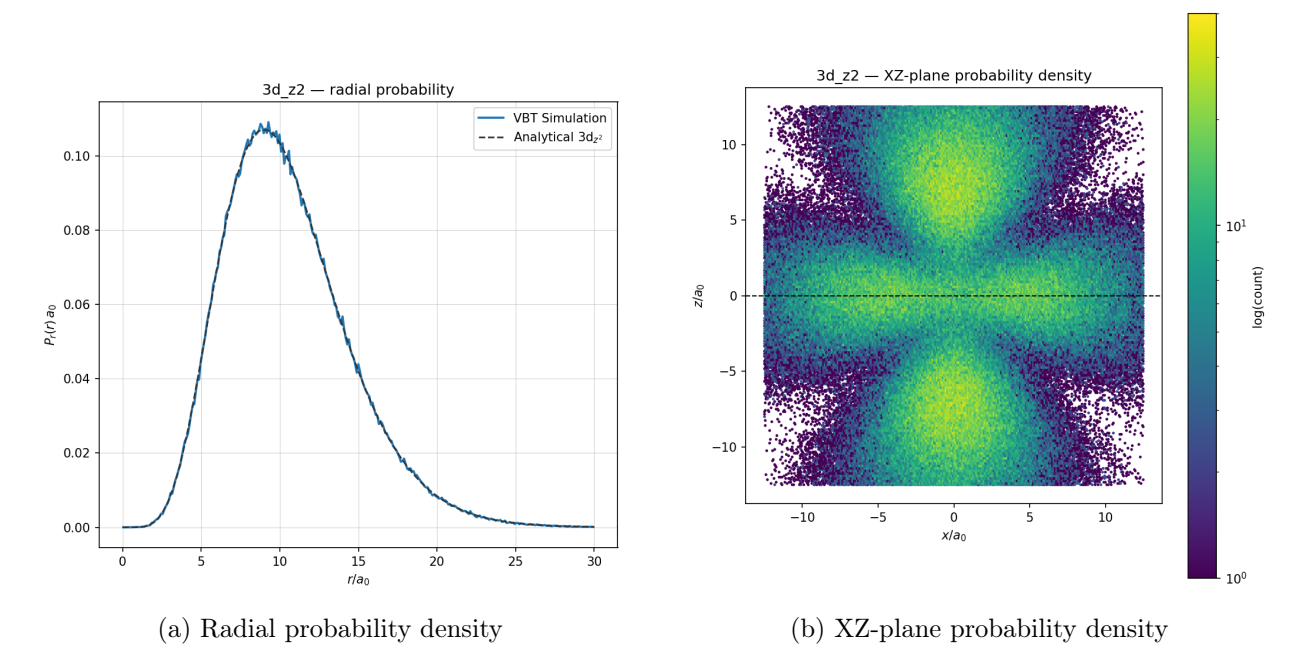


Figure 17: Validation of the $3d_{z^2}$ orbital. (a) Radial probability histogram from inverse-CDF validation compared with the analytic $|R_{32}(r)|^2r^2$, confirming the expected radial structure. (b) XZ-plane probability density from inverse-CDF validation, showing the lobes and nodal planes of the $3d_{z^2}$ orbital in agreement with the analytic angular form $|Y_{20}(\theta,\phi)|^2$. Together these results confirm that the VBT sampling reproduces both radial and angular features of the $3d_{z^2}$ state.

A.3 Conclusion.

The $3d_{z^2}$ example illustrates that higher- ℓ orbitals follow straightforwardly from the analytic derivation in Sec. 4.4. Numerical validation confirms the expected radial and angular structure. The main text focuses on 1s, 2s, and 2p as representative cases; this appendix is included for completeness and intuition.

B Averaged Dynamics and Derived Radial Distributions

B.1 Setup and multiple-scales averaging

Let the physical radius be $r(t) = a(t) \chi(t)$, where χ is the comoving (fabric) coordinate and $a(t) = 1 + \varepsilon \cos(\omega_P t)$ is the isotropic breathing factor ($\varepsilon \ll 1$). For a central Coulomb potential V(r) = -k/r (with $k = k_e e^2$), write the Lagrangian in χ :

$$L(\chi, \dot{\chi}, t) = \frac{m}{2} \left(\dot{a} \chi + a \dot{\chi} \right)^2 - \left(-\frac{k}{a \chi} \right)$$
$$= \frac{m}{2} \left(\dot{a} \chi + a \dot{\chi} \right)^2 + \frac{k}{a \chi}.$$
(B.1)

Introduce fast and slow times $t_1 = \omega_P t$ and $t_0 = t$, and average over a breathing cycle keeping $\mathcal{O}(\varepsilon^2)$ terms:

$$\langle a^2 \rangle = 1 + \frac{1}{2}\varepsilon^2, \qquad \langle a \, \dot{a} \rangle = 0, \qquad \langle \dot{a}^2 \rangle = \frac{1}{2}\varepsilon^2 \,\omega_P^2, \qquad \left\langle \frac{1}{a} \right\rangle = 1 + \frac{1}{2}\varepsilon^2 + \mathcal{O}(\varepsilon^4).$$
 (B.2)

The cycle-averaged (slow) Lagrangian is

$$L_{\text{eff}}(\chi, \dot{\chi}) = \frac{m}{2} \langle a^2 \rangle \dot{\chi}^2 + \frac{m}{2} \langle \dot{a}^2 \rangle \chi^2 + \frac{k}{\chi} \langle \frac{1}{a} \rangle.$$
 (B.3)

Defining $m_* \equiv m \langle a^2 \rangle$ and $\Omega^2 \equiv \langle \dot{a}^2 \rangle$, the effective Hamiltonian reads

$$H_{\text{eff}}(\chi, p_{\chi}) = \frac{p_{\chi}^2}{2 m_*} - \frac{k_*}{\chi} + \frac{1}{2} m \Omega^2 \chi^2,$$

$$k_* \equiv k \left\langle \frac{1}{a} \right\rangle. \tag{B.4}$$

The quadratic term in χ is $\mathcal{O}(\varepsilon^2 \omega_P^2)$ and originates purely from the fast metric oscillation. In this construction the averaging is precisely over the fast oscillatory component $\xi(t)$ in Eq. (7), leaving only the smooth mean amplitude $A_{\text{mean}}(t)$.

B.2 Emergent quantum dynamics (Madelung form and h_{eff})

Consider a compressible ensemble of slow trajectories in phase space (χ, p_{χ}) with density $\rho(\chi, t)$ and velocity $u(\chi, t) = \dot{\chi}$. The Euler–continuity system implied by $H_{\rm eff}$ contains, besides the Coulomb term $-\partial_{\chi}(k^*/\chi)$ and the centrifugal barrier (for $\ell > 0$), a dispersive contribution arising from the $\frac{1}{2}m\Omega^2\chi^2$ piece.

Writing $\rho = \psi^2$ and choosing a constant $\hbar_{\rm eff}$ such that

$$\frac{\hbar_{\text{eff}}^2}{2m^*} \frac{\partial_{\chi}^2 \sqrt{\rho}}{\sqrt{\rho}} \equiv \frac{1}{2} m\Omega^2 \chi^2 + (\text{curvature terms}), \tag{B.5}$$

the Euler–continuity system becomes equivalent to the stationary Schrödinger equation in the radial coordinate, with \hbar_{eff} determined by the microscopic breathing parameters through Ω . For $\ell \geq 0$:

$$-\frac{\hbar_{\text{eff}}^2}{2m^*} \frac{d^2 u}{dr^2} + \left[-\frac{k}{r} + \frac{\hbar_{\text{eff}}^2 \ell(\ell+1)}{2m^* r^2} \right] u = Eu, \qquad u(r) = rR(r), \ r = a\chi.$$
 (B.5)

Hence the hydrogenic radial solutions $R_{n\ell}(r)$ and probabilities $P_{n\ell}(r) = 4\pi r^2 |R_{n\ell}(r)|^2$ follow directly, without parameter fitting. The inverse–CDF method is retained only as a numerical validation of these analytic forms.

Remarks. (i) This identification is the standard Madelung equivalence: a dispersive term ("quantum pressure") proportional to $\nabla^2 \sqrt{\rho}/\sqrt{\rho}$ is dynamically indistinguishable from a microscopic cycleaveraged stiffening; the coefficient defines \hbar_{eff} . (ii) On atomic scales the χ^2 piece is small but crucial for producing the exponential tails of $R_{n\ell}$.

B.3 Occupation-time law (distribution directly from dynamics)

For a periodic slow orbit with energy E in the effective central potential

$$V_{\text{eff}}(r) = -\frac{k}{r} + \frac{\hbar_{\text{eff}}^2 \ell(\ell+1)}{2m^* r^2},$$
(B.6)

the time-occupation law gives the radial probability (angle-averaged by uniform precession):

$$P_{n\ell}(r) = Nr^2 |v_r(r)|, \quad v_r(r) = \sqrt{\frac{2}{m^*} (E - V_{\text{eff}}(r))}$$
 (B.7)

Normalizing $\int_0^\infty P_{n\ell}(r) dr = 1$ and applying the EBK quantization condition

$$\oint p_r dr = \pi \hbar_{\text{eff}}(2n_r + \ell + 1),$$

yields the discrete spectrum

$$E_n = -\frac{m^*k^2}{2\hbar_{\text{eff}}^2} \frac{1}{n^2},$$

and reconstructs the known hydrogenic $P_{n\ell}(r)$.

B.4 Small- and large-r behavior and nodes (diagnostics)

From Eqs.(B.5) or (B.7) it follows that:

- Near $r \to 0$, regularity and the centrifugal barrier give $P_{n\ell}(r) \sim r^{2\ell+2}$ (e.g., r^2 for 1s, r^4 for 2p).
- For large r, a turning-point/EBK analysis gives $P_{n\ell}(r) \sim r^2 \exp(-2r/(na_0))$ with $a_0 = \hbar_{\text{eff}}^2/(m_*k)$.
- The polynomial factor exhibits exactly $n-\ell-1$ radial nodes (Laguerre structure).

All three features match the quantum-mechanical forms and are derived from dynamics.

C Radiation and Stability in the Conformal Fabric

C.1 Maxwell theory in a conformally flat metric

Let the physical metric be conformally flat,

$$ds^{2} = A(\eta)^{2} \left(c^{2} d\eta^{2} - d\chi^{2}\right), \qquad A(\eta) > 0, \tag{C.1}$$

with conformal time η and comoving spatial coordinates χ . The conformal factor $A(\eta)$ in this setting plays the same role as the cycle-averaged $A_{\text{mean}}(t)$ introduced in Eq. (6), providing the smooth

background scale against which oscillations occur. In four spacetime dimensions the source-free Maxwell equations are conformally invariant: if $F_{\mu\nu}$ solves $\nabla_{\mu}F^{\mu\nu}=0$ and $\nabla_{[\alpha}F_{\beta\gamma]}=0$ in the metric $g_{\mu\nu}=A^2\eta_{\mu\nu}$, then the rescaled field $\tilde{F}^{\mu\nu}=F^{\mu\nu}$ (indices raised by $\eta_{\mu\nu}$) obeys the flat-space equations $\partial_{\mu}\tilde{F}^{\mu\nu}=0$, $\partial_{[\alpha}\tilde{F}_{\beta\gamma]}=0$ in (η,χ) . With sources, $\nabla_{\mu}F^{\mu\nu}=\mu_0J^{\nu}$ becomes, after rescaling,

$$\partial_{\mu}\tilde{F}^{\mu\nu} = \mu_0 A^3 \tilde{J}^{\nu}, \qquad \tilde{J}^{\nu} \equiv A^{-3} J^{\nu}, \tag{C.2}$$

and charge conservation is $\partial_{\nu}\tilde{J}^{\nu}=0$. Thus the field equations in (η,χ) take the *Minkowski form* with a conserved current \tilde{J}^{ν} .

C.2 Poynting flux and conformal scaling

Let $T_{\rm EM}^{\mu\nu}=\frac{1}{\mu_0}\left(F^{\mu\alpha}F^{\nu}{}_{\alpha}-\frac{1}{4}g^{\mu\nu}F^{\alpha\beta}F_{\alpha\beta}\right)$ be the electromagnetic stress–energy tensor. In the conformal metric (C.1) and for any hypersurface with unit normal n_{μ} and induced area element $d\Sigma_{\nu}$, the radiated power through a large sphere S_R (radius R in χ -coordinates) is

$$P(\eta) = \int_{\mathcal{S}_R} T_{\text{EM}}^{\mu\nu} u_{\mu} d\Sigma_{\nu}, \qquad u^{\mu} = A^{-1}(1, \mathbf{0}) \text{ (static observer)}.$$
 (C.3)

Using the conformal relation and the rescaled (Minkowski) fields $\tilde{\mathbf{E}}, \tilde{\mathbf{B}}$ defined in (η, χ) , one finds

$$P(\eta) = A(\eta)^{-4} \tilde{P}(\eta), \qquad \tilde{P}(\eta) \equiv \int_{\tilde{S}_R} \tilde{\mathbf{S}} \cdot d\tilde{\mathbf{A}},$$
 (C.4)

where $\tilde{\mathbf{S}} = \frac{1}{\mu_0} \tilde{\mathbf{E}} \times \tilde{\mathbf{B}}$ is the flat-space Poynting vector in the (η, χ) chart. Thus the question of radiation in the physical metric reduces to whether \tilde{P} is nonzero in the conformal frame. If the cycle–average $\langle \tilde{P} \rangle_{\eta} = 0$, then $\langle P \rangle = 0$ as well.

C.3 Stationary bound states as standing—wave sources

In VBT, a stationary atomic state corresponds to a time-periodic and spatially localized current $\tilde{J}^{\mu}(\eta, \chi)$ in the conformal frame (e.g. the diametric shuttle for s-states, with uniform motion through the fabric between turning regions). Decompose the source in temporal Fourier modes:

$$\tilde{J}^{\mu}(\eta, \chi) = \sum_{n \in \mathbb{Z}} \hat{J}_{n}^{\mu}(\chi) e^{-in\omega_{b}\eta}, \qquad \omega_{b} = \text{breathing/beat frequency.}$$
 (C.5)

The causal (outgoing-wave) solution in flat (η, χ) separates into near- and far-field parts. At large $\chi = R$, the radiative field is proportional to the causal time derivatives of the *multipole moments* of \hat{J}_n^{μ} . For a *standing-wave* source built from equal–amplitude counter–propagating harmonics (the constructive mechanism for stationarity), the outgoing and incoming 1/R pieces cancel in the cycle average:

$$\tilde{\mathbf{E}}^{\mathrm{rad}} = \tilde{\mathbf{E}}_{+}^{\mathrm{rad}} + \tilde{\mathbf{E}}_{-}^{\mathrm{rad}}, \quad \tilde{\mathbf{B}}^{\mathrm{rad}} = \tilde{\mathbf{B}}_{+}^{\mathrm{rad}} + \tilde{\mathbf{B}}_{-}^{\mathrm{rad}}, \quad \left\langle \tilde{\mathbf{S}} \cdot \hat{\mathbf{n}} \right\rangle_{\eta} = \left\langle \tilde{\mathbf{S}}_{+} \cdot \hat{\mathbf{n}} \right\rangle_{\eta} + \left\langle \tilde{\mathbf{S}}_{-} \cdot \hat{\mathbf{n}} \right\rangle_{\eta} + \left\langle \mathrm{cross} \right\rangle_{\eta} = 0. \quad (\mathrm{C.6})$$

Physically: a stationary bound state cannot feed a net outward radiative flux at infinity in the conformal frame; its fields are reactive/evanescent (near-field) with zero net energy transport per cycle. By (C.4), this implies $\langle P \rangle = 0$ in the physical metric as well.

Dipole check (selection rule form). In the conformal frame, the leading radiative channel is dipole radiation with power $\tilde{P}_{\rm dip} \propto \left|\frac{d^2\tilde{\mathbf{d}}}{d\eta^2}\right|^2$, where $\tilde{\mathbf{d}}(\eta) = \int \chi \, \tilde{\rho} \, d^3 \chi$. For stationary bound states the source has definite parity and a fixed azimuthal structure (over a cycle), so the net dipole channel averages to zero; transitions (e.g. $2p \to 1s$) occur only when the source acquires the appropriate oscillatory component at the transition frequency, reproducing the usual selection rules. Hence $\langle \tilde{P}_{\rm dip} \rangle_{\eta} = 0$ in stationary states.

C.4 Local criterion via proper acceleration

A complementary local statement uses the covariant Larmor scalar. Let $u^{\mu} = dx^{\mu}/d\tau$ be the four-velocity and $a^{\mu} = u^{\nu} \nabla_{\nu} u^{\mu}$ the proper four-acceleration in the physical metric $g_{\mu\nu} = A^2 \eta_{\mu\nu}$. The radiative power measured in the comoving frame is proportional to the invariant

$$\mathcal{P} \propto q^2 a^{\mu} a_{\mu} \,, \tag{C.7}$$

so worldlines with $a^{\mu}a_{\mu}=0$ do not radiate locally.³ In the conformal metric (C.1), geodesics satisfy $a^{\mu}=0$. The VBT construction takes the *fabric-frame* motion to be uniform between turning regions (piecewise geodesic in (η, χ)), so that $a^{\mu}a_{\mu}=0$ except where the binding potential reverses the motion. The global statement (C.6) then guarantees that the cycle-averaged power still vanishes: the transient local accelerations at turning regions do not produce a net outward 1/R flux when the full standing-wave source is taken into account.

C.5 Conclusion

Maxwell's conformal behavior reduces the radiation question to a flat–space calculation in conformal coordinates. Stationary bound states correspond to standing–wave sources, which carry no net Poynting flux through a distant sphere per cycle; by conformal scaling, the physical radiated power also averages to zero. Equivalently, the covariant Larmor scalar $a^{\mu}a_{\mu}$ vanishes along the uniform fabric–frame segments of the motion, and the remaining turning–region contributions cancel at the level of the far–field 1/R terms. Therefore, stationary VBT orbitals are non–radiating.

D Lagrangian Formulation for Electromagnetism in the Breathing Vacuum

For completeness, we recall the standard electromagnetic Lagrangian density:

$$\mathcal{L}_{EM} = -\frac{1}{4} F_{\mu\nu} F^{\mu\nu} - J_{\mu} A^{\mu}, \tag{D.1}$$

where $F_{\mu\nu} = \partial_{\mu}A_{\nu} - \partial_{\nu}A_{\mu}$ is the field strength tensor and J_{μ} is the 4-current density. This conventional formulation provides the baseline against which VBT modifications may be compared, without invoking additional assumptions from quantum electrodynamics [32].

A concise action for the transverse degrees of freedom of the vacuum fabric is

$$S_{\rm EM} = \int d^4x \, \frac{\rho_v}{2} \left[\frac{1}{c^2} (\partial_t \boldsymbol{\xi}_\perp)^2 - (\nabla \boldsymbol{\xi}_\perp)^2 \right], \tag{D.2}$$

³In flat space this reduces to the Liénard formula; the generalization to curved spacetimes keeps the same scalar $a^{\mu}a_{\mu}$ in the local limit.

where $c^2 = \kappa_v/\rho_v$ as in Section 8. Introducing the vector potential

$$\mathbf{A} \equiv \Lambda \, \partial_t \boldsymbol{\xi}_\perp, \tag{D.3}$$

and defining $A_{\mu} = (\phi/c, \mathbf{A})$, the action becomes

$$S_{\rm EM} = -\frac{1}{4\mu_0} \int d^4x \ F_{\mu\nu} F^{\mu\nu},$$
 (D.4)

with $F_{\mu\nu} = \partial_{\mu}A_{\nu} - \partial_{\nu}A_{\mu}$ and $\mu_0^{-1} = \Lambda^2 \rho_v c^2$. Varying with respect to A_{μ} yields the source-free Maxwell equations. Coupling to matter is introduced via

$$S_{\rm int} = \int d^4x \ J^{\mu} A_{\mu},\tag{D.5}$$

which enforces charge conservation $\partial_{\mu}J^{\mu}=0$.

D.1 Charge as a Topological Defect in the Vacuum Fabric

In VBT, electric charge corresponds to a topological winding of an internal U(1) order parameter $\theta_{U(1)}(\mathbf{x})$, not of the global Planck carrier. The carrier $\Phi_P(t)$ remains strictly synchronized everywhere. A 2π winding in $\theta_{U(1)}$ produces quantized flux, consistent with Gauss's law. Thus charge is a defect in the vacuum's internal orientation, while the underlying breathing oscillation is untouched.

D.2 Remarks

This picture unifies:

- Elastic wave physics of the vacuum fabric with the field theory of electromagnetism.
- Charge conservation with topological invariance of phase winding.
- Gauge symmetry with the freedom to redefine the carrier phase without changing measurable fields.

At Planck resolution, both the breathing (longitudinal) and shear (transverse) modes coexist, but only the shear modes survive as propagating disturbances at low frequency, giving rise to photons.

E Vacuum birefringence

In strong external fields the vacuum acquires effective nonlinearities described by the Heisenberg–Euler Lagrangian,

$$\mathcal{L}_{HE} = \frac{1}{2} \left(\mathbf{E}^2 - \mathbf{B}^2 \right) + \frac{2\alpha^2}{45m_e^4} \left[\left(\mathbf{E}^2 - \mathbf{B}^2 \right)^2 + 7 \left(\mathbf{E} \cdot \mathbf{B} \right)^2 \right]. \tag{E.1}$$

For a probe wave propagating perpendicular to a static magnetic field B, the refractive indices for polarizations parallel/perpendicular to B are

$$n_{\parallel} - 1 = \frac{7\alpha}{90\pi} \left(\frac{B}{B_c}\right)^2,\tag{E.2}$$

$$n_{\perp} - 1 = \frac{4\alpha}{90\pi} \left(\frac{B}{B_c}\right)^2,\tag{E.3}$$

with

$$B_c = \frac{m_e^2 c^3}{e\hbar} \simeq 4.4 \times 10^9 \,\text{T}.$$
 (E.4)

The birefringence signal is therefore

$$\Delta n_{\text{QED}} = n_{\parallel} - n_{\perp} = \frac{3\alpha}{90\pi} \left(\frac{B}{B_c}\right)^2. \tag{E.5}$$

E.1 VBT expectation.

Within the breathing framework, Maxwell's equations remain conformally invariant, so the leading nonlinearity is unchanged. Any VBT correction appears as a fractional modification of the Heisenberg–Euler coefficients,

$$\Delta n_{\text{VBT}} = \Delta n_{\text{QED}} (1 + \xi), \qquad \xi = \mathcal{O}(\varepsilon^2),$$
 (E.6)

which vanishes as the breathing amplitude $\varepsilon \to 0$. Vacuum birefringence therefore acts as a null test for VBT-specific corrections.

E.2 Laboratory bound.

At $B \simeq 2.5 \,\mathrm{T}$, QED predicts

$$\Delta n_{\rm QED} \approx 2.5 \times 10^{-23}.\tag{E.7}$$

PVLAS reports

$$\Delta n = (12 \pm 17) \times 10^{-23}$$
 $(B = 2.5 \,\mathrm{T}),$ (E.8)

consistent with the prediction within sensitivity [36, 59]. This constrains deviations to

$$|\xi| \lesssim 7 \ (1\sigma), \qquad |\xi| \lesssim 20 \ (3\sigma).$$
 (E.9)

E.3 Astrophysical evidence.

Optical polarimetry of neutron star RX J1856.5-3754 reported a linear polarization degree of ~16, supporting the existence of vacuum birefringence in the strong-field regime [60]. Recent X-ray polarimetric observations of magnetars by IXPE—including the first measurements from 4U 0142+61 and 1E 1841-045—show strong, energy-dependent polarization patterns that are consistent with QED-induced birefringence and mode conversion effects [29, 30].

E.4 Summary.

VBT predicts the same birefringence signal as QED at leading order. Present laboratory and astrophysical observations are consistent, while a future laboratory detection of Δn at the QED level would immediately constrain any breathing-induced correction ξ to $\ll 1$.

F Simulation validation

To validate the analytic radial probability densities, we generated synthetic trajectories using the inverse-CDF method. A uniform random sequence $u \in [0,1]$ was mapped to radii r by inverting the cumulative distribution $F(r) = \int_0^r P(r') dr'$ of the target hydrogenic state. By stepping through this sequence at fixed angular increments we obtain time series r(t) whose histograms can be compared

directly to the analytic distributions. This procedure reproduces the correct weighting by sampling design and is used purely as a numerical validation tool, not as an independent derivation.

For completeness we present additional checks for the 2s and 2p states that were omitted from the main text for brevity.

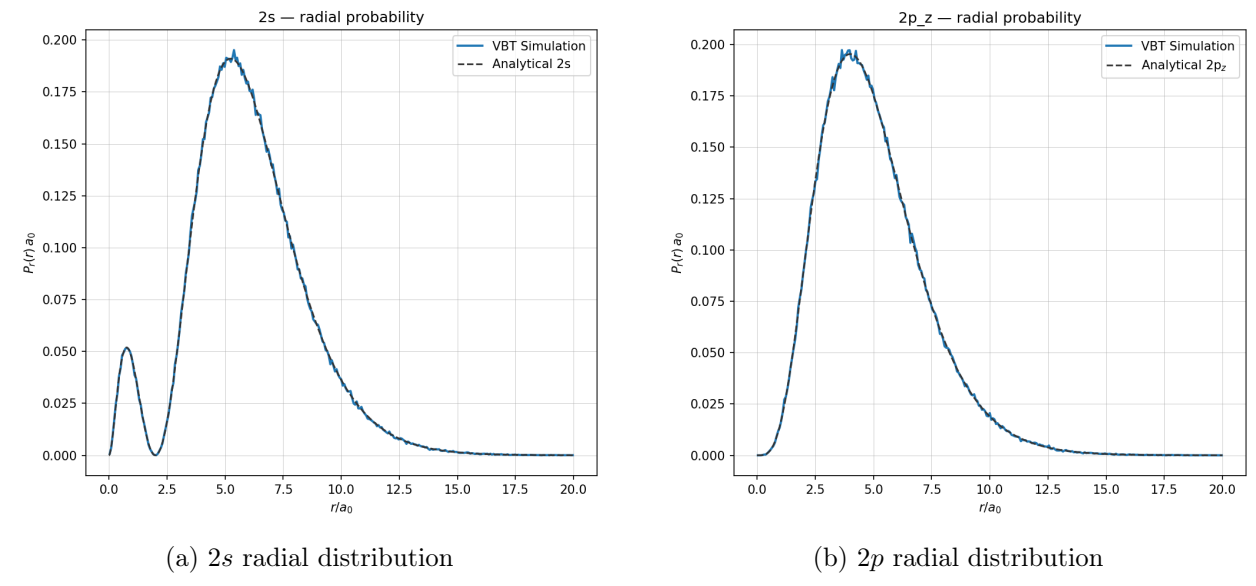


Figure 18: Validation of the 2s and 2p radial distributions. Histograms of radii r(t) from inverse-CDF validation compared with the analytic densities. Both cases show L_1 error $\lesssim 10^{-2}$, confirming that the sampling method reproduces the analytic distributions.

Summary. These results demonstrate that the inverse-CDF validation produces trajectories whose histograms agree with the analytic radial PDFs for the 2s and 2p states. They serve as validation of the analytic derivation presented in Sec. 4.4, not as an independent assumption.

References

- [1] G. E. Volovik. The Universe in a Helium Droplet. Oxford University Press, Oxford, 2003.
- [2] David Izabel. Analogy of space-time as an elastic medium state of the art and perspectives on the knowledge of time. *preprint*, 2025. Preprints.org, doi:10.20944/preprints202508.1443.v1.
- [3] David L. Poole. Vacuum breathing theory: A deterministic framework for atomic structure and cosmology, 2025. First public preprint, Rev.1, 10.5281/zenodo.17050452.
- [4] Max Planck. On the law of distribution of energy in the normal spectrum. *Annalen der Physik*, 4:553–563, 1901.
- [5] Louis de Broglie. Recherches sur la théorie des quanta. PhD thesis, Université de Paris, 1924.
- [6] E. Madelung. Quantentheorie in hydrodynamischer form. Zeitschrift für Physik, 40:322–326, 1927.
- [7] Erwin Schrödinger. Quantisierung als Eigenwertproblem. Annalen der Physik, 79:361–376, 1926.

- [8] Niels Bohr. On the constitution of atoms and molecules. *Philosophical Magazine*, 26(151):1–25, 1913.
- [9] Werner Heisenberg. Über den anschaulichen inhalt der quantentheoretischen kinematik und mechanik. Zeitschrift für Physik, 43:172–198, 1927.
- [10] H. P. Robertson. The uncertainty principle. Physical Review, 34:163–164, 1929.
- [11] P. A. M. Dirac. The quantum theory of the electron. *Proceedings of the Royal Society A*, 117:610–624, 1928.
- [12] Hans A. Bethe and Edwin E. Salpeter. Quantum Mechanics of One- and Two-Electron Atoms. Springer, 1957.
- [13] S. P. Goldman and G. W. F. Drake. Relativistic two-photon decay rates in hydrogen-like ions. *Phys. Rev. A*, 24:183–192, 1981.
- [14] W. E. Lamb and R. C. Retherford. Fine structure of the hydrogen atom by a microwave method. *Phys. Rev.*, 72:241–243, 1947.
- [15] C. Schwob, L. Jozefowski, B. de Beauvoir, L. Hilico, F. Nez, L. Julien, and F. Biraben. Optical frequency measurement of the 2s 12d transitions in hydrogen and deuterium: Rydberg constant and lamb shift determinations. *Phys. Rev. Lett.*, 82:4960–4963, 1999.
- [16] David L. Poole. Testing the temporal structure of single-photon emission with trapped ions, 2025. Revision 2.
- [17] K. S. Novoselov et al. Two-dimensional gas of massless dirac fermions in graphene. *Nature*, 438:197–200, 2005.
- [18] Luna Y. Liu, Steffi Y. Woo, Jinyuan Wu, Bowen Hou, Cong Su, Diana Y. Qiu, et al. Direct observation of massless excitons and linear exciton dispersion in monolayer hexagonal boron nitride. arXiv preprint arXiv:2502.20454, 2025. measured linear exciton branch due to long-range exchange;.
- [19] Alessandro Nicolaou, Kari Ruotsalainen, Laura Susana, Victor Porée, Luiz Galvao Tizei, Jaakko Koskelo, et al. Direct measurement of the longitudinal exciton dispersion in hbn by resonant inelastic x-ray scattering. *Physical Review B*, 112:085207, 2025.
- [20] E. H. Hauge and J. A. Støvneng. Tunneling times: a critical review. Reviews of Modern Physics, 61(4):917–936, 1989.
- [21] A. M. Steinberg, P. G. Kwiat, and R. Y. Chiao. Measurement of the single-photon tunneling time. *Physical Review Letters*, 71(5):708–711, 1993.
- [22] K. von Klitzing, G. Dorda, and M. Pepper. New method for high-accuracy determination of the fine-structure constant based on quantized hall resistance. *Physical Review Letters*, 45(6):494–497, 1980.
- [23] K. S. Novoselov, A. K. Geim, S. V. Morozov, D. Jiang, M. I. Katsnelson, I. V. Grigorieva, S. V. Dubonos, and A. A. Firsov. Two-dimensional gas of massless dirac fermions in graphene. *Nature*, 438:197–200, 2005.

- [24] Massimiliano Rossi, Andrei Militaru, Nicola Carlon Zambon, Andreu Riera-Campeny, Oriol Romero-Isart, Martin Frimmer, and Lukas Novotny. Quantum delocalization of a levitated nanoparticle. *Physical Review Letters*, 135(8):h3601, 2025.
- [25] S. L. Adler. Photon splitting and photon dispersion in a strong magnetic field. *Annals of Physics*, 67:599–647, 1971.
- [26] E. Zavattini et al. Experimental observation of optical rotation generated in vacuum by a magnetic field. *Physical Review Letters*, 96:110406, 2006.
- [27] A. Cadène et al. Vacuum magnetic birefringence experiment. European Physical Journal D, 68:16, 2014.
- [28] H. von Helmholtz. Über integrale der hydrodynamischen gleichungen, welche den wirbelbewegungen entsprechen. Journal für die reine und angewandte Mathematik, 55:25–55, 1858.
- [29] Dong Lai et al. Ixpe detection of polarized x-rays from magnetars and photon mode conversion at qed vacuum resonance. *Proceedings of the National Academy of Sciences*, 120:e2301683120, 2023.
- [30] Michela Rigoselli et al. Ixpe detection of highly polarized x-rays from the magnetar 1e 1841-045. arXiv preprint, 2024.
- [31] John David Jackson. Classical Electrodynamics. Wiley, 3 edition, 1998.
- [32] Claude Cohen-Tannoudji, Jacques Dupont-Roc, and Gilbert Grynberg. Atom-Photon Interactions: Basic Processes and Applications. Wiley, 1992.
- [33] Particle Data Group. Review of particle physics. Progress of Theoretical and Experimental Physics, 2024(8):083C01, 2024.
- [34] Michael Faraday. On the rotation of the plane of polarization of light by magnetic forces. *Philosophical Transactions of the Royal Society of London*, 136:1–20, 1846.
- [35] John Kerr. A new relation between electricity and light: Dielectric media birefringent in the presence of an electric field. *Philosophical Magazine*, 50:337–348, 1875.
- [36] R. Battesti and C. Rizzo. Magnetic and electric properties of quantum vacuum. *Rep. Prog. Phys.*, 76:016401, 2013.
- [37] Gerald V. Dunne. The heisenberg-euler effective action: 75 years on. arXiv e-prints, 2012.
- [38] Elda Guzman-Herrera and Nora Breton. Euler-heisenberg waves propagating in a magnetic background. European Physical Journal C, 81(115), 2021.
- [39] David J. Griffiths. *Introduction to Electrodynamics*. Cambridge University Press, Cambridge, 4th edition, 2017.
- [40] C. N. Yang and R. L. Mills. Conservation of isotopic spin and isotopic gauge invariance. *Physical Review*, 96(1):191–195, 1954.
- [41] L. D. Landau and E. M. Lifshitz. *The Classical Theory of Fields*, volume 2 of *Course of Theoretical Physics*. Pergamon Press, Oxford, 4th edition, 1986.

- [42] T. Kopf, M. Krenn, R. Fickler, M. Huber, and A. Zeilinger. Conservation of orbital angular momentum in single-photon pumped parametric down-conversion. *Physical Review Letters*, 134(20):203601, 2025.
- [43] Albert Einstein. Die grundlage der allgemeinen relativitätstheorie. Annalen der Physik, 49:769–822, 1916.
- [44] E. Mach. The Science of Mechanics. Cambridge University Press, 1883.
- [45] Edwin Hubble. A relation between distance and radial velocity among extra-galactic nebulae. Proceedings of the National Academy of Sciences, 15(3):168–173, 1929.
- [46] A. G. Riess et al. Observational evidence from supernovae for an accelerating universe and a cosmological constant. Astronomical Journal, 116:1009–1038, 1998.
- [47] S. Perlmutter et al. Measurements of ω and λ from 42 high-redshift supernovae. Astrophysical Journal, 517:565–586, 1999.
- [48] P. J. E. Peebles. Cosmology's Century: An Inside History of Our Modern Understanding of the Universe. Princeton University Press, 2020.
- [49] Planck Collaboration. Planck 2018 results. vi. cosmological parameters. Astronomy and Astrophysics, 641:A6, 2020.
- [50] A. H. Guth. Inflationary universe: A possible solution to the horizon and flatness problems. *Physical Review D*, 23:347–356, 1981.
- [51] V. C. Rubin and W. K. Jr. Ford. Rotation of the andromeda nebula from a spectroscopic survey of emission regions. *Astrophysical Journal*, 159:379–403, 1970.
- [52] Y. Sofue. Rotation curve and mass distribution in the galaxy. *Publications of the Astronomical Society of Japan*, 69:R1, 2017.
- [53] S. S. McGaugh. Predictions and outcomes for the rotation curves of gas-rich galaxies. *Galaxies*, 8:35, 2020.
- [54] Steven Weinberg. Gravitation and Cosmology: Principles and Applications of the General Theory of Relativity. Wiley, 1972.
- [55] A. Sandage. The change of redshift and apparent luminosity of galaxies due to the deceleration of selected expanding universe models. *Astrophysical Journal*, 136:319–333, 1962.
- [56] J. Liske et al. Cosmic dynamics in the era of extremely large telescopes: The codex experiment. Monthly Notices of the Royal Astronomical Society, 386:1192–1202, 2008.
- [57] J. Lense and H. Thirring. On the influence of the proper rotation of central bodies on the motion of planets and moons according to einstein's theory of gravitation. *Physikalische Zeitschrift*, 19:156–163, 1918.
- [58] C. M. Will. The confrontation between general relativity and experiment. Living Reviews in Relativity, 17(4), 2014.
- [59] F. Della Valle and others (PVLAS Collaboration). First results from the new pvlas apparatus: A new limit on vacuum magnetic birefringence. *Phys. Rev. D*, 90:092003, 2014.

[60] R. P. Mignani et al. Evidence for vacuum birefringence from the first optical-polarimetry measurement of the isolated neutron star rx j1856.5–3754. *Monthly Notices of the Royal Astronomical Society*, 465:492–500, 2017.